HOMELANDER

TEAM DRACO - HOMELANDER

University of Illinois Urbana - Champaign

2024 - 2025 AIAA Undergraduate Design Competition

Homeland Defense Interceptor Design Proposal

DRACO AEROSPACE

Draco Aerospace Team

Alex Hausser

Stability & Control
Avionics
AIAA ID #1810180

Zach Baker

Team Lead
Interior Design
AIAA ID #1325431

Yair Guerrero

Structures
Repair & Mainenance
AIAA ID #1328548

Zayna Khan

Loads & Dynamics
Certification
AIAA ID #1747555

Aidan Menees

Aerodynamics
Configuration
Survivability
AIAA ID #1339465

Vansh Jain

Performance
Cost Analysis
AIAA ID #1810201

Darwin Maco

Propulsion
Landing Gear
AIAA ID #1810181

Sebastian Rivera Morales

Mass Properties
Systems
Ordnance
AIAA ID #1810183

Dr. Jason Merret

Faculty Advisor

AIAA ID #155270

Table of Contents

Nomenclature

C_{D_0} = Parasite Drag Coefficient
C_{D_i} = Induced Drag Coefficient
C_{D_w} = Wave Drag Coefficient
C_l = Sectional Lift Coefficient
C_{lmax} = Maximum Sectional Lift Coefficient
C_{l_p} = Roll Moment Roll Rate Derivative [rad^{-1}]
C_{l_r} = Roll Moment Yaw Rate Derivative [rad^{-1}]
C_{l_β} = Roll Moment Sideslip Derivative [rad^{-1}]
C_{Lmax} = Maximum Aircraft Lift Coefficient
C_L = Lift Coefficient
C_{L_α} = Lift curve slope [rad^{-1}]
C_{M_0} = Zero Lift Moment Coefficient
C_{M_α} = Pitching Moment Angle of Attack Derivative [rad^{-1}]
C_{n_β} = Yaw Moment Sideslip Derivative [rad^{-1}]
C_{n_p} = Yaw Moment Roll Rate Derivative [rad^{-1}]
C_{n_r} = Yaw Moment Yaw Rate Derivative [rad^{-1}]
C_{y_β} = Side Force Sideslip Derivative [rad^{-1}]
C_{y_p} = Side Force Roll Rate Derivative [rad^{-1}]
C_{y_r} = Side Force Yaw Rate Derivative [rad^{-1}]
D_{oleo} = Oleo Diameter [in]
E = Elastic Modulus [KSI]
g = Gravitational Acceleration [ft/s^2]
K = Drag Due to Lift Factor
K_P = Coefficient of Pressure Lift
K_V = Coefficient of Vortex Lift
L_{oleo} = Oleo Length [ft]
L_x = Landing Gear x Coordinate [ft]
L_y = Landing Gear y Coordinate [ft]
L_z = Landing Gear z Coordinate [ft]
L/D = Lift to Drag Ratio
M_{crit} = Critical Mach Number
M_{DD} = Drag Divergence Mach Number
M_∞ = Freestream Mach Number
$\dot{m}_f$ = Fuel Flow [lb/hr]
n = Load Factor
N_{gear} = Landing Gear Load Factor
η = Shock-Absorbing Efficiency
P = Pressure [psi]
P_S = Specific Excess Power
$P_{S_{min}}$ = Minimum Required Specific Excess Power
q = Dynamic Pressure [lb/ft^2]
R = Range [nmi]
S = Wing Planform Area [ft^2]
S_{ref} = Wing Reference Area [ft^2]
SFC = Specific Fuel Consumption [lb/lb-hr]
t/c = Thickness to chord ratio
T = Thrust [lb]
$T_{2,s}$ = Spiral Mode Time to Double [s]
T/W = Thrust to Weight Ratio
V = Velocity, Airspeed [ft/s]
V_{vert} = Landing Vertical Velocity, Airspeed [ft/s]
V_{stall} = Stall speed [kts]
V_{dive} = Dive speed [kts]
V_{b} = Max maneuver speed [kts]
W = Weight [lb]
W_f = Final Weight [lb]
W_i = Initial Weight [lb]
λ = Taper ratio
μ = Mach angle [deg]
ν = Poisson's Ratio
$\omega_{n_{DR}}$ = Dutch Roll Natural Frequency [rad/s]
ω_{n_p} = Phugoid Mode Natural Frequency [rad/s]
$\omega_{n_{sp}}$ = Short-Period Mode Natural Frequency [rad/s]
τ_r = Roll Mode Time Constant [s]
ρ = Density [slug/ft^3]
σ_{ult} = Ultimate Strength [KSI]
σ_{yield} = Yield Strength [KSI]
ζ_{DR} = Dutch Roll Damping Ratio
ζ_p = Phugoid Mode Damping Ratio
ζ_{sp} = Short-Period Mode Damping Ratio

Acronyms

AC	=	Alternating Current
AI	=	Artificial Intelligence
AIM	=	Air Intercept Missile
AIAA	=	American Institution of Aeronautics and Astronautics
AMRAAM	=	Advanced Medium-Range Air-to-Air Missile
AoA	=	Angle of Attack
BLOS	=	Beyond Line of Sight
BPR	=	Bypass Ratio
CA	=	Combat Allowance
CAD	=	Computer Aided Design
CG	=	Center of Gravity
CFD	=	Computational Fluid Dynamics
CFR	=	Code of Federal Regulations
CFT	=	Conformal Tank
CSD	=	Constant-Speed Drive
DAPCA	=	Development and Procurement Costs of Aircraft
DC	=	Direct Current
DCA	=	Defensive Counter-Air
EAS	=	Equivalent Airspeed
EO	=	Electro-Optical
EW	=	Empty Weight
FADEC	=	Full Authority Digital Engine Controller
FBW	=	Fly-by-Wire
FCC	=	Flight Control Computer
FEA	=	Finite Element Analysis
FPR	=	Fan Pressure Ratio
GCS	=	Ground Control Station
GCU	=	Generator Control Unit
GFE	=	Government Furnished Equipment
GTOW	=	Gross Take-off Weight
HDI	=	Homeland Defense Interceptor
HPC	=	High Pressure Compressor
HPT	=	High Pressure Turbine
ICNIA	=	Integrated Communication, Navigation, and Identification Avionics
IDG	=	Integrated Drive Generator
INEWS	=	Integrated Electronic Warfare System
ISA	=	International Standard Atmosphere
I/E	=	Intercept/Escort
IFF	=	Identification Friend or Foe
IR	=	Infrared
IRSTS	=	Infrared Search and Track System
JFS	=	Jet Fuel Starter
KEAS	=	Knots Equivalent Airspeed
LAU	=	Launcher Unit
LCC	=	Lifecycle Cost
LE	=	Leading Edge
LOS	=	Line of Sight
LPT	=	Low Pressure Turbine
MAC	=	Mean Aerodynamic Chord
MMH/FH	=	Maintenance Man Hour per Flight Hour
MSL	=	Mean Sea Level
MTOW	=	Max Take-off Weight
NASA	=	National Aeronautics and Space Administration
NATO	=	North Atlantic Treaty Organization
OML	=	Outer Mold Line
OPR	=	Overall Pressure Ratio
OV1	=	Operational Concept Graphic
O&S	=	Operating and Support
PDI	=	Point Defense Intercept
RAT	=	Ram Air Turbine
RCS	=	Radar Cross Section
RF	=	Radio Frequency
RFP	=	Request for Proposal
RPM	=	Revolutions Per Minute
R&D	=	Research and Development
SL	=	Sea Level
STL	=	StereoLithography
SFC	=	Specific Fuel Consumption
SM	=	Static Margin
TE	=	Trailing Edge
TRU	=	Transformer Rectifier Unit
UMCS	=	Unmanned Carrier Aviation Mission Control Station
WUTTO	=	Warmup-to-Take-off
UAV	=	Unmanned Aerial Vehicle
VMS	=	Vehicle Management System

List of Tables

List of Figures

DRACO AEROSPACE

THE HOMELANDER

DRACO AEROSPACE

$24.7 MILLION
FLY AWAY COST

$117 MILLION
LIFE CYCLE COST

31,034 LB
GROSS WEIGHT

15,890LB
EMPTY WEIGHT

4200 NMI
RANGE AT MACH 0.8

2500 NMI
RANGE AT MACH 1.1

1.1 MACH
CRUISE SPEED

2.0 MACH
DASH SPEED

14,490 LBS OF FUEL

60,000 + FT CEILING

12 MAX G RATING

AIM-9 SIDEWINDER
OPTIONAL WINGTIP

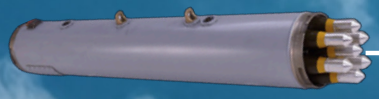

LAU-131 LAUNCHER
OPTIONAL WINGTIP

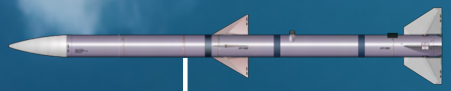

INTERNAL BAY
2 AIM-120 AMMRAAM

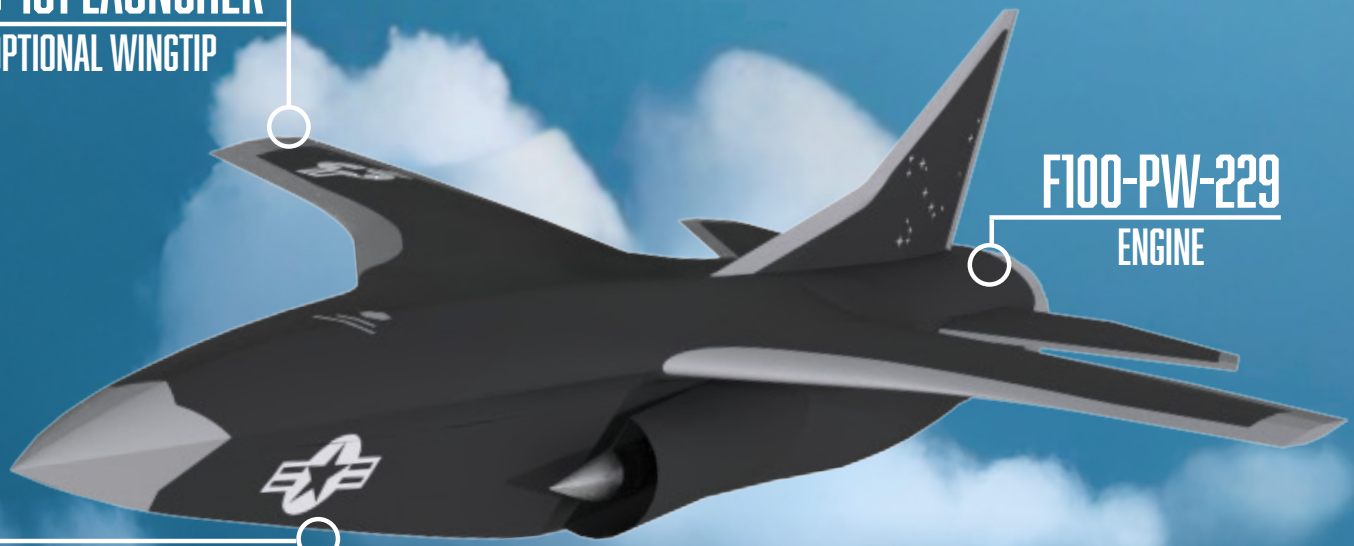

F100-PW-229
ENGINE

LENGTH - 50 FT

WINGSPAN - 27 . 4 FT

WING AREA - 300 SQ FT

I. Introduction

With escalating political tensions around the world, the United States needs to be prepared for air attacks on the homeland. These attacks may involve aircraft ranging from hijacked airliners, drone swarms, to small cruise missiles. Most current Air Force and Navy fighter aircraft will reach their service life by 2045, and the F-35 and F-22 are too costly to perform these missions. To address this threat, it is necessary to have a small, high-performance, and cost-effective interceptor that can be purchased in bulk to defend the homeland.

Interceptors are a vital asset to the United States and irreplaceable to protect the homeland. Not only will this aircraft save civilian lives, it will save pilots' lives too by being entirely unmanned. With no pilot, the Homelander will still have just as high of a mission effectiveness as an inhabited flight due to the current technology and training as well as versatile payloads. Team Draco's design focused on reaching and eliminating the target as fast as possible, which is the main goal of an interceptor. This is why the team decided to achieve a dash speed of Mach 2.0 as well as a super-cruise speed of Mach 1.1, above the requirements specified by the Request for Proposal (RFP) [1]. While speed was the focus, the team traded the increase in cost as well to ensure the $25 million flyaway cost was not exceeded. The three design missions specified by the RFP will challenge the Homelander to perform similar to a modern fighter while being one of the smallest in size compared to other interceptor and fighter aircraft. The Homelander was designed to complete these missions as fast and efficiently as possible. The high-wing configuration, sleek fuselage, and planform shape are tailored for high speed flight. The Homelander not only does the job, but it looks the part as well. Every decision made in the design process also received a visual appeal rank that was factored into each decision. The team wanted to design an aircraft that strikes fear into the enemy and be the face of American homeland defense.

II. Compliance Checklist

The requirements of the RFP were demanding and challenging to meet within the required cost, budget, and schedule. Team Draco went to great efforts to meet all requirements, and succeeded as shown in Table 3. A couple of the complex requirements were meeting the flyaway cost budget and various performance requirements such as the maximum 18 deg/s instantaneous turn rate and the 1g and 5g specific excess power requirement. Other derived and flowdown requirements challenged the team especially during the team's attempt to find room for fuel and other internal systems. More challenges will be discussed throughout the report along with the steps to solve them. Additional derived and flowdown requirements will also be discussed throughout the report in their respective sections.

Table 3. RFP Compliance Checklist

Requirement	Compliance	Reference Section
Perform DCA, I/E, and PDI Missions	✓	VIII.C
Carry AIM-120 AMRAAM	✓	XVI.A
All Engine and Engine Cycle Requirements	✓	VII.C
Minimum Performance Requirements/Constraints	✓	VIII.D
Remote Pilot	✓	XV.A
Easy Maintenance Access to Remove Primary Elements of Major Systems	✓	XVIII.A
Limit Load Factors of +7 and -3 Vertical g's at Maneuver Weight	✓	XII.B
Withstand a Dynamic Pressure of 2,133 psf	✓	XII.B
Self Sealing Fuel Tanks using JP-8 Fuel	✓	XIV.C
Subsonic Static Margin Range of -10% and +10%	✓	X.C
Operate in all Weather from Existing NATO Runways	✓	VIII.A
Flyaway Cost for 1,000 Aircraft under $25 Million	✓	XIX.B

Measures of Merit	Compliance	Reference Section
Weights Summary Table	✓	IX
Aircraft Geometry and Systems Integration	✓	V.C
Mission Duration, Radius, Fuel Burn by Mission Segment	✓	VIII.C
Take-off and Landing Distances for all Missions at Various Conditions	✓	VIII.A
Performance at Maneuver Weight	✓	VIII.D
Design Service Life of 2,000 Hours	✓	XIX.C
Flyaway and Total Life Cycle Costs	✓	XIX.B
Digital 3D Model of Aircraft	✓	V.C

III. Concept of Operations

The high-level operational concept graphic (OV1) is presented in Fig. 1 and provides an overview of the Homelander's intended mission profile. The concept is straightforward: reach the target as quickly as possible and neutralize it. The OV1 highlights several representative threats, including cruise missiles and, more recently, high-altitude surveillance balloons. The balloon, in particular, is a highly relevant target given recent events, and the Homelander is specifically designed to engage threats at these altitudes. With a service ceiling of 60,000 ft on dry thrust alone, the Homelander is capable of intercepting any target operating at extreme altitudes.

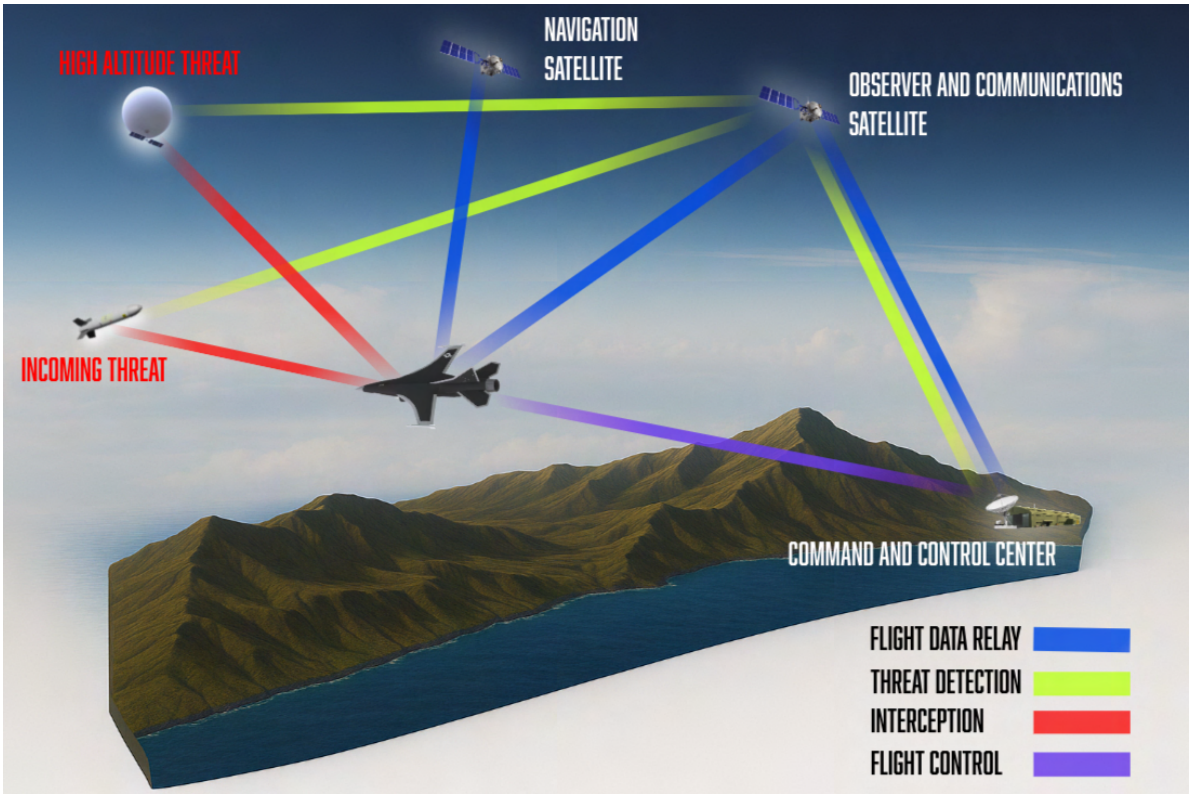

Fig. 1 High-level operational concept graphic (OV1).

The Homelander will be able to complete three different missions as provided by the RFP [1]. The first mission is the defensive counter-air (DCA) patrol mission visualized in Fig. 2. The DCA patrol mission is a protection mission, defined by a long loitering or defensive period, followed by identifying an invading target and then dashing out to perform interception. The loiter segment of this mission is by far the most taxing portion for fuel and was the driver for the Homelander's design. The second mission is a point defense intercept (PDI) mission visualized in Fig. 3. The PDI mission is a true scramble, dash and intercept. While this mission does not drive the design, it is important to optimize the time and cost of this mission. The third mission is an intercept/escort (I/E) mission and visualized in Fig. 4. The I/E mission is a measure of the Homelander's performance and range.

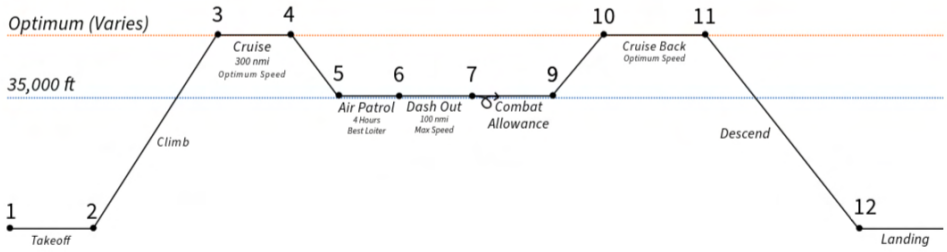

Fig. 2 DCA Mission Diagram

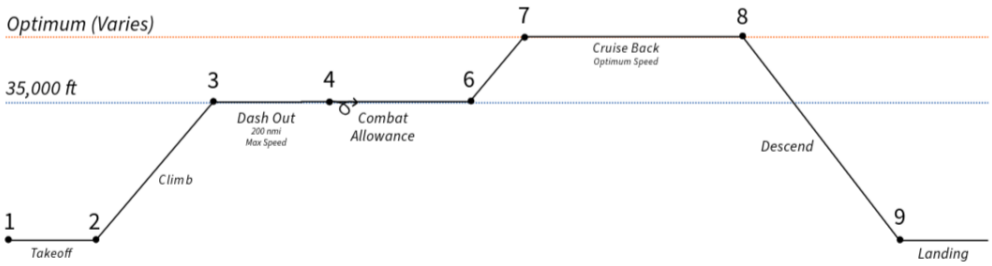

Fig. 3 PDI Mission Diagram

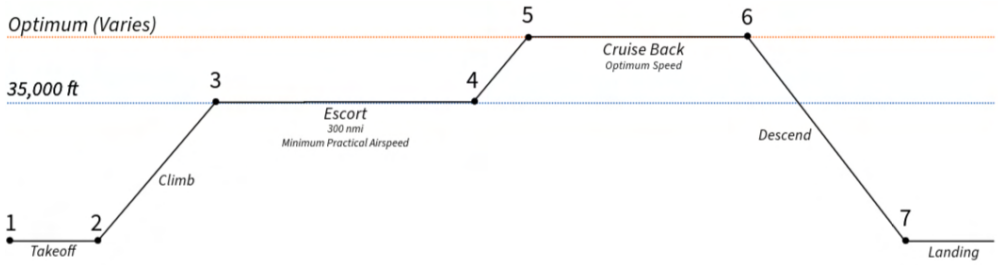

Fig. 4 Intercept/Escort mission diagram.

All combat allowances in the missions must perform two sustained turns at Mach 1.2 and 0.9 and then fire all missiles. This must also happen while maintaining maximum thrust and fuel flow. Another important note is that all of these missions give allowances for warm-up and fuel to accelerate to climb at maximum thrust with no distance credit. For descent to sea level, there is also no distance credit or fuel used. At the end of all of the missions, there needs to be fuel reserves for 30 minutes at sea level at speed for maximum endurance. All missions performed are calculated with standard day conditions and no wind. Another important operational criterion is meeting the take-off and landing requirements. The RFP states the aircraft must operate in all weather from existing NATO runways (8,000 ft), shelters, and maintenance facilities [1]. This is an important requirement that translates into restrictions of take-off and landing field lengths, span, height, turn radius, etc. The team ensured this requirement was met because if the Homelander can not land at a NATO runway, then it can not be relied on in areas on conflict.

IV. Sizing Analysis

Initial sizing of the Homelander was performed through two approaches: a similarity analysis of existing fighter/interceptor aircraft and a constraint analysis. While studying current and past aircraft provides examples of how different problems could be solved, the constraint analysis ensures key performance requirements are being met.

A. Similarity Analysis

A variety of interceptor and fighter aircraft were studied. The aircraft shown in Table 4 below were selected for their desired capabilities and configurations, they all fill similar roles or have similar capabilities to what is demanded of the HDI.

Table 4. Aircraft Similarity Analysis

Parameter	**Homelander**	**F-106A** [2]	**HAL Tejas** [3]	**JAS Gripen** [4]	**F-16C/D** [5]
Empty Weight [lb]	15,890	23,646	14,462	14,991	13,955
MTOW [lb]	31,034	41,831	27,558	36,376	37,500
Length [ft]	50.0	70.67	43.33	48.92	49.5
Dry Thrust [lbf]	17,800	17,200	18,180	18,100	17,155
SFC [lb/lb-hr]	0.73	0.74	0.80	0.84	0.73
Fuel Weight [lb]	14,490	14,495	14,862	15,440	12,000
Wing Area [ft^2]	300	661.5	403.7	320.0	279.9
Aspect Ratio	2.5	2.1	1.93	2.38	3.55

Some patterns and trends become apparent studying the above table. Empty weight (EW) is largely between 14,000 and 16,000 lb. Fuel weight, combining both internal and external stores, is around 14,000 lb with the lighter F-16 being the exception. The F-106A is also an outlier, being an older aircraft utilizing aged technology. Note that all considered aircraft are single engine as cost is a primary consideration, having multiple engines would increase price, particularly with maintenance in the long run. Not listed above is the MQ-28 Ghost Bat, a UAV with capabilities suspected to be comparable to modern multi-role fighters. Due to its currently classified nature, no credible geometric or performance metrics are publicly available. Nonetheless, the MQ-28, being unmanned, served as inspiration for what a fighter without a human cockpit onboard might look like.

The team's final selection for a seed aircraft is the HAL Tejas MK 1, chosen largely due to its delta wing configuration and cost effective design approach. As will be discussed in later sections, the delta wing design was chosen over the conventional configuration. The HAL Tejas fits this design decision and there is a wide array of information on the aircraft to adapt into the similarity analysis sizing code. While not selected, other aircraft such as the F-16 and JAS Gripen still played a critical role serving as inspiring for different elements of the Homelander.

B. Constraint Analysis

Starting from the seed aircraft and a set of constraints defined by the performance requirements of the RFP [1], the aircraft's size was refined through an iterative process. The constraint diagram for the Homelander at maneuver weight with afterburner thrust is shown in Fig. 5 and demonstrates that the two primary driving requirements are the 1-g and 5-g specific excess power requirements at sea level with afterburner. The intersection of these lines places the optimal design point at a wing loading (W/S) of 68.4 lb/ft^2 and a thrust-to-weight (T/W) of 1.10. The Homelander's actual design point, denoted by the green point, falls at W/S = 76.1 lb/ft^2 with a T/W = 1.27 which is very close to the optimal design point. The difference between the predicted optimal T/W and the Homelander's design stems from RFP specific excess power requirements and the requirement of using a non-developmental engine, whose combination can not be scaled to achieve the optimal design point. Similarly, for a given engine choice, scaling the wing area and calculating the required maneuver weight to meet requirements can only achieve a close to optimal design W/S.

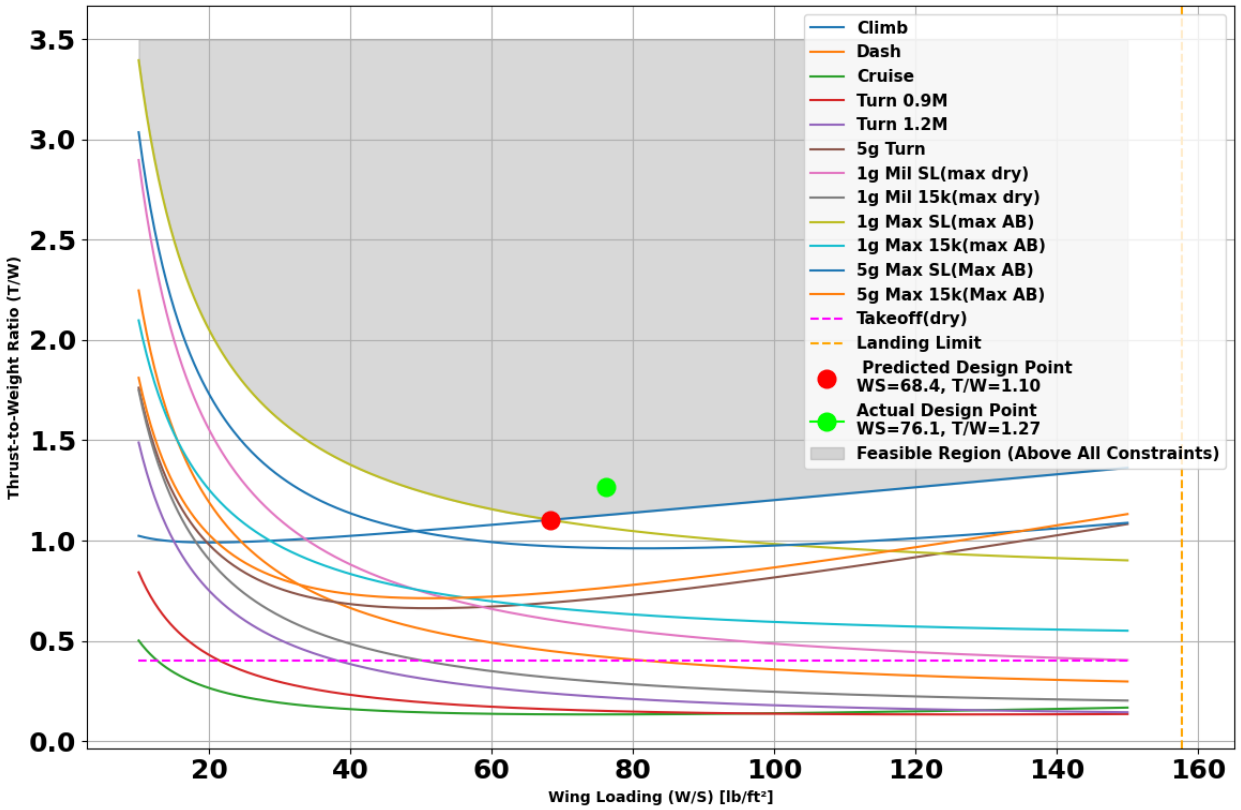

Fig. 5 Constraint diagram based on RFP requirements.

To select a wing area and aspect ratio, a study was performed sweeping across S_{ref} and AR values while simulating fuel requirements for the PDI and DCA patrol missions. The F100-PW-229 had already been selected by the team and was used during this analysis. Reasoning for the engine selection is explained in the later Propulsion Section VII.

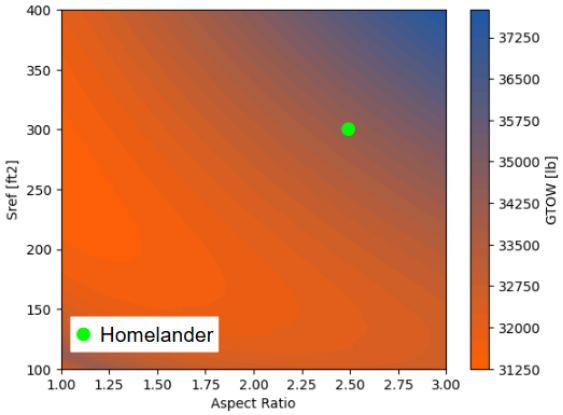

(a) Gross take-off weight study.

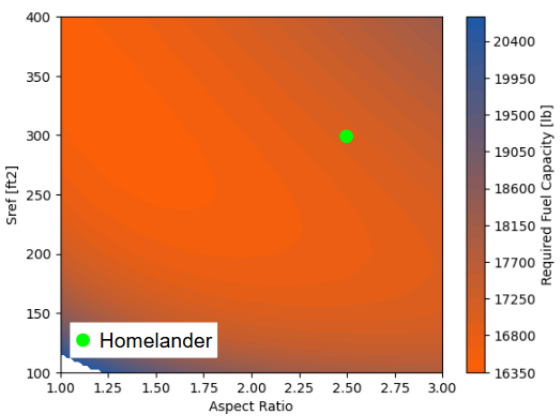

(b) Required fuel weight study.

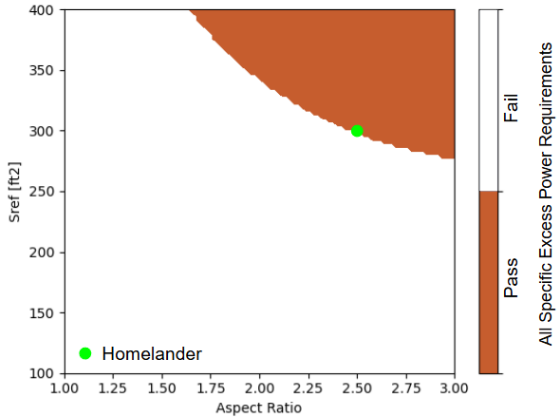

(c) Specific excess power study.

Fig. 6 S_{ref} vs AR study.

As shown in Fig. 6c, the current design point was selected to just meet the specific excess power requirements while minimizing gross take-off and required fuel weight to the greatest extent possible. This produces a wing with an area of 300 ft^2 and aspect ratio of 2.5.

V. Configuration

A. Design Methodology

The RFP specifies criteria and mission profiles that any Homeland Defense Interceptor submission must meet, but a truly effective interceptor must also excel in several additional areas. The core mission is to intercept threats before they reach their targets, so top-performing interceptors engage threats as far out and as quickly as possible, minimizing risk to ground assets. This encourages a configuration capable of supersonic cruise without completely sacrificing low speed efficiency. As will be demonstrated in the Performance Section VIII, the fuel volume requirement for the DCA patrol mission is significant and promotes larger structures for more storage as well as external fuel stores. Cost

is also a primary consideration to remain competitive with fighters like the F-22 and F-35. Ultimately, any proposed configuration must be evaluated not only for mission completion but also for superior performance as an interceptor.

B. Aircraft Configuration Selection

Four aircraft configurations were considered, the conventional, variable sweep, forward swept and delta wing, shown in Fig. 7. High and low sweep variations as well as delta wing with horizontal surfaces were also considered. Each configuration was judged on its potential to complete the required mission set as efficiently as possible while meeting necessary design metrics. The highest significance was placed on weight and cost as well as considering subsonic and supersonic attributes. A decision matrix is shown in Table 5. In this matrix, the baseline values for weight and cost are derived from the conventional configurations with performance in one regime of flight versus the other judged relative to the high and low-sweep conventional variations. A description of this scoring is shown in Table. 6.

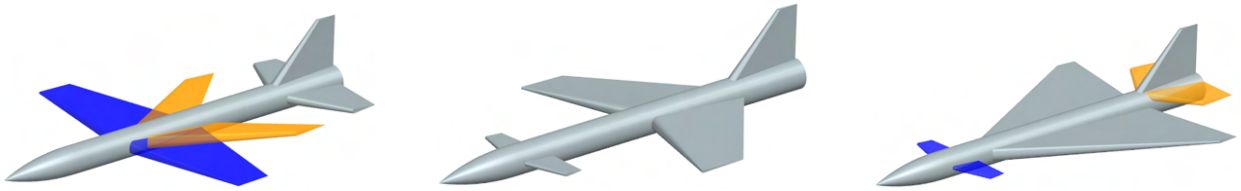

(a) High and low swept wings. **(b) Forward swept wings.** **(c) Delta wing w/ added surfaces.**

Fig. 7 Investigated aircraft configurations.

Table 5. Configuration Decision Matrix

Criteria	Weight	High Swp.	Low Swp.	Var. Swp.	Fwd. Swp.	Delta	Delta w/ Surf.
Weight	0.25	0	0	-2	0	1	1
Cost	0.30	0	0	-1	-2	0	0
Supersonic Perf.	0.25	1	-1	2	1	2	1
Subsonic Perf.	0.20	-1	1	2	1	-1	-1
Total		**0.05**	**-0.05**	**0.10**	**-0.15**	**0.55**	**0.30**

Table 6. Decision Matrix Scoring Description

	Poor	Worsened	Nominal	Improved	Excellent
Score	-2	-1	0	1	2

As shown in the matrix, the delta wing won out over other configurations because of its lighter weight and good supersonic performance, even in spite of its worsened low-speed properties. In second, the tailed delta wing has similar attributes. Variable sweep is also shown to be viable, with great aerodynamic properties but it simply adds too much weight and cost to fully justify. The conventional high/low sweep and forward swept wings, while not being bad configurations, are just not as well suited for the tasks required of a dedicated Homeland Defense Interceptor.

As design work progressed, stabilizing the delta wing in the longitudinal axis proved to be a challenge without introducing an excessive wingtip washout. As a compromise between aerodynamics, stability, and structures a much smaller three degree washout was implemented and an appropriately sized horizontal tail was added. More is discussed about this tradeoff in the later Stability & Control Section X. A 3-view drawing of the final configuration of the Homelander is seen in Fig. 8.

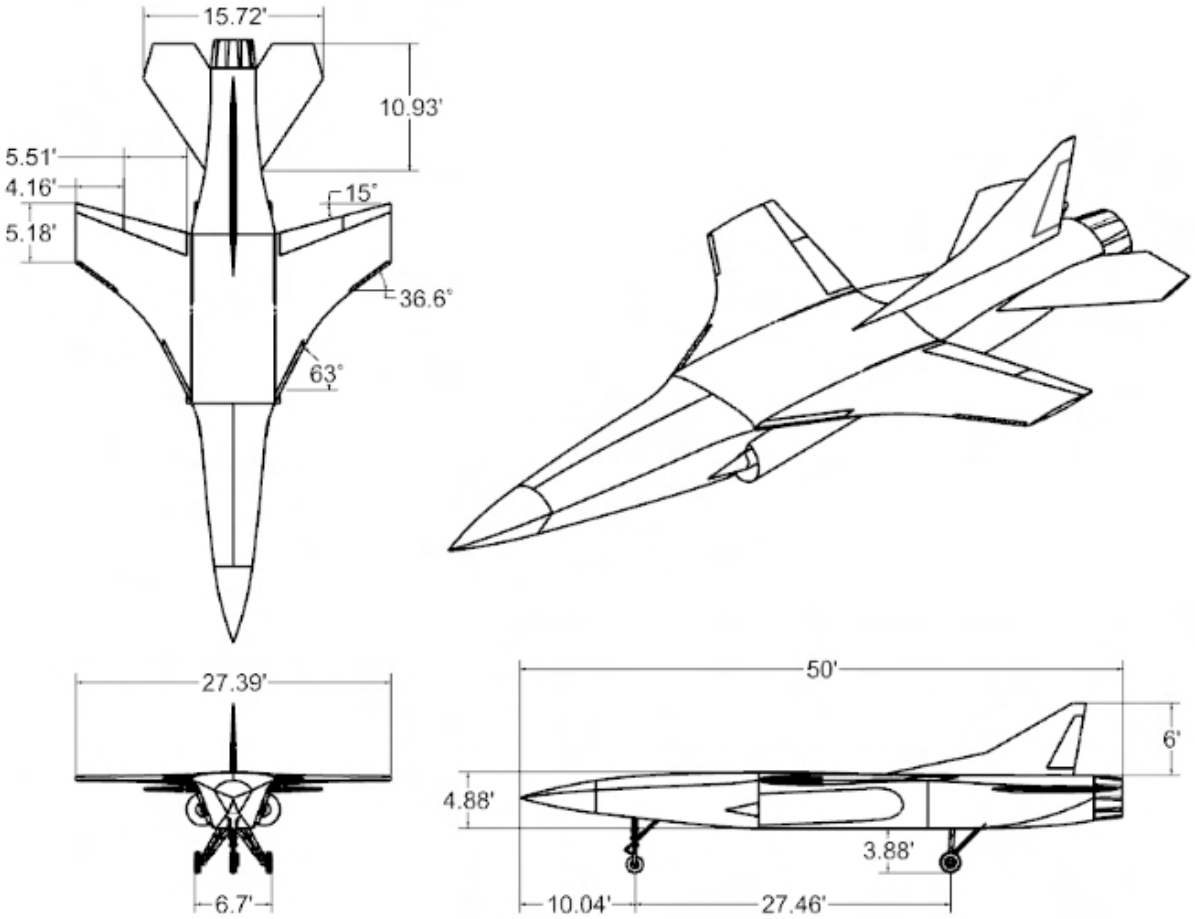

Fig. 8 3-view drawing of the Homelander.

C. Internal Component Layout

As shown in Fig. 9, the internal placement of location-sensitive components such as radar and landing gear were given priority. Structure was also a consideration when placing components. Fuel volume was considered next, requiring enough room to fulfill mission requirements and placed to minimize the center of gravity shifting. Other systems such as avionics, ram air turbines, or utility routing were placed within the remaining space. Overall, the total available fuselage volume for all internal components and structures within the fuselage was 641.5 ft^3, making efficient packaging and careful placement essential to fit all required systems within the limited space.

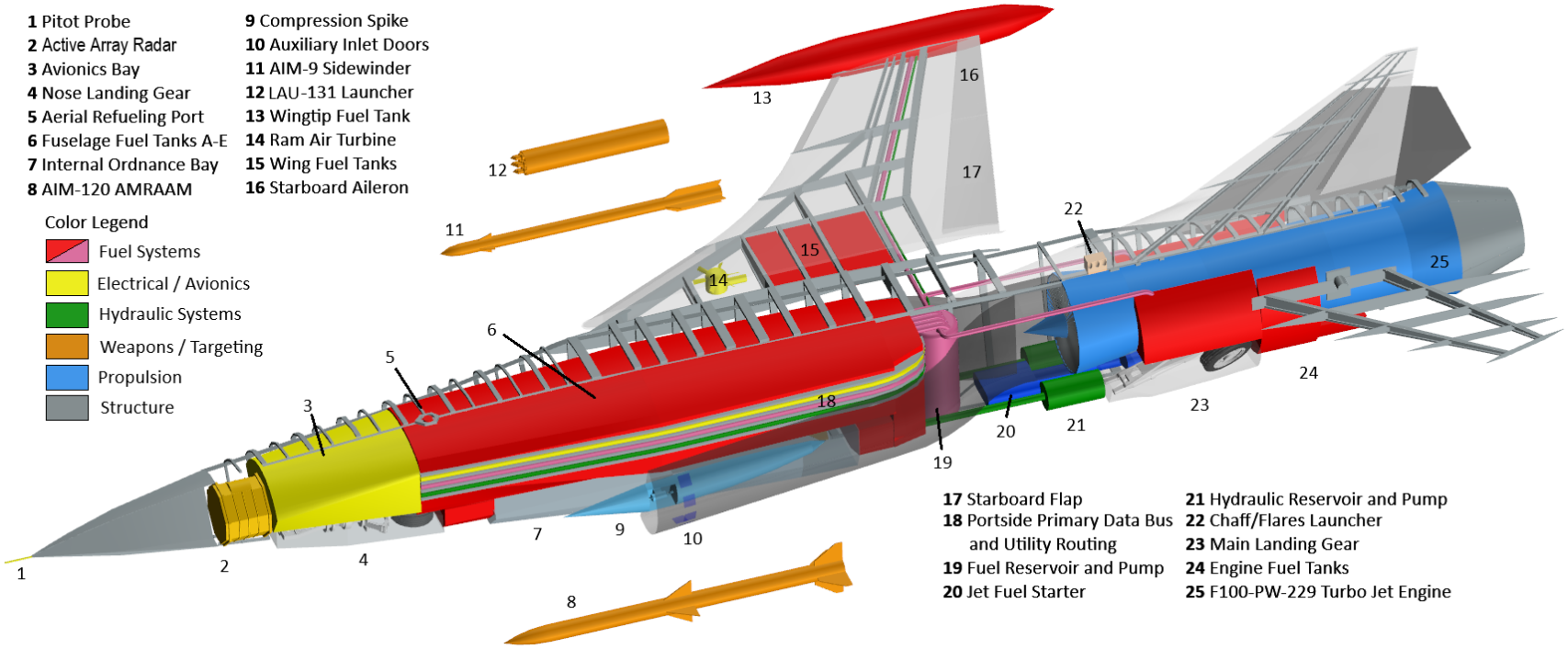

Fig. 9 Internal configuration layout of aircraft.

VI. Aerodynamics

An aircraft must be designed with careful consideration of the airflow regimes it is intended to operate. An aircraft not optimized for supersonic flight will struggle to break the sound barrier, as drag dramatically increases upon reaching the transonic speeds. Conversely, an aircraft over-optimized for supersonic flow may struggle to maintain efficient and controllable flight at low speeds. The Homelander is designed to operate effectively across both regimes of flight.

A. Wing Design

A supersonic aircraft's wing design is critical to its operation, providing the bulk of the lifting force in all regimes of flight. To properly balance performance in both subsonic and supersonic flow the Homelander uses a delta wing planform, featuring a highly swept leading edges (LE) to reduce wave drag during supersonic flight while also generating vortex-induced lift at lower speeds. The wing itself is defined by two fundamental design elements: the planform and the airfoil. Achieving strong performance in both supersonic and subsonic regimes requires careful optimization of both the planform geometry and the airfoil profile.

1. Planform Design

A vast variety of delta wing planforms exist, all with differing strengths and complexities. While the simplest approaches use a single straight LE sweep, more advanced designs vary this either continuously like the ogive delta seen on the Concorde or discontinuously like the compound delta used on the F-16 XL. These planforms both include higher sweep angles inboard than midspan. At a high enough angle of sweep this can act similarly to a LE extension or wing strake, creating vortices that delay flow separation increasing lift at high AoA [6]. This is a critical property of delta wings flying at low speeds that aids in take-off and landing.

The compound delta, also called the double delta, was selected for its ability to balance supersonic performance with improved subsonic efficiency. The highly swept inboard section benefits from vortex lift generation (at subsonic speeds, high AoA) while the outboard section increases the wingspan allowing more efficient subsonic flight versus a plain delta wing of equivalent aspect ratio. The LE sweeps are set such that at super-cruise the wing is entirely within the shock cone and at dash only the outboard section is supersonic. This reduces the local Mach number, delaying the peak in wave drag. The placement of shocks along these two sweeps at two different flight conditions is shown in Fig. 10.

Certain concessions were made to ensure this wing planform is acceptable for other disciplines, primarily stability and structures. The trailing edge is swept at straight 15 deg to allow for the design of effective control surfaces. A circular arc was used to blend the two sweeps together to avoid stress concentrations. Finally, a linear wing washout, varying from 0 deg at the root to 3 deg at the tip, is employed to improve stall characteristics across the span and prevent undesirable nose-up pitching moments near stall.

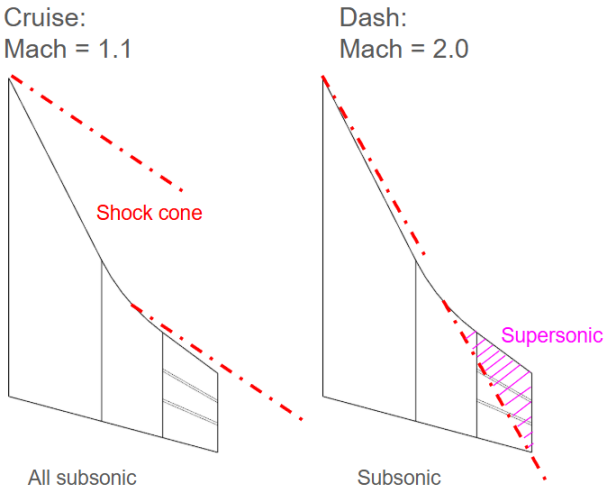

Fig. 10 Location of shocks on the wing at Mach 1.1 and Mach 2.

2. Airfoil Selection

Two broad categories of airfoils can be defined: supersonic and subsonic. Each has properties that suit them for one regime of flight over the other. For example, while a large LE radius promotes a higher $C_{l\max}$ it also creates drag heavy bow shocks in supersonic flow [7]. Sharp LEs like with a diamond airfoil create attached oblique shocks when supersonic, reducing wave drag [7]. However sharp LE airfoils struggle to produce adaquete lift at low AoA. Proper application of one airfoil type over the other is critical to a successful wing design able to operate in both air flow regimes.

A middle ground between these two categories is the NASA developed supercritical airfoil, with one such airfoil shown plotted in Fig. 11. This shape is designed to have good transonic performance without sacrificing acceptable low speed characteristics. The airfoil achieves this by pushing up the critical Mach number (M_{crit}), the point when flow over the airfoil hits Mach 1, essentially delaying the formation of transonic flow patterns and thus an increase in drag to a higher speed [6]. However, because of the rounded LE this airfoil still needs careful consideration of its use to avoid large drag spikes. Additional to its aerodynamic benefits, the supercritical airfoil typically has a larger enclosed area than a supersonic airfoil with an equivalent chord length, allowing more internal volume to store fuel, munitions, landing gear or any other necessary items.

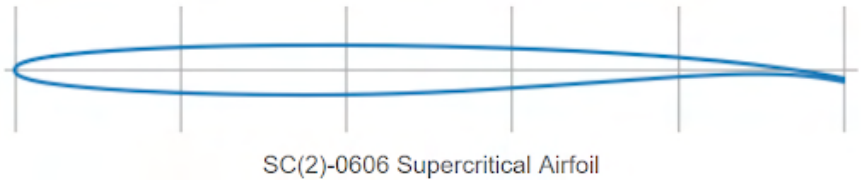

Fig. 11 A plotted supercritical airfoil.

Each member of the supercritical airfoil family is defined by a design lift coefficient and thickness ratio. However, the most critical property of a supercritical airfoil is its drag divergence mach number (M_{DD}) or the speed at which drag spikes due to shock wave formation. This is slightly different from M_{crit}, typically occurring a little later. Figure 12 shows M_{DD} for a number of different supercritical airfoils. The SC2-0606, seen in Fig. 11, was selected as one of the airfoils for the Homelander's two-airfoil design due to its desirable lift coefficient and adequately high M_{DD}.

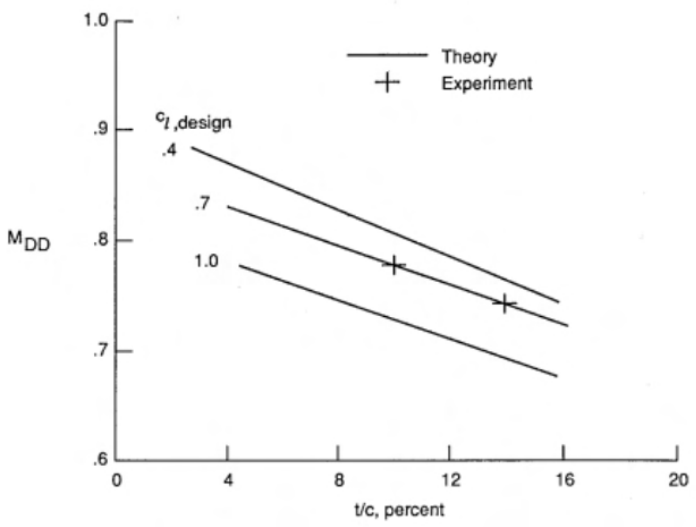

Fig. 12 Drag divergence Mach numbers for different supercritical airfoils [8].

Next, two supersonic airfoils were investigated: the hexagonal and biconvex. While a hexagonal airfoil is composed of six plates, four slanted and two parallel to the chord, the biconvex is two circular arcs. Examples are shown in Fig. 13. The hexagonal airfoil was opted for over the typical diamond airfoil as it better facilitates the integration of structures such as I-beams while offering comparable aerodynamic performance.

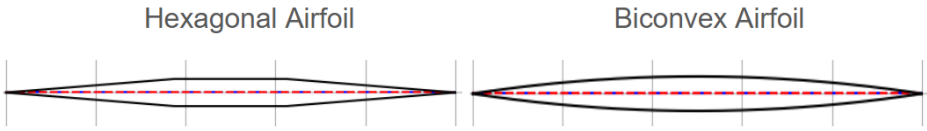

Fig. 13 Hexagonal and biconvex airfoils.

At supersonic speeds, the flow patterns around an airfoil can be predicted using oblique shock and Prandtl-Meyer expansion wave relations. From these relations, the surface pressures normalized by freestream pressure can be found and used to calculate sectional lift, drag, and moment coefficients. With techniques described by McCormick [7], a number of supersonic airfoils were simulated at varying angles of attack.

Camber was first studied with the results shown in Fig. 14. It is demonstrated that negative camber produces slightly higher lift at the cost of more drag. It is apparent that while biconvex airfoils produce comparable lift than their equally cambered hexagonal airfoil counterparts, they produce more drag.

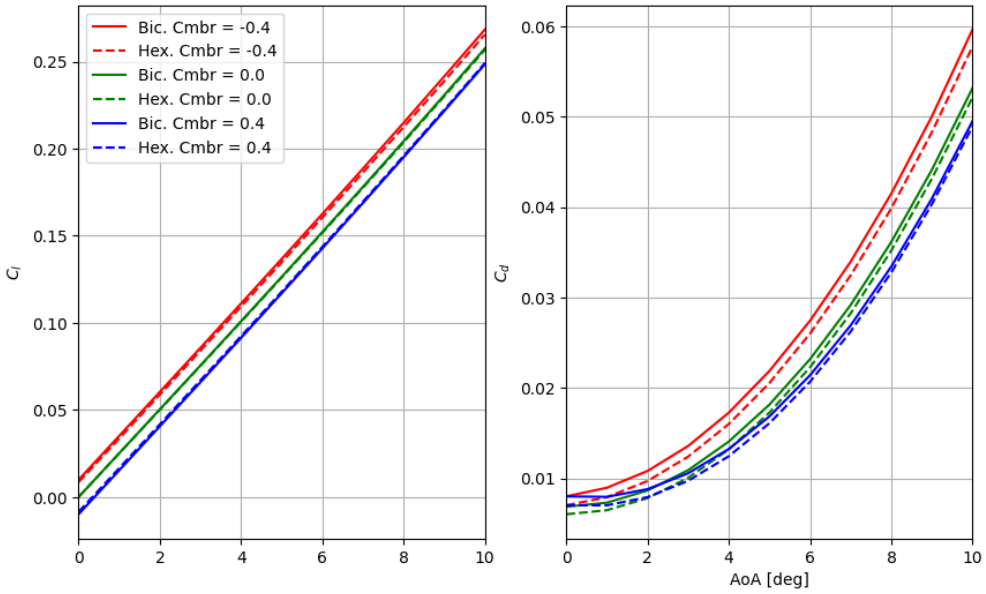

Fig. 14 Lift and drag of hexagonal and biconvex airfoils of varying camber.

The thickness to chord ratio was varied next, revealing a similar set of patterns in Fig. 15. A higher t/c correlates to a higher lift coefficient, which is exaggerated at higher angles of attack. The trend continued with biconvex airfoils producing marginally more lift for a penalty in drag compared to hexagonal airfoils.

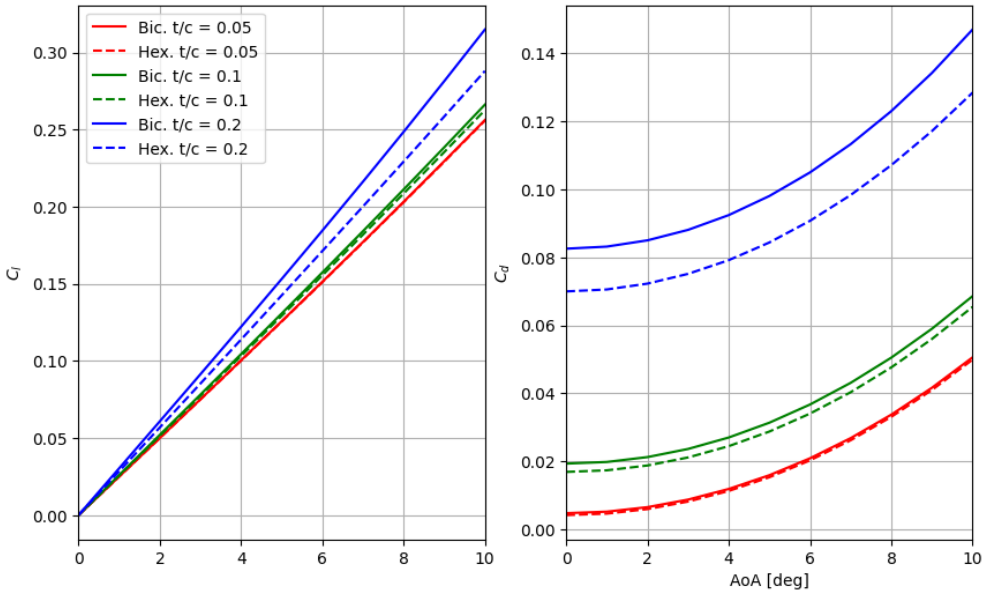

Fig. 15 Lift and drag of hexagonal and biconvex airfoils of varying t/c ratios.

From these two analytical studies it is clear that biconvex airfoils produce slightly more lift at the cost of some additional drag. One decisive advantage held by biconvex airfoils and why they are widely used for supersonic aircraft wings is a higher enclosed area, which usually allows for more efficient and thus lighter structures [9]. However, for the Homelander's wing planform, this airfoil will only be present near the wingtips, where a higher enclosed volume is less impactful. For this reason, hexagonal airfoils and their improved drag performance at supersonic speeds is chosen over biconvex airfoils. The 6% thickness hexagonal airfoil was chosen to match the SC2-0606's thickness. Thus, the airfoils used on the Homelander include the SC2-0606 in the inboard section, and a 6% thickness hexagonal in the outboard section.

3. Final Wing Design

Combining the previously defined planform and airfoil choices, an entire wing can be modeled. General dimensions and where the airfoil section changes is marked in Fig. 16 as well as additional important parameters including the wing reference area, aspect ratio, and taper ratio (λ). As previously mentioned, the wing planform was adjusted to include a mid-span transition that smoothly blends the two airfoils and leading edge sweeps together.

Parameter	S_{ref} [ft^2]	AR	λ
Value	300	2.5	0.248

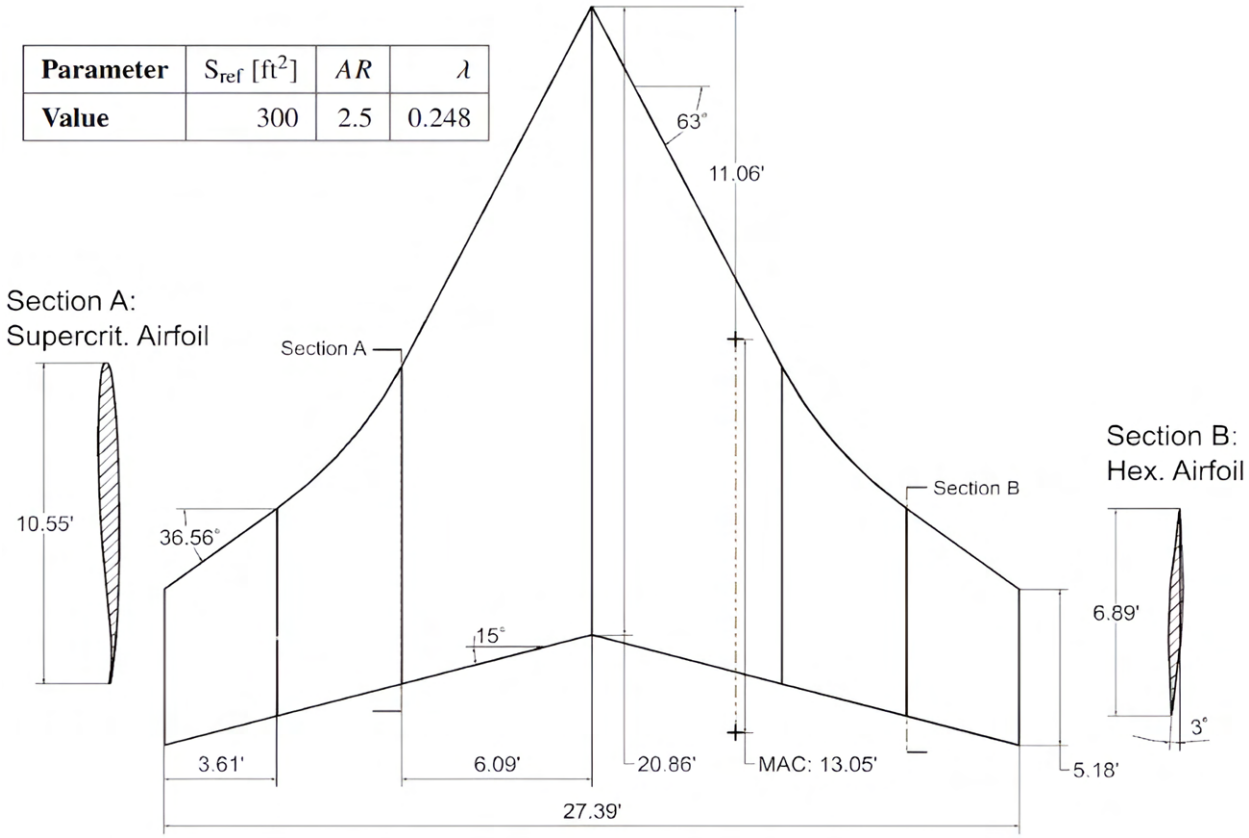

Fig. 16 Wing dimensions.

B. Aircraft Aerodynamic Model

Understanding and predicting the aircraft's lift, drag, and moment coefficients at different points in flight is critical to accurately assessing its performance. A variety of methods and theories were applied, applicable to different conditions and flow regimes during flight.

1. Lift Estimation

The subsonic lift model used is the leading-edge suction analogy created by Edward C. Polhamus. This method was developed for delta wings and better captures the effect of high lift vortices versus other methods [10]. The calculation of C_L is shown below in Eq. 1.

$$C_L = K_P \sin(\alpha)\cos^2(\alpha) + K_V \cos(\alpha)\sin^2(\alpha) \tag{1}$$

This equation is split into two components derived from different flow patterns: potential lift and vortex lift [11]. Each source has its own coefficient, K_P and K_V respectively, determined by the wing's aspect ratio from figures presented by Polhamus [10]. Figure 17 computes Eq. 1 for the given wing geometry across a sweep of AoAs, additionally plotting the potential and vortex lift components as well as slender wing theory for comparison.

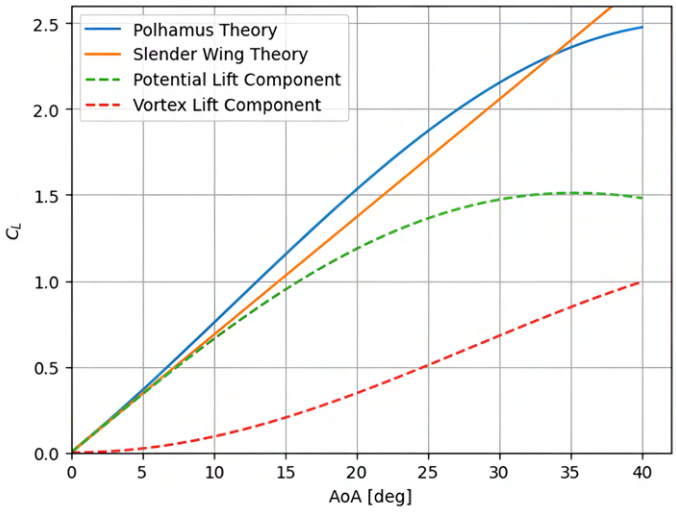

Fig. 17 Application of Polhamus Method compared to Slender Wing Theory.

Lift at transonic and supersonic speeds is hard to estimate. One exceptionally easy and often valid assumption to make is steady level flight, where the lift coefficient is set to maintain the aircraft's altitude at a given weight and speed. If the required coefficient can't be obtained at level flight, an additional trim drag penalty must be applied. Another, more preferred, route to determine supersonic lift is computational fluid dynamics software, discussed in a later section.

2. Maximum Lift Coefficient and High Lift Devices

To produce adequate lift and avoid stall at high angles of attack or low airspeeds, slats and plain flaps are employed. The flaps are critical to boosting the C_{Lmax} ensuring take-off requirements are met. Slats work by increasing high pressure airflow over the top surface of the wing, suppressing boundary layer growth and delaying flow separation. These devices combined increase lift generation and increase the AoA range the aircraft can operate at while maintaining control.

To quantify the ΔC_{Lmax} benefit of high lift devices it is typically best to use wind tunnel testing. However, with empirical data and known geometry an estimation using methods described by Raymer [6] can be obtained. Using control surface geometry described in the Stability & Control Section X, it is found the flaps add 0.415 to the clean C_{Lmax}. Combined with the previously described Polhamus Method, C_{L} at a given AoA can be predicted, shown in Fig. 18.

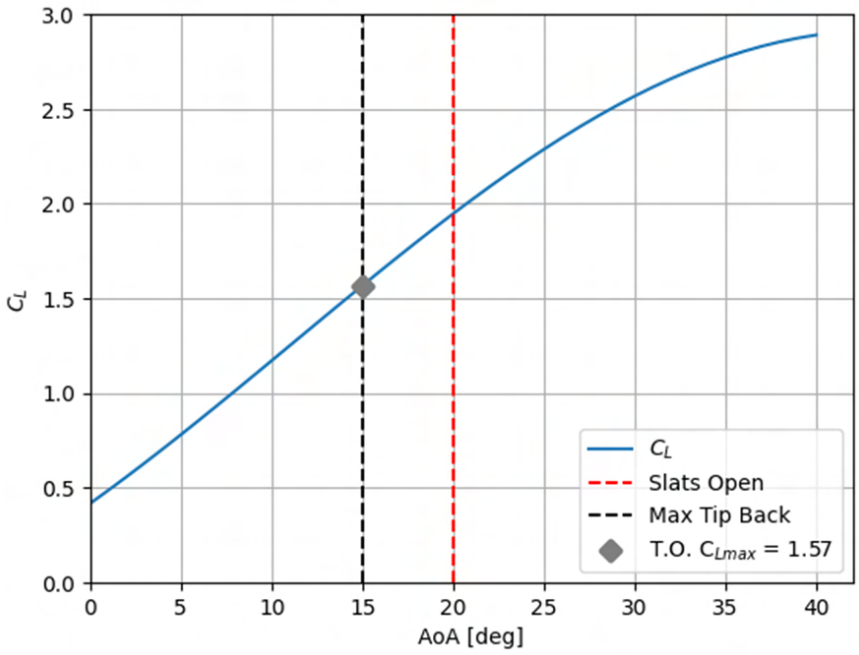

Fig. 18 C_{L} versus angle of attack.

The C_{Lmax} attainable during take-off is constrained by the maximum tip back angle of 17.5 deg shown in the Landing Gear Section XIII. Using a tip back of 15 deg (providing some safety margin), results in a take-off C_{Lmax} of 1.57. Additionally, shown in Fig. 18 is the AoA at which the leading edge slats automatically deploy. When they are not needed, the slats are closed, presenting a clean wing surface reducing drag particularly at high speeds. Prompted by the aircraft's onboard computer the slats open during high AoA maneuvers to prevent flow separation.

3. Drag Buildup

At subsonic speeds, the two primary components of drag are parasitic skin/pressure drag (C_{D_0}) and induced drag (C_{D_i}). With the geometry of the aircraft defined, wetted areas were collected from CAD and used to perform a part-by-part buildup of C_{D_0}. These wetted areas are shown in Table 7. With these numbers, the parasitic drag can be calculated at various altitudes and Reynolds numbers. The part-by-part parasitic drag build up and the calculations of induced drag were completed with methods described by Raymer [6].

Table 7. Aircraft Component Wetted Areas

Component	**Fuselage**	**Wing**	**Tail Surfaces**	**Total S_{wet}**	**Total S_{wet} / S_{ref}**
Wetted Area [ft^2]	819.6	352.6	290.8	1,463.0	4.88

Supersonic wave drag (C_{D_w}) is calculated with the NASA developed Delta Method. This method uses empirical data to turn aircraft geometry and flight conditions into a drag coefficient. It was conceived using data from 19 subsonic and supersonic military aircraft, estimating C_{D_w} near cruise conditions from the range of Mach 0.4 to 2.0 [12]. Both wave drag and parasite drag are plotted in Fig. 19.

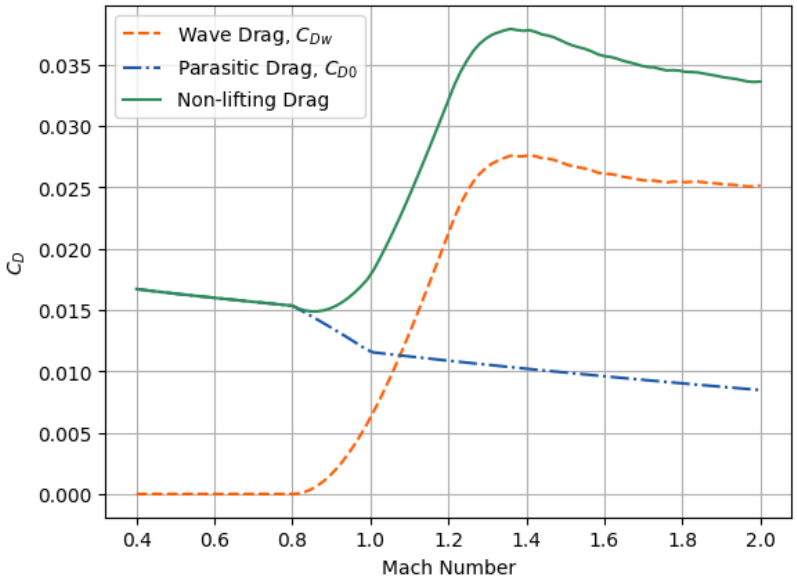

Fig. 19 Parasitic and wave drag coefficient across a range of Mach numbers.

Another means of quantifying wave drag is through the Area Rule Method. Developed from supersonic slender body theory, this process measures a number of slices through the aircraft to quantify generalized wave drag [9]. This method directly takes in the 3D outer mold line (OML) and flight conditions and generating a wave drag coefficient calculated from the integral in Eq. 2 [9].

$$C_{D_w} = \frac{-1}{2\pi S_{\text{ref}}} \int_0^l \int_0^l S''(x) S''(\xi) \ln(x - \xi)\, dx\, d\xi \tag{2}$$

The surface area at each slice, $S(x)$, is taken by measuring an STL file with Python code. At Mach numbers greater than one, the slices were taken at the Mach angle and at a number of roll angles between 0 and 180 deg before being averaged. This area distribution can then be compared to a Sears-Haack body of identical length and volume which has the lowest theoretical wave drag. The analyzed OML and area distribution with a Sears-Haack body comparison is given in Figs. 20a and 20b respectively.

(a) OML used for Area Rule measurements with the subtracted intake in red.

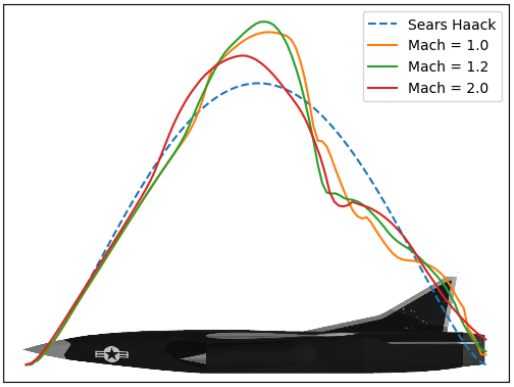

(b) Area distribution at different Mach numbers compared to a Sears-Haack body.

Fig. 20 Area ruling inputs and results.

The percent error between the aircraft's area distribution and the that of the Sears-Haack body can be calculated. This gives a numerical measurement indicating how closely the two distributions match. As can be seen in Table 8, the error decreases as Mach number increases, indicating the aircraft becomes more aerodynamically efficient the faster it flies. Note this does not necessarily mean a decrease in drag force, as dynamic pressure increases with the square of the airspeed.

Table 8. Percent Error between the Homelander's Area Distribution and the Sears-Haack Body

Mach Number	1.0	1.2	1.6	2.0
Percent Error	15.28%	14.79%	12.96%	11.06%

Three aircraft configurations are considered in the drag model: a clean aircraft, all external fuel stores (DCA patrol mission), and wingtip mounted AIM-9s. These configurations add wetted area and volume to the aircraft. These stores have a minimal impact on wave drag as per the Delta Method. The non-lifting C_D of these different configurations is plotted in Fig. 21.

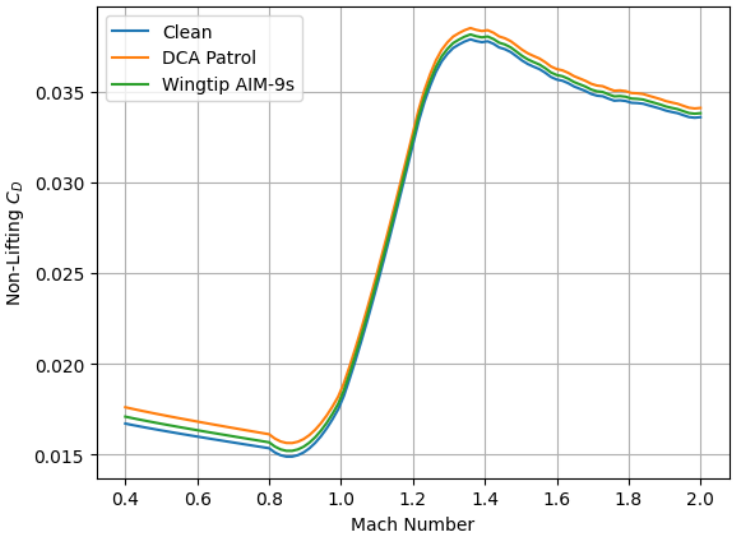

Fig. 21 Non-lifting drag of different aircraft configurations.

4. CFD Analysis

With the aircraft's OML fully realized in CAD, CFD could be performed. FlightStream, a vortex panel method, was used to verify the aircraft's properties at low speeds, with an instance shown in Fig. 22a. Using the wing model, a large sweep was ran across six mach numbers from 0.3 to 0.9 and six AoAs from 0 to 10 deg. The results of this sweep are shown in Fig. 22b. At subsonic speeds, it is apparent the L/D ratio peaks at a high AoA and a Mach number of 0.4.

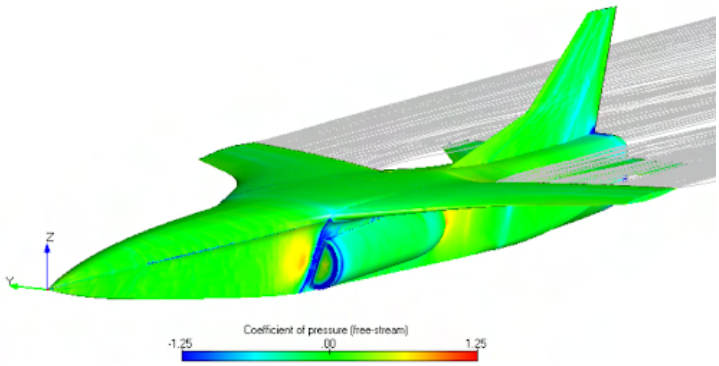

(a) FlightStream coefficient of pressure on the aircraft at Mach 0.6, 1 deg AoA.

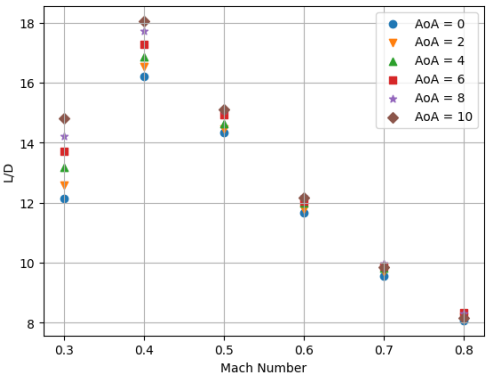

(b) Results of FlightStream sweep.

Fig. 22 FlightStream aircraft analysis.

SU2, a Compressible Euler CFD software capable of simulating compressible supersonic flow, was used to analyze the wing's properties at high Mach numbers. Paraview was then used to visualize the results making the pressure distribution on and around the wing visible, shown at Mach 1.2 and 2.0 in Figs. 23a and 23b respectively. These images confirm the shock wave locations shown prior in Fig. 10, as well as demonstrating the outboard section being supersonic with an attached oblique shock on its LE visible by the spike in pressure.

(a) Pressure distribution around wing in Mach 1.2 flow.

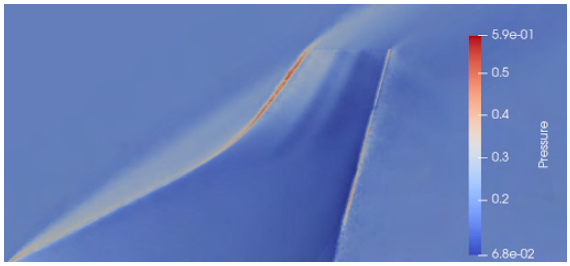

(b) Pressure distribution around wing in Mach 2.0 flow.

Fig. 23 SU2 Wing Analysis.

Results from SU2 for a sweep of AoAs from 0 to 4 deg was performed at various Mach numbers, with data plotted in Fig. 24. Because of the immense dynamic pressure acting on the wing C_{L} requirements for steady flight are met within these AoAs.

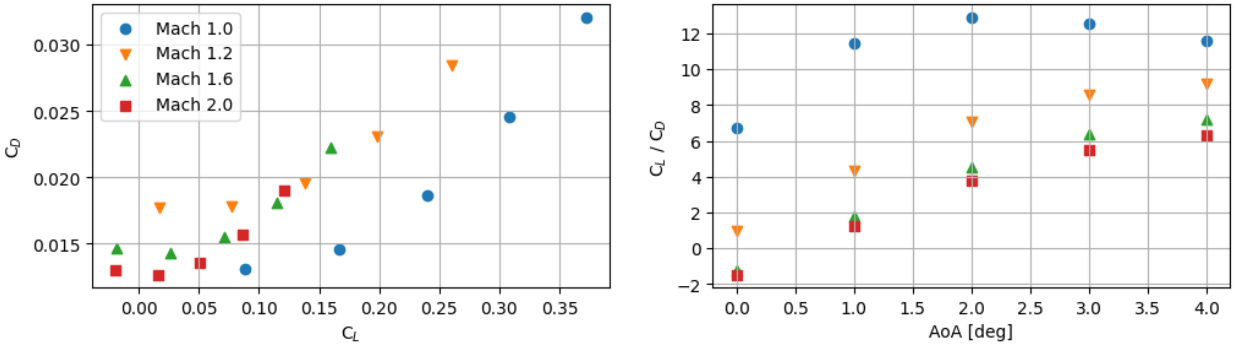

Fig. 24 Wing C_L and C_D from SU2 in a sweep of AoA and Mach.

5. Completed Aerodynamic Model

With a completed lift and drag model, the aircraft can be simulated at a number of different test conditions. The three required inputs to obtain lift and drag coefficients are Mach number, altitude and aircraft weight. This model is used in the Performance Section VIII to obtain estimates of fuel burn and ensure key requirements are met. The data is outputted below in Figs. 25a to 25c as a series of L/D plots with two varieties, either holding a constant Mach and sweeping altitudes and weights or a constant altitude and sweeping over Mach numbers and weights. They were created at critical aircraft mission conditions such as cruise, dash and loiter as well as approaching the Mach pinch near M = 1. These aerodynamic performance plots meet the validation requirements outlined in MIL-HDBK-516C Section 6.3.2 for demonstrating compliance across critical mission conditions.

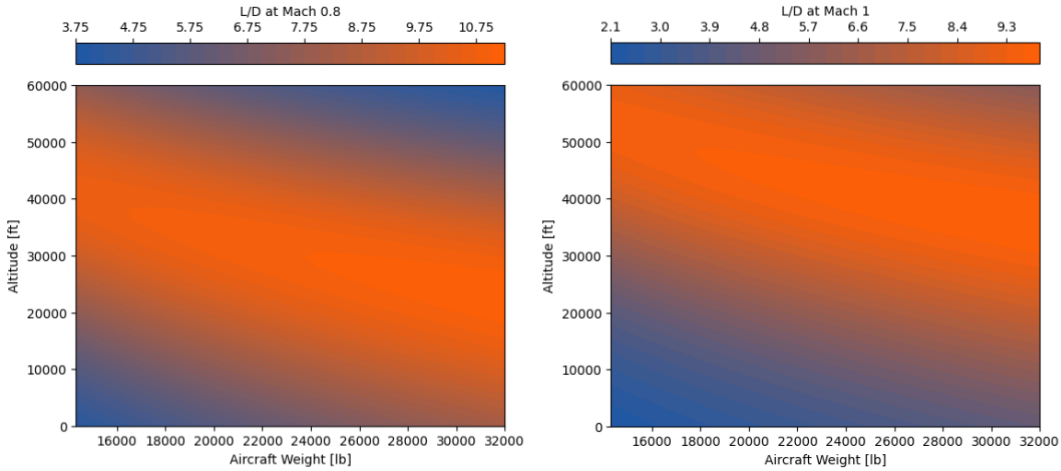

(a) L/D plots at Mach 0.8 and 1.0, where wave drag begins to rise.

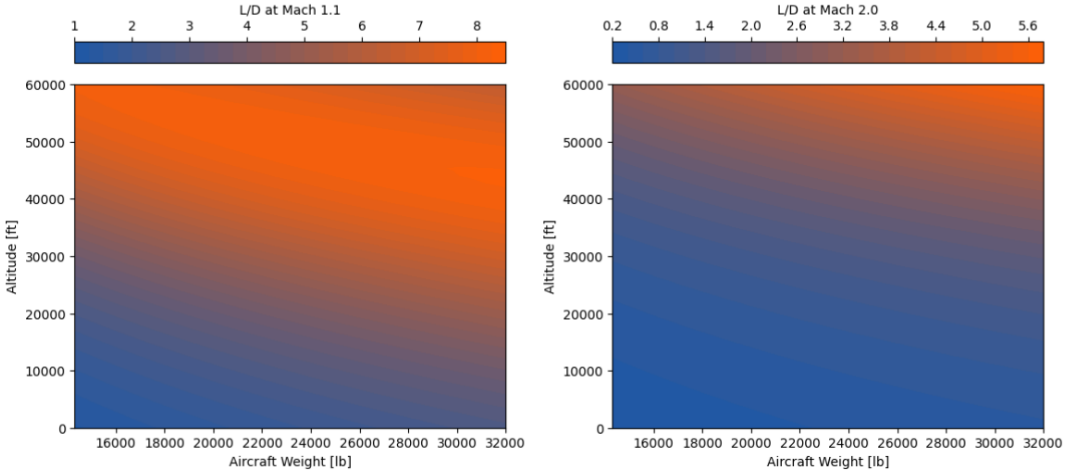

(b) L/D plots at Mach 1.1 and 2.0, cruise and dash conditions

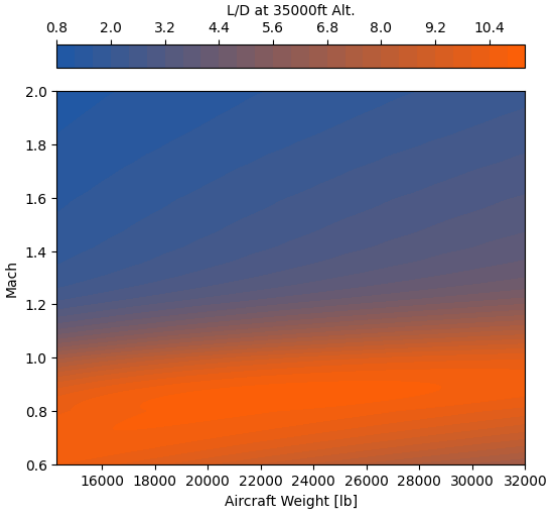

(c) L/D plots at 35,000 ft for loiter.

Fig. 25 L/D plots at varying Mach numbers and altitudes, in the clean configuration.

VII. Propulsion

In this section, the engine selected, criteria for engine selection, and simulated engine performance is discussed. Furthermore, inlet sizing/performance is discussed as well to provide insight on how the wide range of the thrust requirements was enhanced with the chosen inlet design. A trade study regarding high vs. low bypass ratio (BPR) engine is examined to further justify the selected engine choice.

A. Engine Selection Methodology and Thrust Requirements

During the design process, engine selection was critical in balancing three different drivers the team determined to be critical: cost, thrust, and fuel consumption. With a $25 million budget, this ruled out twin-engine configurations early in the design process due to significant portion of the budget becoming dedicated to propulsion alone. Furthermore, the team's desire for super-cruise and a Mach 2 dash meant that a high thrust engine would be needed for the demanding thrust requirements. To maintain the balance between high thrust performance and minimum fuel consumption, a low BPR turbofan engine with afterburners was chosen as they are industry standard for similar aircraft such as the F-16 [13]. With these considerations in mind, the F100-PW-229 was chosen as the engine to be used in the Homelander as the team determined this engine balanced the cost, thrust, and fuel consumption tradeoff. Figures 26 and 27 show the placement of the PW-229 (highlighted in blue) in the aircraft's CAD model and the cutaway of the actual engine, respectively. Table 9 summarizes the specifications of the PW-229, which were crucial in creating a simulated version of the PW-229 in GasTurb 14 software to generate thrust, TSFC, and fuel flow data.

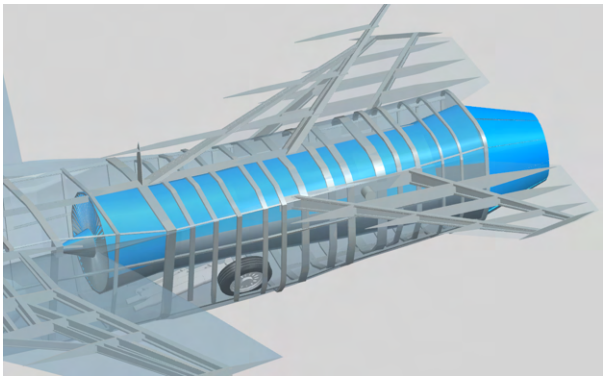

Fig. 26 PW-229 placement in CAD model.

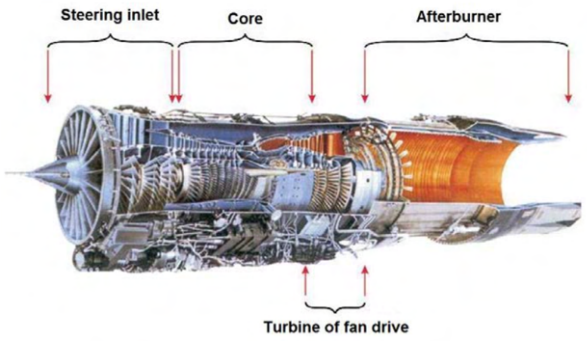

Fig. 27 Cutaway of PW-229 engine [14].

Table 9. F100-PW-229 Engine Specifications [15][16]

Specification	Value
Static SL Dry / Wet Thrust [lb]	17,800 / 29,100
Static SL Dry / Wet TSFC [lb/lb-hr]	0.726 / 2.06
Static SL Mass Airflow [lb/s]	254
BPR	0.36
OPR / FPR	32.4 / 3.8
Turbine Inlet Temperature [°R]	2,916
Length [in]	191
Dry Weight [lb]	3,876

Specification	Value
# of HPC Stages	10
# of HPT Stages	2
# of LPT Stages	2
# of Spools	2
# of Fan Stages	3
Fan / Max Diameter [in]	34.8 / 46.5
Nominal Spool Speed [RPM]	10,500

B. Propulsion Trade Study: Low vs. High BPR Engine

The most constraining mission segment required by the RFP was determined early on to be the DCA patrol mission's loiter segment, as this requires the aircraft to fly at low thrust/drag conditions and minimal fuel consumption. During the design process, BPR dictates what the fuel consumption would be where higher BPR allows for high fuel economy, but with the a tradeoff of overall lower thrust output. In the Homelander's design, the trade-off between high-speed maneuverability for rapid intercepts, fuel efficiency, and engine cost for sustained four-hour loiter was primarily influenced by the selection of engine BPR. One other engine studied for the use on the Homelander, the F110-GE-132, has a BPR of 0.68 [17], almost double that of the PW-229. Using specification information for the GE-132 [15][16], GasTurb 14 can be used again to generate TSFC, thrust, and fuel flow data. Since the four hour loiter was the most constraining, this was considered as the benchmark case to compare the two engines at whether any fuel savings from the GE-132 was worth it. Figures 28 and 29 show the results of simulating the PW-229 and GE-132 in GasTurb 14 and compares them at loiter conditions for TSFC and thrust requirements.

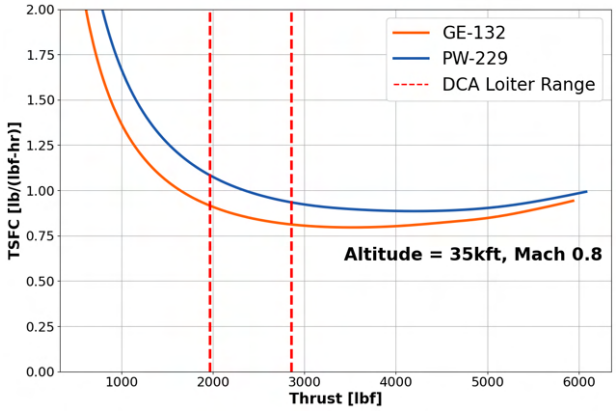

Fig. 28 TSFC vs. thrust for both engines at loiter.

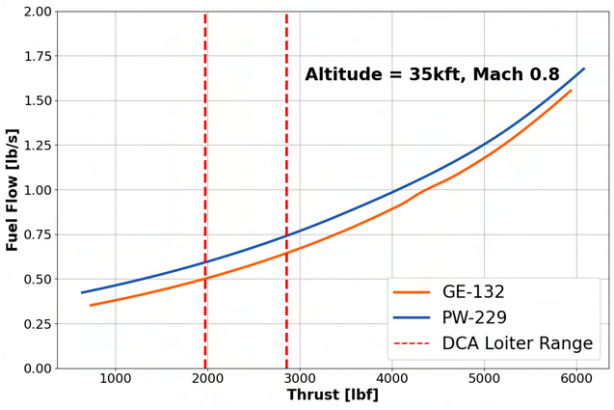

Fig. 29 Fuel flow vs. thrust for both engines at loiter.

Figure 28 shows lower overall TSFC at loiter conditions for the GE-132 compared to the PW-229, while Fig. 29 shows the expected lower fuel consumption for the GE-132. Although fuel flow improves with the higher BPR GE-132, the benefits are only slight as shown in Fig. 29, where there is only an average of 15% decrease in fuel flow when switching from the PW-229 to the GE-132. Despite the fuel consumption benefits of the GE-132 at loiter, cost was still a factor that needed to be maintained. Nicolai contains engine cost data specifically for the F100 and F110 family of engines based on max thrust output [9], which was used for determining engine unit cost. Using max sea level static thrust for the PW-229 in Table 9 and GE-132 (32,500 lb) [16], the following costs can be determined:

Table 10. Cost Analysis Results of PW-229 and GE-132

Engine Model	Unit Engine Cost (2024 USD)	Aircraft Cost (Millions, 2024 USD)
F100-PW-229	$5,479,300	24.7
F110-GE-132	$5,891,200	25.1

Table 10 shows that even with an average of 15% reduction in fuel economy, the aircraft would still run over the $25 million budget with the GE-132 installed and thus not satisfy the cost requirements. This stems from the fact that although the GE-132 has a higher BPR, it also is rated at a higher max sea level static thrust, which is what the Nicolai engine cost estimation is based upon [9]. Furthermore, the GE-132 proved to have issues reaching lower thrust outputs for even the minimum dash requirements of Mach 1.6, due to the increased thrust penalties when increasing the BPR. So even though there are fuel savings benefits, the unitary cost outweighs any weight savings. Therefore, this resulted in the team still selecting the PW-229 for its cost savings, exceptional performance for higher thrust maneuvers, and balanced fuel economy for low thrust segments.

C. F100-PW-229 Engine Performance and Thrust Requirements

With the PW-229 engine specifications outlined in Table 9, simulations were conducted at various altitudes and Mach conditions using GasTurb 14 software. After confirming GasTurb 14 outputs closely matched PW-229 specifications at sea level static conditions, the resulting data set provided thrust, TSFC, and fuel flow values for the engine. These data were then used by the performance lead to determine Homelander's thrust requirements and fuel needs for each mission segment. Figures 30–35 show the PW-229 simulation results for relevant mission segments, and Table 11 lists the exact thrust requirements. Nicolai's Chapter 16 method for applying thrust penalties to installed thrust values from GasTurb 14 was used [9], resulting in approximately a 4% reduction in thrust relative to the simulated values. Additionally, a 2% bleed mass flow was allocated for environmental control and avionics liquid cooling, and a 50 kW power extraction was applied for electrical and hydraulic demands as required by the RFP [1]. These effects were incorporated into the GasTurb analysis and are reflected in Figs. 30–35.

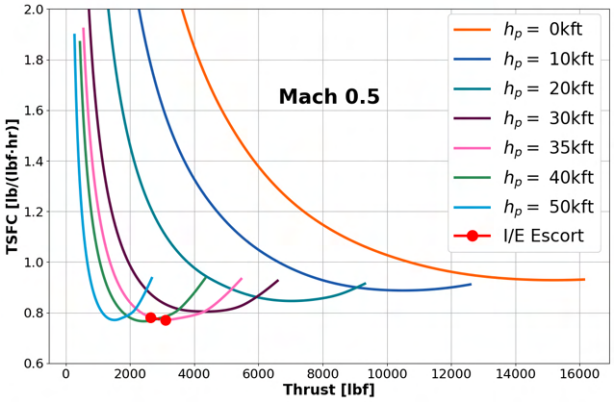

Fig. 30 PW-229 no AB Mach 0.5 performance.

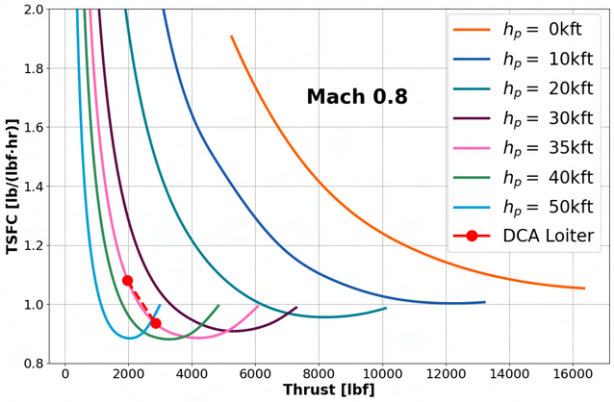

Fig. 31 PW-229 no AB Mach 0.8 performance.

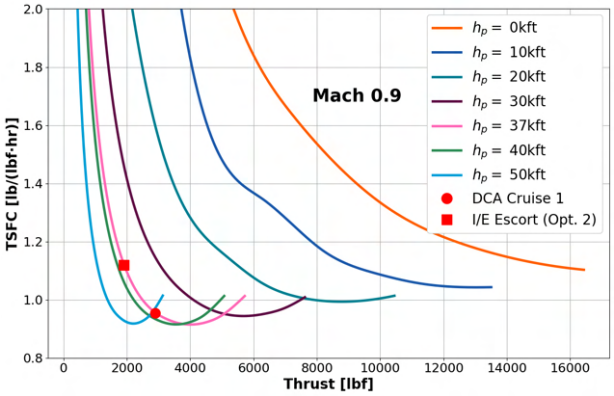

Fig. 32 PW-229 no AB Mach 0.9 performance.

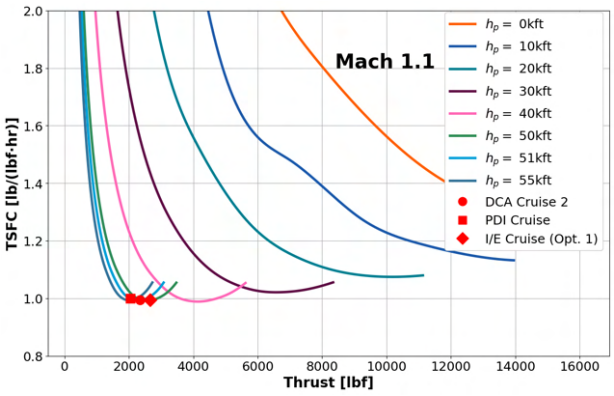

Fig. 33 PW-229 no AB Mach 1.1 performance.

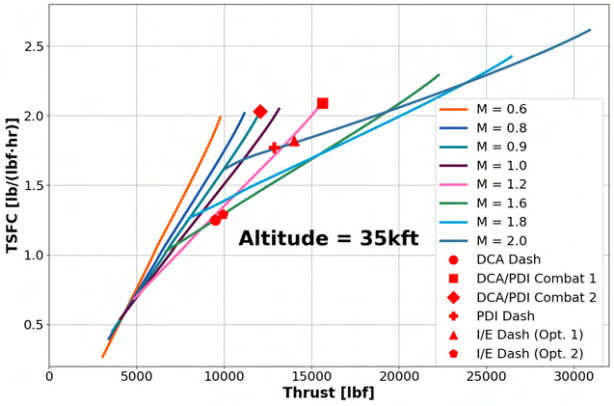

Fig. 34 PW-229 AB performance.

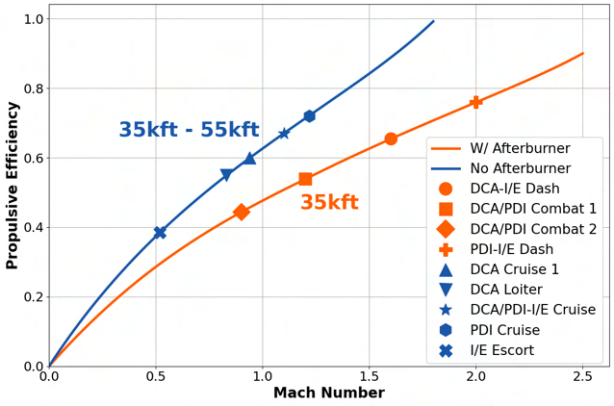

Fig. 35 PW-229 propulsive efficiency.

Table 11. Thrust requirements of mission segments of interest

Mission	Altitude [kft]	Mach	Thrust [lb]
DCA Cruise 1+2	35, 51	0.9, 1.1	(2,374-2,499), (2,316-2,469)
DCA Loiter	35	0.8	(2,026-2,897)
DCA Dash	35	1.6	(9,552-9,584)
PDI Dash	35	2.0	(12,830-12,878)
PDI Cruise	55	1.1	(2,050-2,121)
DCA/PDI CA 1+2	35, 35	1.2, 0.9	(15,639), (12,080)
I/E Escort	35	0.5	(2,840-3,375)
I/E Escort	35	0.5	(2,840-3,375)
I/E Cruise (Opt. 1+2)	50, 35	2.0, 1.6	(2,292-2,543), (1,704-1.886)

The chosen PW-229 engine tends to operate close to the TSFC "bucket" for the segments requiring no afterburners in Figs. 30 - 33, which helps keep fuel flow to a minimum even for the Mach 1.1 super-cruise segments. Figure 33 helped justify the choice of the PW-229 since it allowed for the Homelander to achieve super-cruise speeds and remain within the "bucket" of the TSFC curve for minimized TSFC/fuel consumption because of the engine's wide range of thrust capabilities. The cases requiring afterburners in Fig. 34 show dash segment thrust requirements being met, while also showing that the engine would not be operating too close to the minimum or maximum dash thrust capabilities at the desired speeds. Finally, the propulsive efficiency values for the simulated mission segments, shown in Fig. 35, are also based on PW-229 engine simulation data generated using GasTurb 14. The results indicate that most mission segments of interest operate within regions of high propulsive efficiency, contributing to overall fuel savings.

D. Inlet Design

For inlet design, Nicolai inlet area sizing was used for the inlet entrance [9]. This method was chosen because it incorporated mass flow rate into the calculation, which made the final area calculation more representative of the PW-229's mass flow needs in order to operate. This meant that the design Mach mass flow rate obtained from GasTurb data could be used to size the inlet entrance area, which was done at a design Mach of 1.8. This design Mach choice was not set to Mach 2 (the aircraft's maximum dash speed) because lowering the design Mach allowed a balance between mass flow needs at Mach 2 and the lower speed mission segments since the aircraft inlets needs to provide adequate mass flow in both regimes. Since the aircraft will be achieving Mach 2 speeds, a movable external compression spike was implemented because of the large reduction in pressure recovery that occurs at higher speeds with a one shock inlet. With an external compression spike, the two shock system this creates allows for better pressure recovery in the inlet, which then allows for more efficient thrust production at high speeds. It also will not be fixed and can move to help optimize pressure recovery at off-design speeds/altitudes. This inlet integration approach satisfies MIL-HDBK-516C Section 5.2.3 requirements for mounting security and performance across flight regimes.

Since a compression spike was implemented, an S-duct, twin side mounted inlet was chosen due to the clean airflow side mounted inlets provide. Also, other high speed industry interceptors, such as the Dassault Mirage 2000 [18], use external compression spikes for better high speed performance. This is important for the I/E mission's dash segment that shows off the capabilities of the Homelander, so optimal thrust and pressure recovery is needed for such long dash segments. Furthermore, a channel-type boundary layer diverter was chosen since this is also the diverter used by the Dassault Mirage [18], which was sized using Nicolai's Chapter 16 boundary layer height calculation at the same design Mach 1.8. Furthermore, Nicolai's pressure recovery curve for the two shock system [9] was implemented through GasTurb's intake map feature in order to generate Figs. 30 - 35 to get more accurate results for the aircraft's specific two shock inlet system. Figure 36 shows the results for the pressure recovery of this two shock system implemented into GasTurb, which is also compared to a one shock system and MIL-E-5008B standard pressure recovery schedule.

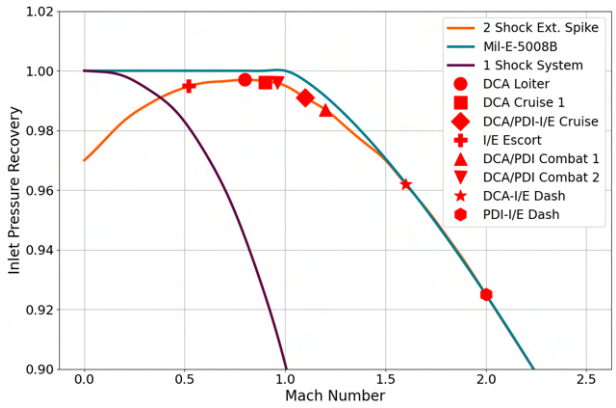

Fig. 36 2 shock inlet with mission segments.

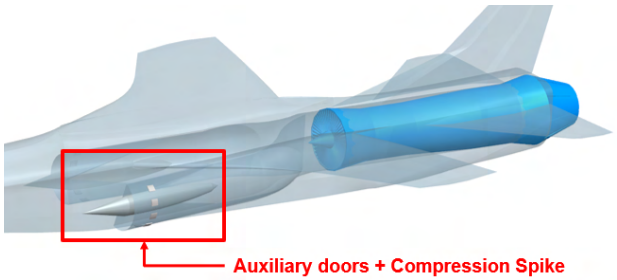

Fig. 37 Inlet routing in CAD model with compression spike and auxiliary doors.

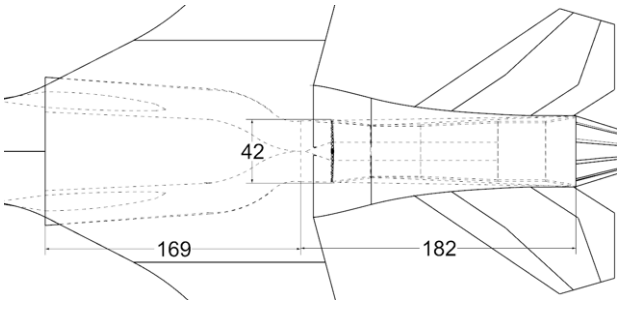

Fig. 38 Inlet S-duct dimensions [in.].

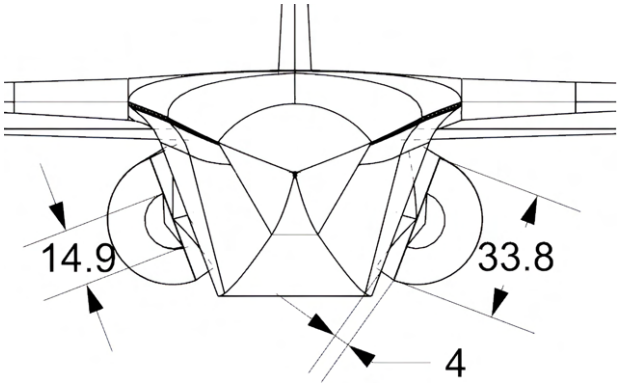

Fig. 39 Inlet entrance and boundary layer diverter dimensions [in.].

Figure 37 shows the full inlet CAD implemented with both the external compression spike and auxiliary doors. Similarity analysis with the F-16 inlet's area, which has auxiliary doors and utilizes the same PW-229 engine [19], found that the team's aircraft had comparable inlet area to the F-16. Thus, the team's aircraft had auxiliary doors implemented to help with airflow during engine startup. To further aid engine startup, a jet fuel starter (JFS) was implemented, so as not to require flight crew to provide startup by external means. JFS is important for the PDI mission, as quick scramble time is important for arriving to an adversary, which JFS helps shorten the time from ground to taking off. Furthermore, for engine out conditions, a ram air turbine plus batteries was chosen to aid in a loss of power so that a pilot can still control the flight system and have some time to get the aircraft on the ground before full loss of power. These systems for engine out and take-off conditions are elaborated more in the Systems Section XIV. Figures 38 - 39 show the results of the inlet and boundary layer diverter height sizing done from the Nicolai methods mentioned above. Nicolai also had methods to minimize pressure recovery loss based on duct length to inlet height ratio, which also aided in determining these dimensions [9].

VIII. Performance

This section presents a comprehensive performance evaluation of the proposed aircraft design. Design decisions from the Aerodynamics and Propulsion disciplines have been integrated and assessed collectively. The analysis includes take-off and landing performance, flight condition optimization strategies, and mission modeling through time-step integration. Additionally, the flight envelope has been examined with respect to performance limits and operational constraints. The resulting performance characteristics are discussed in detail and demonstrate that the design exceeds the expectations outlined in the RFP [1].

A. Take-off and Landing Distance Analysis

To initiate the performance evaluation, it was essential to verify whether the design put forth meets the take-off and landing distance requirements specified in the RFP [1]. Table 12 provides a concise summary of the calculated values corresponding to the current design configuration.

For take-off and landing analysis, a constant C_{Lmax} of 1.57 was used, corresponding to a 15 deg AoA constrained by the tip-back angle of the main landing gear. As shown in Table 12, transition distances exceed ground roll values due to higher climb gradient requirements for take-off. The aircraft is assumed to complete the rotation arc at the maximum feasible climb angle under full thrust, not just the minimum obstacle clearance, ensuring a smoother and more efficient transition to mission climb altitudes. Variations in distance result from changes in air density with altitude and Delta ISA conditions typical of cold or icy environments, which also affect the coefficient of friction. These factors are similarly reflected in the landing field length analysis.

Table 12. Take-off and Landing Performance under Varying Conditions

Altitude	Runway Type	Weight [lb]	Flare / Transition [ft]	Ground Roll [ft]	Total [ft]
Sea Level	Asphalt	31,034	3,150	2,800	5,950
Sea Level	Asphalt	22,452	3,400	1,300	4,700
4,000	Asphalt	31,034	3,600	3,200	6,800
4,000	Asphalt	22,452	3,750	1,500	5,250
Sea Level	Icy	31,034	3,050	2,400	5,450
Sea Level	Icy	22,452	3,300	1,100	4,400
4,000	Icy	31,034	3,400	2,850	6,250
4,000	Icy	22,452	3,550	1,150	4,700
Sea Level	Asphalt	17,300	650	2,470	3,120
4,000	Asphalt	17,300	730	2,350	3,080
Sea Level	Icy	17,300	650	2,500	3,150
4,000	Icy	17,300	730	2,700	3,430

Given the characteristics of the designed landing gear, particular attention was paid to selecting braking coefficients that prevent overheating of the tires and braking systems. Consequently, the landing ground rolls exhibit similar values across conditions, even though in some cases were expected to be lower if not similar. Although colder, high-altitude environments could allow more aggressive braking, still standard braking parameters were adopted to prevent wheel spin or skidding. All computed distances remain comfortably within the 8,000 ft limit specified in the RFP [1].

B. Optimal Speeds and Altitude Determination

The optimal cruise and loitering speed is traditionally identified by maximizing various aerodynamic efficiency metrics such as C_L/C_D, $C_L^{0.5}/C_D$, $C_L^{1.5}/C_D$, or $C_L/C_D^{1.5}$, while ensuring engine operability, specifically, maintaining positive net thrust. These textbook-based criteria are widely used and are theoretically ideal to determine optimum cruise velocities and altitudes for maximizing jet endurance or range under fixed altitude or throttle conditions. However, with simulated real-time engine performance data, these methods prove inadequate. They do not account for fuel flow variations or the continuous reduction in weight due to fuel consumption, both of which significantly influence the optimal flight condition at any given moment. To capture these dynamic effects, the team implemented a grid search across a broad range of flight conditions to identify representative solutions that reflect true mission-averaged performance.

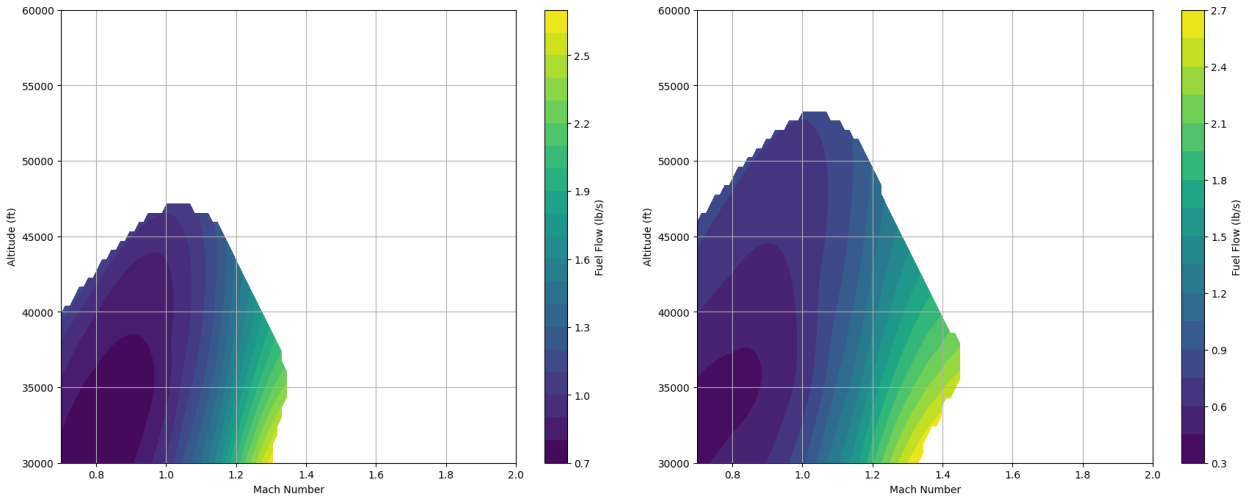

(a) MTOW **(b) Maneuver weight**

Fig. 40 Optimal flight conditions plotted against their fuel flow.

As shown in Fig. 40, this approach facilitates the selection of optimal altitudes and speeds for fuel-intensive mission phases such as loiter. For example, the loiter speed was determined by performing time-step integration over the entire loiter segment, choosing a different optimal speed at every time step to minimize the fuel burn. Then, with that minimal fuel burn integration, a grid search was setup, that finds a velocity which when constant throughout the phase yields the same number by the end with an acceptable tolerance. Similarly, the cruise velocity was selected by maximizing the specific range ($V/\dot{m}_f$), thereby ensuring an efficient balance between speed and fuel consumption. This method enabled the identification of a cruise condition that was both rapid and fuel-efficient.

C. Mission Segments and Time-step Integration

Tables 13, 14, 15, and 16 present the time-step integration results obtained using the aforementioned methodology. These tables provide detailed data not just on fuel consumption, required thrust, drag, and distance covered but also on the L/D ratio, T/W ratio, throttle setting, and fuel flow ranges across various mission segments, serving as the basis for evaluating the aircraft's performance throughout the mission profile.

Table 13. DCA Patrol Mission – Basic Flight Data

Phase	Initial Weight [lb]	Fuel Consumed [lb]	Speed [kts]/Mach	Altitude [ft]	Time [s]	Range [nmi]	Throttle Setting (%)
1. Take-off GR	30,770	76	148/0.25	0	20	–	100(dry)
2. Take-off Transition	30,694	47	161/0.24	0-1,000	12.2	–	100(dry)
3. Take-off Climb(1,000 ft)	30,648	18	161/0.24	1,000	4.7	–	100(dry)
4. Climb to Cruise	30,630	500	586/0.9-1.02	1,000-35,000	160	25.4	100(dry)
5. Cruise Out	30,130	1,230	514/0.9	35,000	2,101	300	32.6-27.0(dry)
6. Loiter	28,900	7,580	470/0.82	35,000	14,400	–	25.7-41.5(dry)
7. Dash	21,320	1,290	1.60	35,000	390	100	35(wet)
8. Combat 1	20,010	430	1.20	35,000	47	–	100(wet)
9. Combat 2	19,580	320	0.90	35,000	47	–	100(wet)
10. Climb to Cruise	18,600	185	565/0.98	35,000-51,000	153	23.8	100(dry)
11. Cruise Back	18,415	1,515	630/1.10	51,000	2,286	400	70.2-56.0(dry)
12. Reserves	–	1,000	–	–	–	–	–

Phase	Thrust Range [lbf]	Drag Range [lbf]	L/D Ratio Range	T/W Range	Fuel Flow Range [lb/s]	γ [deg]	ROC [FPM]
1. Take-off GR	16,384-17,079	0-7,836	0-7.9	0.52-0.54	3.90	–	–
2. Take-off Transition	16,142-16,369	5,618-5,687	7.9-8.1	0.51-0.52	3.76	–	–
3. Take-off Climb(1,000 ft)	15,972-16,139	5,688-5,745	7.7-7.9	0.51	3.73	18.9-19.3	–
4. Climb to Cruise	6,774-16,153	2,855-4,021	7.9-10.9	0.21-0.51	1.90-4.90	7.9-10.9	7,459-15,365
5. Cruise Out	Matched to Drag	2,384-2,499	12.4-12.5	0.08	0.57-0.6	–	–
6. Loiter	Matched to Drag	2,026-2,897	10.7-11.1	–	0.41-0.68	–	–
7. Dash	Matched to Drag	9,552-9,584	2.2-2.3	0.43-0.46	3.30-3.36	–	–
8. Combat 1	Matched to Drag	15,639	n = 5.0	Turn Rate = 7.67	–	–	–
9. Combat 2	Matched to Drag	12,080	n = 3.8	Turn Rate = 7.77	–	–	–
10. Climb to Cruise	3,126-6,653	2,043-2,220	9.1-9.8	0.16-0.33	0.90-1.90	2.9-12.7	2,879-12,565
11. Cruise Back	Matched to Drag	2,316-2,469	8-8.1	0.12-0.13	0.64-0.69	–	–

Table 14. Point Defense Intercept Mission – Basic Flight Data

Phase	Initial Weight [lb]	Fuel Consumed [lb]	Speed [kts]/Mach	Altitude [ft]	Time [s]	Range [nmi]	Throttle Setting (%)
1. Take-off GR	22,452	40	125	0	11	–	100(dry)
2. Take-off Transition	22,412	67	136	0-1,000 ft	18	–	100(dry)
3. Take-off Climb(1,000 ft)	22,345	0	0	0	0	0	0
4. Climb to Dash	24,155	440	638	1,000-35,000	130	22	100(dry)
5. Dash	23,715	3,921	2	35,000	625	200	70(wet)
6. Combat 1	19,795	367	1.2	35,000	40	–	100(wet)
7. Combat 2	19,425	273	0.9	35,000	40	–	100(wet)
8. Climb to Cruise	18,155	202	566	35,000-55,000	202	29	100(dry)
9. Cruise Back	17,995	700	630	55,000	1143	200	60.2-46.0(dry)
10. Reserves	–	1000	–	–	–	–	–

Phase	Thrust Range [lbf]	Drag Range [lbf]	L/D Ratio Range	T/W Range	Fuel Flow Range [lb/s]	γ [deg]	ROC [FPM]
1. Take-off GR	16,426-17,079	0-5,553	0-7.4	0.73-0.76	3.82	–	–
2. Take-off Transition	15,938-16,401	3,984-4,083	7.7-8.1	0.71-0.73	3.71	–	–
3. Take-off Climb(1,000 ft)	0	0	0	0	0	0	–
4. Climb to Dash	7,014-16,208	3,027-4,886	4.6-7.2	0.32-0.73	2.10-5.10	10.5-15	11,567-16,449
5. Dash	Matched to Drag	12,830-12,878	1.4-1.7	0.59-0.71	6.30	–	–
6. Combat 1	Matched to Drag	15,639	n = 5.77	Turn Rate = 8.9 deg/s	–	–	–
7. Combat 2	Matched to Drag	12,080	n = 4.41	Turn Rate = 9 deg/s	–	–	–
8. Climb to Cruise	2,577-6,653	1,766-2,057	8.4-9.8	0.15-0.38	0.74-1.91	2.4-15	2,442-14,822
9. Cruise Back	Matched to Drag	2,050-2,121	8.0-8.1	0.12	0.57-0.59	–	–

Table 15. Intercept/Escort Mission Optimized – Basic Flight Data

Phase	Initial Weight [lb]	Fuel Consumed [lb]	Speed [kts]/Mach	Altitude [ft]	Time [s]	Range [nmi]
1. Take-off GR	30,770	76	148/0.25	0	20	–
2. Take-off Transition	30,694	47	161/0.24	0-1,000	12	–
3. Take-off Climb(1,000 ft)	30,648	18	161.4/0.24	1,000	5	–
4. Climb to Dash	30,630	500	586/0.90-1.02	1,000-35,000	160	25
5. Dash	30,130	8,054	1.60	35,000	2,342	600
6. Escort	22,076	2,114	300/0.52	35,000	3,600	300
7. Climb to Cruise	19,962	0	0	35,000	0	0
8. Cruise Back	19,962	2,383	500/0.87	35,000	6,480	900
9. Reserves	–	1,000	–	–	–	–

Phase	Thrust Range [lbf]	Drag Range [lbf]	L/D Ratio Range	T/W Range	Fuel Flow Range [lb/s]	γ [deg]	ROC [FPM]
1. Take-off GR	16,384-17,079	0-7,836	0-8.0	0.52-0.54	3.90	–	–
2. Take-off Transition	16,142-16,369	5,618-5,687	7.9-8.1	0.51-0.52	3.80	–	–
3. Take-off Climb(1,000 ft)	15,972-16,139	5,688-5,745	7.7-7.9	0.50-0.51	3.70	18.90-19.30	–
4. Climb to Dash	6,774-16,153	2,855-4,021	7.9-10.9	0.22-0.52	1.96-4.90	7.85-10.90	7,459-15,365
5. Dash	Matched to Drag	9,604-9,853	2.4-3.2	0.32-0.42	3.37-3.50	–	–
6. Escort	Matched to Drag	2,772-3,275	7.0-7.5	0.13-0.14	0.51-0.68	–	–
7. Climb to Cruise	0	0	0	0	0	0	0
8. Cruise Back	Matched to Drag	1,704-1,886	10.8-11.0	0.09	0.34-0.40	–	–

Table 16. Intercept/Escort Mission High Dash – Basic Flight Data

Phase	Initial Weight [lb]	Fuel Consumed [lb]	Speed [kts]/Mach	Altitude [ft]	Time [s]	Range [nmi]
1. Take-off GR	30,770	76	148/0.25	0	20	–
2. Take-off Transition	30,694	47	161/0.24	0-1,000	12	–
3. Take-off Climb(1,000 ft)	30,648	18	161/0.24	1,000	5	–
4. Climb to Dash	30,630	500	586/0.90-1.02	1,000-35,000	160	25.4
5. Dash	30,130	7,655	2	35,000	1,561	350
6. Escort	22,475	2,400	300/0.52	35,000	3,600	300
7. Climb to Cruise	20,235	188	566/0.98	35,000-50,000	148	23.1
8. Cruise Back	20,047	2,500	625/1.10	35,000	3,744	650
9. Reserves	–	1,000	-	-	-	-

Phase	Thrust Range [lbf]	Drag Range [lbf]	L/D Ratio Range	T/W Range	Fuel Flow Range [lb/s]	γ [deg]	ROC [FPM]
1. Take-off GR	16,384-17,079	0-7,836	0-8.0	0.52-0.54	3.90	–	–
2. Take-off Transition	16,142-16,369	5,618-5,687	7.9-8.1	0.51-0.52	3.76	–	–
3. Take-off Climb(1,000 ft)	15,972-16,139	5,688-5,745	7.7-7.9	0.50-0.51	3.73	18.9-19.3	–
4. Climb to Dash	6,774-16,153	2,855-4,021	7.9-10.9	0.22-0.51	1.96-4.92	7.90-10.9	7,459-15,365
5. Dash	Matched to Drag	13,915-14,068	1.7-2.2	0.45-0.59	6.96-7.10	–	–
6. Escort	Matched to Drag	2,840-3,375	6.9-7.5	0.13-0.14	0.53-0.71	–	–
7. Climb to Cruise	3,280-6,653	2,139-2,283	9.3-9.9	0.16-0.31	0.95-1.91	2.90-11.9	2,885-11,804
8. Cruise Back	Matched to Drag	2,292-2,543	8.1-8.3	0.12-0.12	0.64-0.70	–	–

The data presented are complete and comprehensive, capturing flight performance throughout each phase of the three missions outlined in the RFP [1]. Parameters such as L/D ratios, T/W ratios, fuel flow rates, and other critical metrics were continuously tracked to ensure accuracy and to validate results across the various disciplines contributing to the integration of this design proposal, helping the team assert its fidelity with confidence.

For engine warm-up, an estimated fuel allocation of 2% of the total fuel weight was reserved, following guidance from Roskam [20]. Regarding reserve fuel, several methods were explored. Although the RFP [1] specified a 30-minute loiter reserve at sea level, even at an optimized sea-level loiter speed, this would result in fuel consumption of approximately 3,000 lbs, which is an unreasonably high value for a reserve, given our current fuel allocations for each phase.

After conducting further research and internal consultation, a more practical approach was adopted: 30 minutes of loiter at 35,000 ft was deemed representative, as it allows for the reproduction of reserve endurance at reduced speeds and lower altitudes, equivalent to 25 min of loiter at 15,000 ft. This led to a reserve fuel estimate of 947 lb, which was conservatively rounded up to an even 1,000 lb to include a safety margin.

1. DCA Patrol Mission

This mission proved to be the most constraining, necessitating multiple design iterations to ensure that the aircraft could accommodate sufficient fuel volume to meet the mission requirements. As shown in Table 13, fuel consumption was highest during the loiter phase, making its reduction a major objective. To achieve this, fuel flow and thrust data were extrapolated beyond the initial GasTurb 14 outputs, allowing for a more precise match to the loiter drag profile and enabling further minimization of fuel consumption.

It is also noteworthy that the dash segment for this mission was executed at Mach 1.6 rather than the aircraft's maximum dash capability of Mach 2.0. This decision was made to demonstrate the feasibility of completing the mission within the available fuel limits, thereby satisfying the RFP's minimum dash requirement [1]. However, for the remaining mission profiles, data are presented assuming the full Mach 2 dash capability of the aircraft.

Additionally, optimal cruise speeds and altitudes vary between the outbound and return segments due to the aircraft's changing weight. This weight-sensitive optimization was implemented to extract and represent the maximum performance potential of the design across all mission phases. Table 17 summarizes the main performance values of the DCA patrol mission.

Table 17. DCA Patrol Mission Summary

Parameter	Value
Warm Up Fuel	265 lb
Reserve Fuel	1,000 lb
Max Dash	Mach 1.6
Optimal Cruise Altitude	35,000 & 51,000 ft
Optimal Cruise Speeds	Mach 0.9 & Mach 1.1
Total Fuel Consumed	14,478 lb
Total Time Taken	5.4 hrs

2. PDI Mission

This mission was comparatively less constraining. The performance results in Table 14 highlight the aircraft's capability to sustain high dash speeds and demonstrate super-cruise functionality, coupled with exceptionally high sustained turn rates, traits that are consistent with the intended role of a homeland interceptor. Table 18 summarizes the main performance values of the PDI mission.

Table 18. PDI Mission Summary

Parameter	Value
Warm Up Fuel	140 lb
Reserve Fuel	1,000 lb
Max Dash	Mach 2.0
Optimal Cruise Altitude	55,000 ft
Optimal Cruise Speeds	Mach 1.1
Total Fuel Consumed	7,115 lb
Total Time Taken	0.613 hr

Table 19. I/E Mission Summary

Parameter	Value
Warm Up Fuel	265 lb
Reserve Fuel	1,000 lb
Max Dash	Mach 2.0 / Mach 1.6
Optimal Cruise Altitude	35,000 ft
Optimal Cruise Speeds	Mach 1.1 / Mach 0.9
Total Fuel Consumed	14,470 lb
Total Time Taken	2.57 / 3.505 hr
Dash Radius	350 / 600 nmi

3. I/E Mission

This mission was designed to demonstrate the aircraft's maximum dash radius. While the RFP mandated a minimum dash radius of 200 nmi [1], the aircraft achieved a radius of a remarkable 350 nmi at a dash speed of Mach 2.0. Furthermore, at the minimum required dash speed of Mach 1.6, the mission yielded a radius close to 600 nmi, nearly three times the requirement.

To showcase mission versatility, the escort segment was flown at a representative speed of 300 knots. This value was selected as the minimum practical escort speed, accommodating the wide range of aircraft types that may be escorted or encountered during actual operational scenarios. The chosen speed also ensures safe and stable level flight, considering stall margin and dynamic stability at lower speeds. Table 19 summarizes the main performance values of the I/E mission.

D. Analysis for Performance Requirements and Constraints

1. RFP Performance Minimas

At 50% internal fuel, the following results were observed to determine whether the RFP minimum performance requirements are met as shown in Table 20.

Table 20. Performance at Maneuver Weight (50% Internal Fuel)

Requirement	Homelander's Performance
Maximum Mach Number at 35,000 ft	
Mach 1.6	Mach 2.0
1-g Specific Excess Power – Military Thrust	
0.9M / Sea Level: 200 ft/s 0.9M / 15,000 ft: 50 ft/s	496 ft/s 358 ft/s
1-g Specific Excess Power – Maximum Thrust	
0.9M / Sea Level: 700 ft/s 0.9M / 15,000 ft: 400 ft/s	1377 ft/s 885 ft/s
5-g Specific Excess Power – Maximum Thrust	
0.9M / Sea Level: 300 ft/s 0.9M / 15,000 ft: 50 ft/s	1028 ft/s 367 ft/s
Sustained Load Factor – Maximum Thrust (0.9M / 15,000 ft)	
5.0 gs	6.81
Maximum Instantaneous Turn Rate at 35,000 ft	
18.0 deg/s	18.04 deg/s at Mach 0.88
Climb to 35,000 ft from SL at a distance of 4.8 nmi	
Under 1 minute	45 s

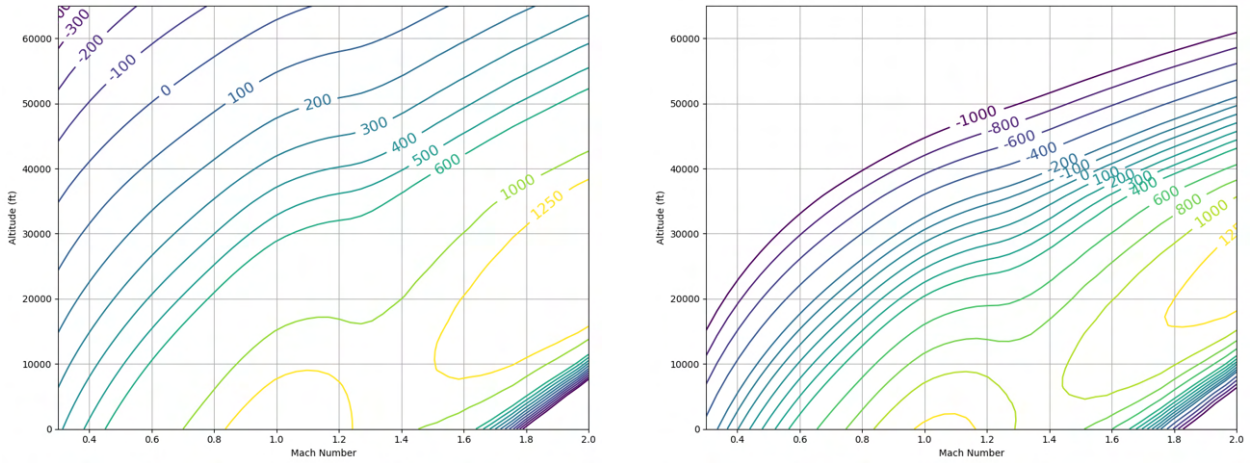

(a) Max Thrust (1-g) **(b) Max Thrust (5-g)**

Fig. 41 Maximum thrust specific excess power envelopes.

Figures 41a and 41b plot the maximum thrust-specific excess power envelopes. The figures illustrate that the aircraft retains significant excess power even above 60,000 ft, indicating the potential for further ascent and higher speeds within the atmosphere in 1g load conditions. These plots play a significant in depicting operable envelopes for combat maneuvers and high turn rates, or high g pull-up.

2. Flight Envelope

Due to the substantial available thrust under afterburner operation, it proved challenging to define definitive mathematical bounds for absolute and service ceilings. Given this, and being satisfied with the observed performance characteristics within the dry thrust flight envelope, the team elected not to explore flight beyond 62,000 ft. This decision was further supported by limitations in the atmospheric modeling approach. The team's calculations were based on the 1962 US Standard atmospheric model, whose model changes at extreme altitudes. Therefore, the performance assessments were constrained to altitudes within a regime where the model remains valid and reliable. Additionally, while afterburner capability allows the aircraft to exceed the target dash speed of Mach 2.0, the team chose to limit this speed to avoid exposing the airframe to significant aerodynamic heating risks. The resulting flight envelope presented in Fig. 42 reflects a conservative, yet robust, constraint-driven, design—balancing performance potential with operational and structural considerations.

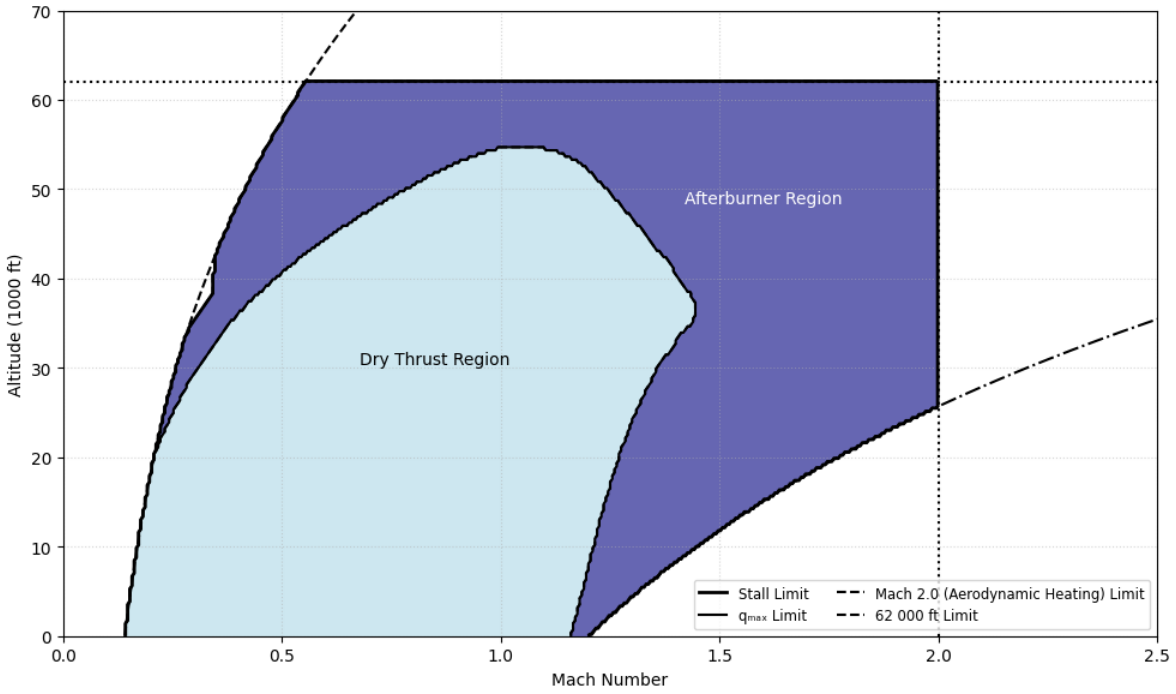

Fig. 42 Flight envelope at maneuvering weight.

As illustrated in the flight envelope diagram, the light blue region represents the operational boundaries under dry thrust conditions, while the darker shaded region indicates the extended envelope enabled by using afterburners. This distinction highlights the aircraft's enhanced operability and feasibility in high-performance regimes when utilizing afterburner power.

Figure 43 presents the maximum sustainable load factor flight envelope, illustrating the maneuvering limits across the aircraft's operational Mach and altitude range.

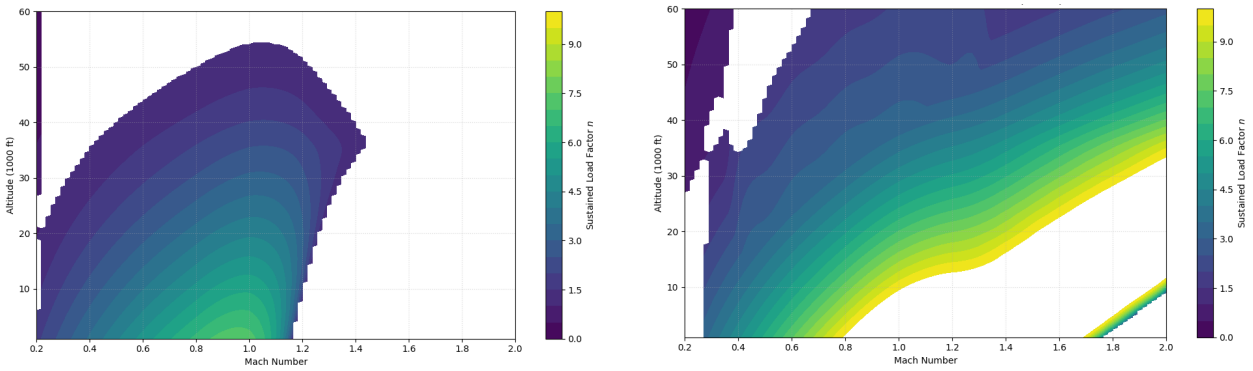

(a) Dry Thrust **(b) Afterburner Thrust**

Fig. 43 Max sustainable load factor flight envelope for dry and wet thrust.

E. Turn Performance Analysis

Figures 44 and 45 are critical to understanding the turn performance requirements and their associated constraints. Shown here is a representative turn performance plot that illustrates the relationship between turn radius, turn rate, load factor, Mach number, and the corresponding altitude at which convergence is achieved. Among the evaluated constraints, the most stringent was satisfying the required instantaneous turn rate of 18 deg/s. This plot effectively demonstrates how the design meets and fulfills this requirement.

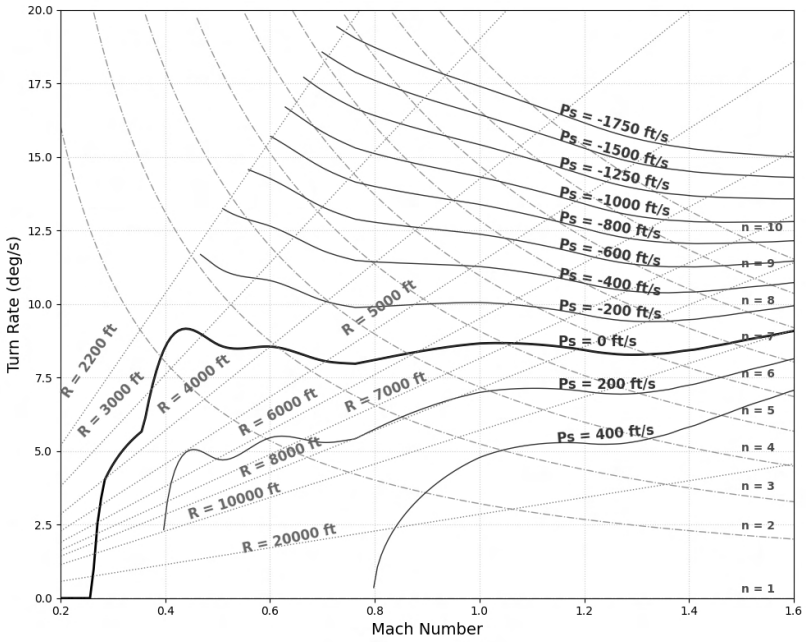

Fig. 44 Turn performance plot at 30,000 ft.

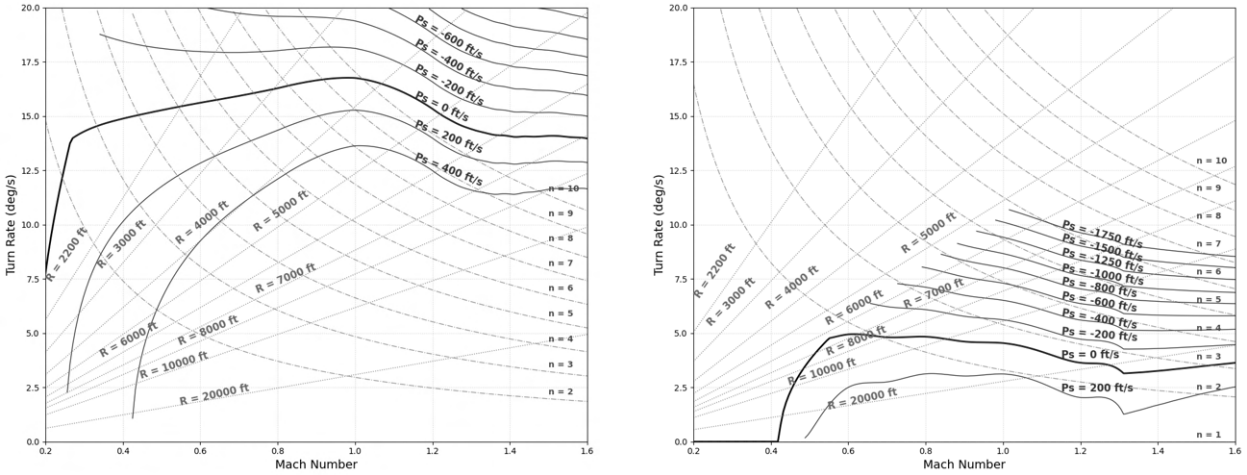

(a) At 10,000 ft **(b) At 50,000 ft**

Fig. 45 Turn performance plots at maneuvering weight for altitudes of 10,000 ft and 50,000 ft.

The Homelander achieves a turn rate of 18.04 deg at $C_{\text{Lmax}} = 2.52$ and a load factor of 8.0 gs, performed at a high AoA with slats deployed as seen in the Aerodynamics Section VI. The above plots also validate the sustained turn rates during the performed mission analysis and the g forces experienced and recorded during those maneuvers. These performance characteristics satisfy the requirements outlined in MIL-HDBK-516C Section 6.1.1 which defines standards for flight performance such as flight speed, climb, turn performance, and flight envelope validation.

IX. Mass Properties

Accurate weight and center of gravity approximations are key to other disciplines, such as Performance and Stability & Control. The Homelander's weight was calculated using a combination of Siemens NX CAD models, empirical equations from Nicolai and Raymer [6, 9], and various sources for known components. A summary of weights and other weight-related parameters can be seen in Table 21.

Table 21. Weight Summary

Parameter	Value
GTOW - DCA Patrol [lb]	31,034
Empty Weight [lb]	15,890
Fuel Weight [lb]	14,490
Payload Weight – PDI & I/E [lb]	654
Wing Loading [lb/ft^2]	76.10
Thrust–To–Weight	1.27
Fuel Fraction [%]	46

A. Component Weight and Center of Gravity Methods

The preferred method for estimating Homelander's component weights was direct measurement from CAD models, rather than relying solely on empirical equations like those in Nicolai's Chapter 20. Key structures including the wing, vertical and horizontal tails, fuselage, radome, and fuel were modeled in Siemens NX (see Fig. 62), allowing assignment of materials and calculation of weights based on volume and density. For components without CAD models, weights were estimated using empirical equations from Nicolai [9] and Raymer [6], covering items such as the landing gear, fuel system, engine controls, control surfaces, avionics, electrical, hydraulic, and anti-icing systems.

Certain weights were also sourced directly: ordnance and radar from the RFP as GFE [1], engine weight from the F100-PW-229 Product Card [21], jet fuel starter from NATO proceedings [22], and launch systems from manufacturer product cards [23, 24]. The components listed as "Fuel Tanks" include the maximum fuel capacities of the tanks. This

component includes the weight of only fuel, while the "Fuel System" component includes the weight of tanks, pumps, and other fuel system related components. Note all component locations and CGs were determined from the Siemens NX CAD model using the Analysis - Measure tool, with reference to the aircraft nose. Table 22 summarizes the weights and locations of all components.

Table 22. Component Weights, Locations, and Data Sources

Component	Weight [lbs]	Location [in. from nose]	Source
Fuselage Tank A	5,080	333	CAD
Fuselage Tank B	4,280	237	CAD
Fuselage Tank C	720	390	CAD
Fuselage Tank D	190	210	CAD
Fuselage Tank E	250	380	CAD
Engine Section Tank	180	515	CAD
Wing Tank	630	380	CAD
Conformal Tanks	2,010	420	CAD
External Wing Tanks	1,150	430	CAD
Radome	135	50	CAD
Wing	1,980	360	CAD
Vertical Tail	283	520	CAD
Horizontal Tail	513	565	CAD
Fuselage	3,603	390	CAD
Engine	3,826	540	Manufacturer Data
Jet Fuel Starter	56	520	Manufacturer Data
Missile Eject Launcher (2)	154	275	Manufacturer Data
AIM-120 (2)	654	275	RFP
Radar	450	100	RFP
Landing Gear	1,140	280	Nicolai
Fuel System	790	210	Nicolai
Engine Controls	25	240	Nicolai
Control Surface System	790	360	Raymer
Avionics (installed)	1,375	130	Raymer
Electrical System	390	390	Raymer
Hydraulic System	225	390	Raymer
Anti-Icing System	155	310	Raymer
Total Weight (MTOW)	31,034		

B. CG Build-Up

A component build-up CG plot was also generated, as seen in Fig. 46. It has the parameters seen in Table 23. This visual is useful in visualizing how the aircraft's center of gravity shifts as components are added, as well as the influence that certain components have on the overall CG.

Table 23. Component Build-Up Information

Step	Configuration	Weight [lbs]	CG (%MAC)
1	Wing	1,980	41.8
2	Wing + Fuselage	5,583	54.2
3	Wing + Fuselage + Tail	6,379	67.7
4	Wing + Fuselage + Engine	10,261	101.3
5	Wing + Fuselage + Engine + Operating Items	15,151	60.3
6	Wing + Fuselage + Engine + Operating Items + Ordnance	16,409	52.5
7	Wing + Fuselage + Engine + Operating Items + Ordnance + Fuel	31,034	37.9

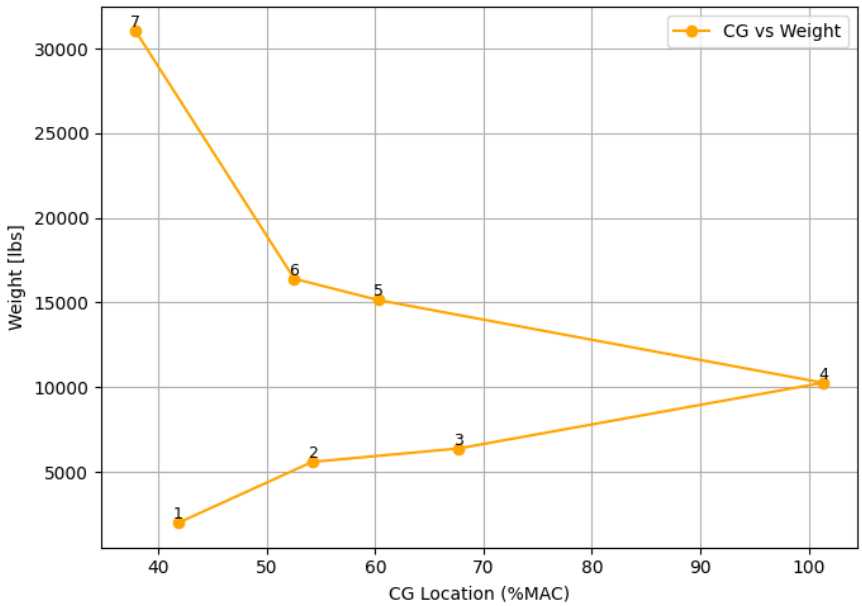

Fig. 46 Component build-up CG.

C. Aircraft Total Weight and Center of Gravity

The maximum-take-off (MTOW) and empty weights (EW) of the aircraft are listed in Table 24. The MTOW includes maximum fuel, including external conformal and wingtip tanks. The EW includes no fuel or ordnance. Their respective CG locations are also listed.

Table 24. Aircraft Weights and CG Locations

Condition	Weight [lb]	CG [in]	CG [%MAC]
MTOW	31,034	353.1	37.9
Empty Weight	15,890	376.7	52.5

D. Absolute CG Envelope

The aircraft's absolute CG envelope was found by loading and unloading in a single direction. The loading process took the following order: Fuselage Tank D, Fuselage Tank B, Ordnance, Fuselage Tank A, Fuselage Tank E, Wing Tanks, Fuselage Tank C, Conformal Tanks, External Wing Tanks, and Engine Section Tank. The unloading process took the same order. This provided the aircraft's CG envelope which can be experienced during the loading/unloading process on the ground. This CG range assessment meets MIL-HDBK-516C Section 6.4.2, which defines requirements for center of gravity tracking and loading/unloading margin envelope. These CG limits are important, specifically to landing gear sizing. The fore limit occurs with the following loaded: Fuselage Tank D, Fuselage Tank B, Ordnance, Fuselage Tank A, and Fuselage Tank E. The aft limit occurs with the following loaded: Engine Section Tank, External Tank, Conformal Tank, and Fuselage Tank C. Figure 47 depicts this process and the values for each step can be seen in Table 25.

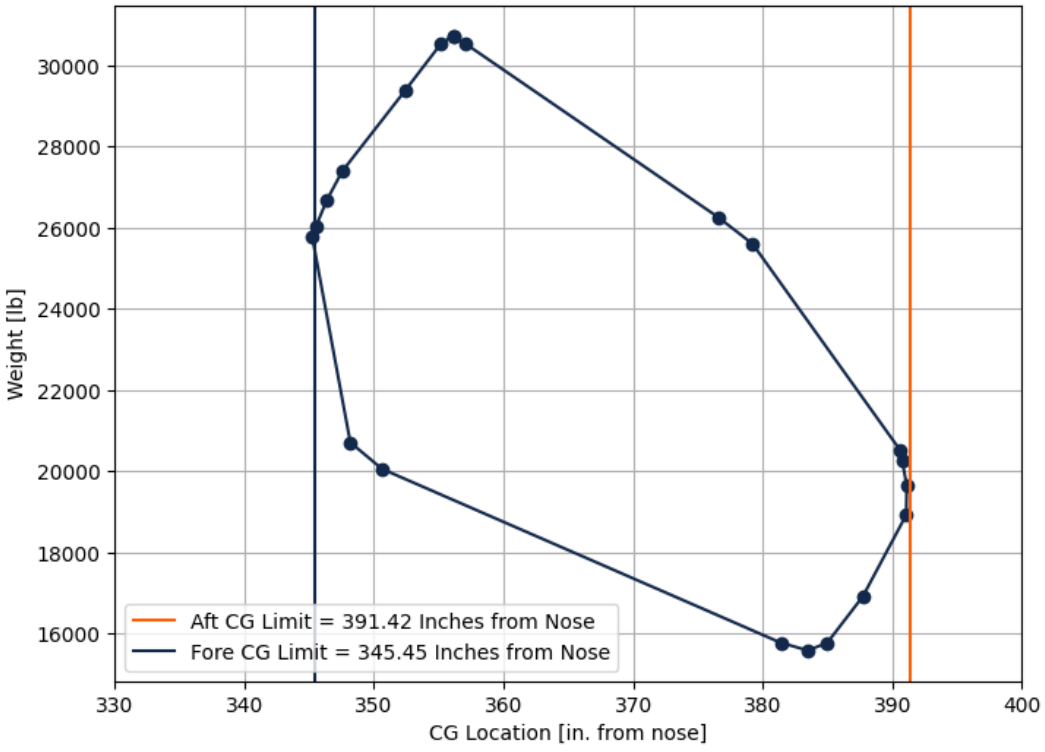

Fig. 47 Extreme fore and aft CG limits during loading and unloading.

Table 25. Ultimate Loading/Unloading Fore and Aft CG Limits

Condition	Weight [lbs]	CG [in]
Fore Limit	25,792	345.45
Aft Limit	19,645	391.42

E. Mission Shift Minimization

The complexity of the aircraft fuel tank system has a significant impact on the CG shift of the aircraft throughout flight, and therefore the static margin (SM) changes throughout flight. To quantify the effects of a more complex fuel system, simulations were conducted on fuel tank depletion throughout the DCA patrol mission with two conditions: tank depletion without the use of a reservoir tank system and tank depletion with the use of a reservoir tank system.

Tank depletion with the use of a reservoir tank system was simulated by depleting these larger tanks in segments: Fuselage Tank A (2 segments) and Fuselage Tank B (3 segments). Mission fuel depletion simulations included depleting these tanks in more segments to have more possible orders of depletion, and therefore further minimize the shift in CG throughout the mission.

The approach involved calculating the center of gravity for every segment of each mission with every possible combination of fuel tank depletion. This was implemented in Python code. The function found the fore and aft SM limits during the mission, calculated the difference between the two, and found the order of depletion that resulted in the smallest range of SM values. The CG and SM plots for the DCA patrol can be seen in Figs. 48 and 49. The limit CG and SM values experienced can be seen in Table 26. This system was deemed necessary to meet the RFP's requirement of subsonic static margin limit values with the Homelander's configuration, as values without tank segments do not meet the requirement [1].

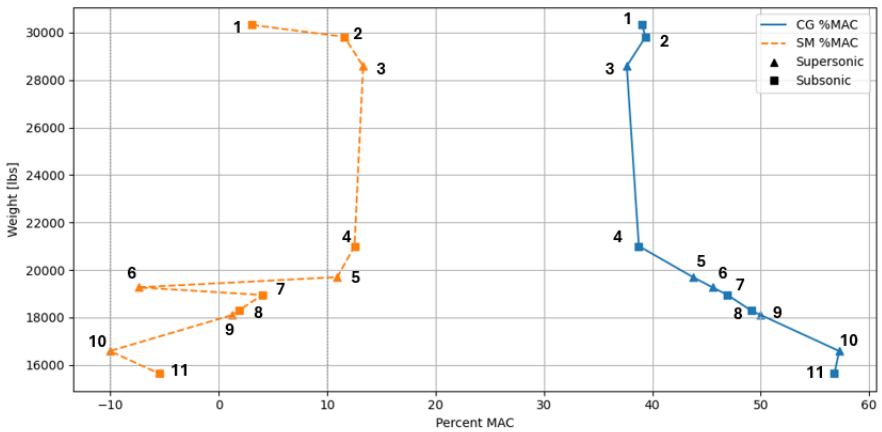

Fig. 48 DCA patrol mission CG and SM range without tank segments.

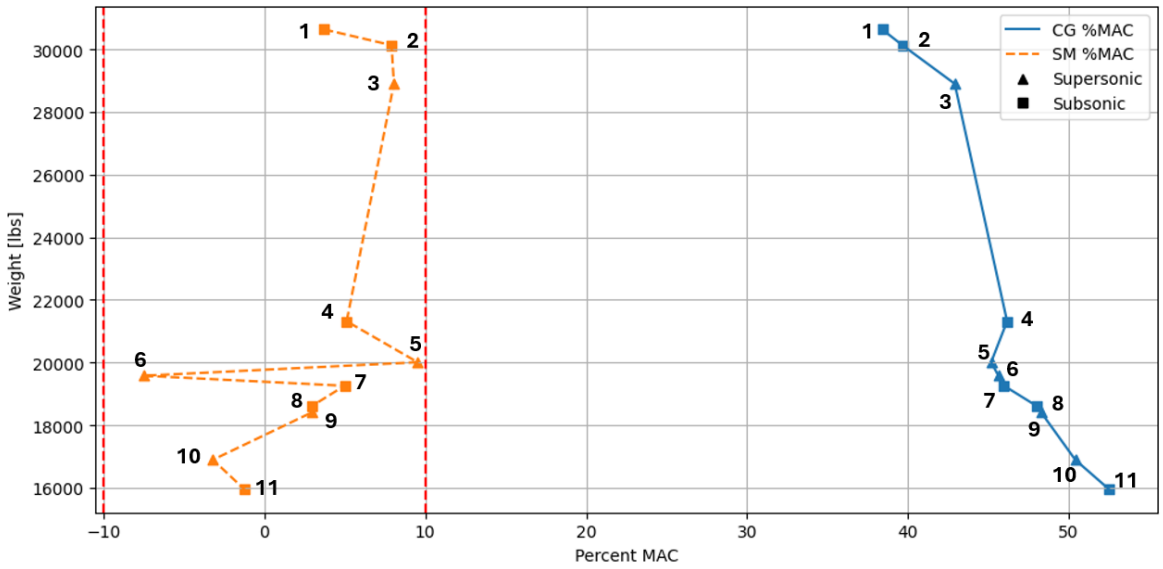

Fig. 49 DCA patrol mission CG and SM range with tank segments.

Table 26. CG and Static-Margin Limits (%MAC)

Limit	No-Tank Segments	Tank Segments
Fore CG Limit	39.0	38.4
Aft CG Limit	57.2	52.5
Fore SM Limit	−10.0	7.5
Aft SM Limit	13.3	9.5

F. Mission CG Envelopes

The aircraft's weight and CG was plotted at each segment of each mission, as defined in the Performance Section VIII. The mission static margin shift minimization method was used. The values are listed in Tables 27 - 29. Figures 50 and 51 show how the CG of the aircraft shifts throughout the mission due to fuel expenditure and ordnance drop. This was done by using the fuel expenditure data as described in the Performance Section VIII.

Table 27. DCA Patrol Mission Segment Weights, CG, and SM

	Segment	Weight [lbs]	CG [%MAC]	SM [%MAC]
1	WUTTO	30,630	38.4	3.7
2	Climb	30,130	39.7	7.9
3	Cruise	28,900	42.9	8.1
4	Loiter	21,320	46.2	5.1
5	Dash	20,010	45.2	9.5
6	CA1	19,580	45.6	-7.5
7	CA2	19,260	46.0	5.0
8	Ordnance Drop	18,600	48.0	2.9
9	Climb	18,415	48.3	3.0
10	Cruise	16,900	50.4	-3.2
11	Reserve	15,950	52.5	-1.2

Table 28. PDI Mission Segment Weights, CG, and SM

	Segment	Weight [lbs]	CG [%MAC]	SM [%MAC]
1	WUTTO	24,155	43.3	-1.2
2	Climb	23,715	44.1	3.4
3	Dash	19,795	48.0	14.2
4	CA1	19,425	48.5	-10.5
5	CA2	19,190	48.8	2.2
6	Ordnance Drop	18,155	52.3	-1.3
7	Climb	17,955	52.6	-7.4
8	Cruise	17,295	52.4	-5.2
9	Reserve	16,295	52.6	-1.3

Table 29. I/E Mission Segment Weights, CG, and SM

	Segment	Weight [lb]	CG [%MAC]	SM [%MAC]
1	WUTTO	30,630	38.4	3.7
2	Climb	30,130	39.7	7.9
3	Dash	22,070	44.8	9.9
4	Escort	19,960	45.6	-2.0
5	Cruise	17,575	48.5	4.4
6	Reserve	16,575	49.9	1.4

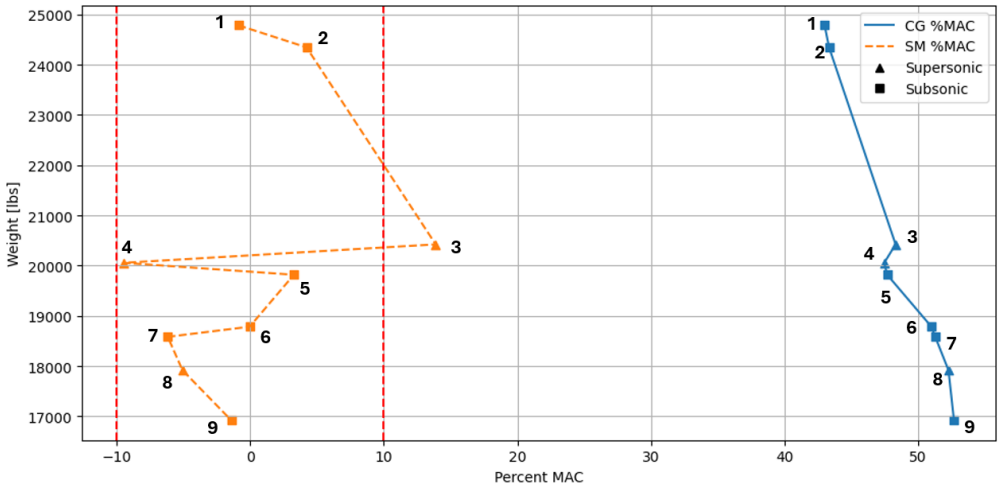

Fig. 50 PDI Mission CG and SM plot.

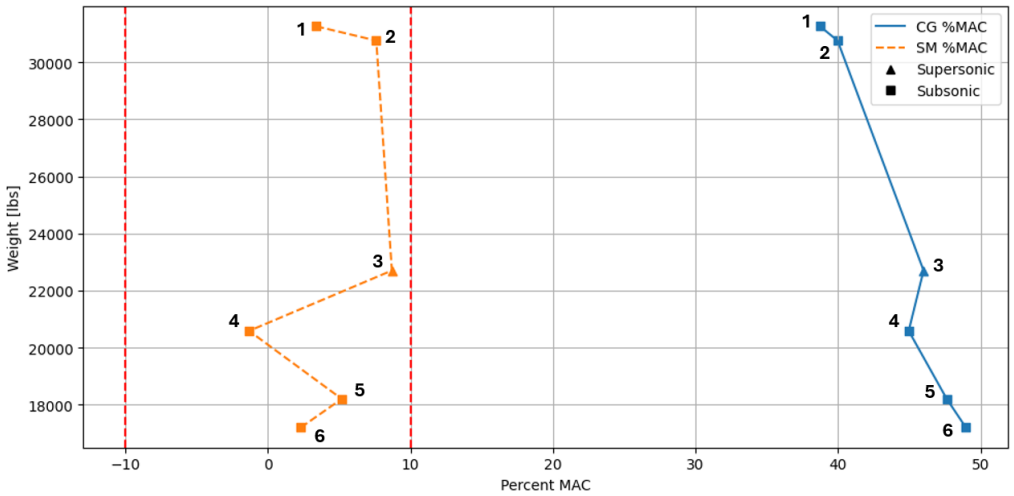

Fig. 51 I/E Mission CG and SM range.

The CG and SM limits are listed in Table 30. The significance of the static margin values will be discussed in the Stability & Control Section X.

Table 30. CG and Static Margin Limits Across Missions

Parameter	**DCA Mission**	**PDI Mission**	**I/E Mission**
Max Fore CG [%MAC]	38.4%	43.3%	38.4%
Max Aft CG [%MAC]	52.5%	52.6%	49.9%
Total Static Margin Range [%MAC]	-7.5% – 9.5%	-10.5% – 14.2%	-2.0% – 9.9%
Subsonic Static Margin Range [%MAC]	**-1.2% – 7.9%**	**-7.4% – -3.4%**	**-2.0% – 7.9%**

X. Stability & Control

The Homelander's stability and control characteristics were evaluated using analytical methods for both subsonic and supersonic regimes, as well as subsonic aerodynamic computational models with Athena Vortex Lattice (AVL) [25]. This analysis encompassed empennage and control surface design, assessments of longitudinal and lateral stability, as well as evaluations of static and dynamic flight qualities, all while ensuring compliance with MIL-STD-1797 and RFP requirements [1].

The stability and control assessment was conducted across five critical flight phases of the DCA patrol mission, which represents the most constraining operational profile due to its use of external fuel tanks inducing significant CG shifts. Table 31 details these phases and their associated mission characteristics. For the loiter, cruise, and dash phases, the weight was assumed to be maneuver weight as defined by the RFP [1], and the CG location was the mean of the max fore and aft. For the landing condition, an emergency landing scenario was considered. Thus, the weight and CG location were the same as take-off.

Table 31. Stability & Control Flight Phase Characteristics

	Take-off	**Landing**	**Loiter**	**Cruise**	**Dash**
Altitude [kft]	0	0	35	45	35
Mach Number	0.25	0.17	0.80	1.10	1.60
Weight [lb]	31,034	31,034	23,000	23,000	23,000
CG Location [Fore/Mean]	Max Fore CG	Max Fore CG	Mean CG	Mean CG	Mean CG
Flaps Deployed [Y/N]	Y	Y	N	N	N

A. Tail Configuration

1. Horizontal Stabilizer

The horizontal stabilizer design of this aircraft was primarily influenced by longitudinal stability analysis through many design iterations. Preliminary designs excluded a horizontal stabilizer, but one was added to satisfy the final design's derived requirements for longitudinal stability and trim conditions such as a negative C_{M_α} and positive C_{M_0}. A tail configuration was selected over a canard to avoid disrupting the wing's freestream airflow and to minimize shock interactions at supersonic speeds. The tail was designed to be all-moving to allow for variable incidence angles. This design choice provides consistent control and prevents control reversal at the high Mach numbers for which the Homelander is designed.

A hexagonal airfoil with a 5.5% thickness-to-chord ratio was selected for the horizontal stabilizer due to its superior supersonic performance and structural benefits as mentioned in the Aerodynamics Section VI. Its symmetrical shape

provides balanced stability and control authority, while the sharp leading edge minimizes adverse effects such as shock waves associated with supersonic speeds. The airfoil is chosen to be thinner than the wing such that control effectiveness does not deteriorate regardless of the local Mach number seen by the tail compared to the wing.

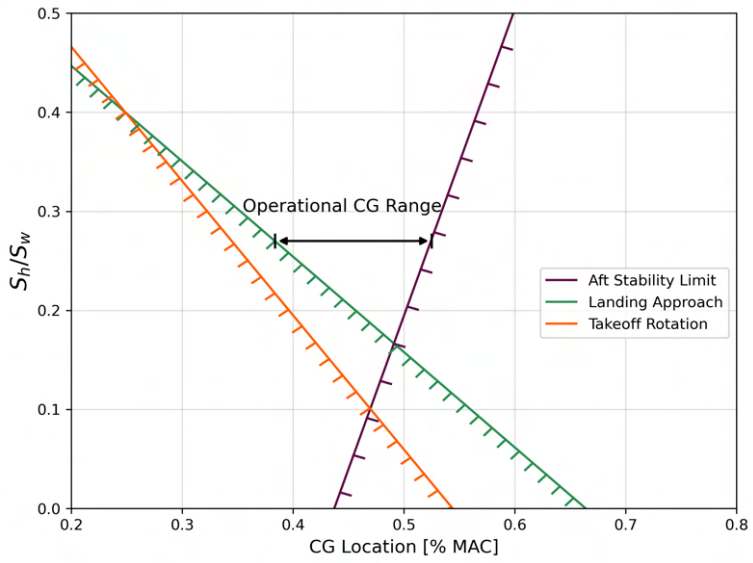

Fig. 52 Scissor plot used to determine optimal tail area ratio.

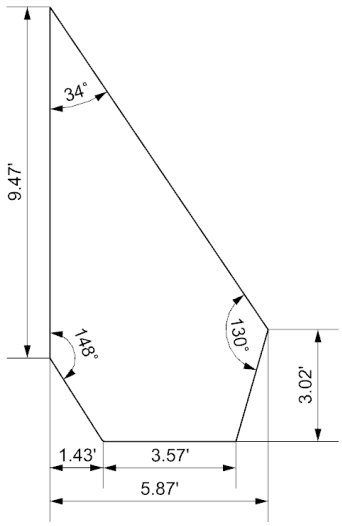

Fig. 53 Horizontal tail dimensional drawing.

The horizontal tail area was sized using a scissor plot analysis for the aircraft with conformal tanks installed. Figure 52 depicts this plot, showing the aerodynamic forward CG limits for both take-off rotation and landing approach conditions based on methodologies from Torenbeek [26]. Due to the aircraft's fly-by-wire system, the aft CG limit was established without a stability margin requirement. Analysis conducted within the operational CG limits outlined in the Mass Properties Section IX yielded an optimal tail area ratio of 0.27. The dimensions of the horizontal tail are tabulated in Table 32 and a visual is provided in Fig. 53.

Table 32. Empennage Dimensions

	Horizontal Tail	**Vertical Tail**	**Dorsal Fin**
Area [ft^2]	80.66	38.47	10.90
Span	11.73	6.34	2.22
Root Chord [ft]	9.47	11.00	6.00
Tip Chord [ft]	3.02	1.14	-
Leading-edge Sweep [deg]	56	60	78
Tail Moment Arm [ft]	18.31	15.83	-
Volume Coefficient	0.38	0.07	-

2. Vertical Stabilizer

A single vertical stabilizer was selected due to its compatibility with a centrally-located single engine, simplifying the design. The aircraft's role as an interceptor also influenced the tail design decision. Although a twin vertical stabilizer configuration might offer better maneuverability, such features are not essential for the interceptor's main missions outlined in the RFP [1]. The chosen tail design, therefore, prioritizes speed and simplicity which aligns with the aircraft's intended role as defined by the RFP [1].

The vertical stabilizer was sized using a tail volume coefficient approach, with a coefficient of 0.074 selected for the Homelander based on precedent from comparable fighter designs. In addition to the vertical tail, a dorsal fin was added to the vertical stabilizer configuration. This choice was primarily to better optimize the area rule distribution of the aircraft as explained in the Aerodynamics Section VI. The dorsal fin also provides some stability benefits with a negligible effect on aircraft weight. At large angles of sideslip, the stabilizing yaw moment increases with the addition of the dorsal fin [27]. The dorsal fin is designed to have a straight, sharp leading edge to limit shock wave interaction. The size of the dorsal fin was initialized using an empirical statistical method created by Barua et al. [27] and optimized using area ruling. Both the vertical tail and dorsal fin have the same hexagonal airfoil with thickness-to-chord ratio of 0.055 as the horizontal tail. This design choice was made for the same reasons as explained above for the horizontal tail. The vertical stabilizer dimensions are tabulated in Table 32 and can be visualized in Fig. 54.

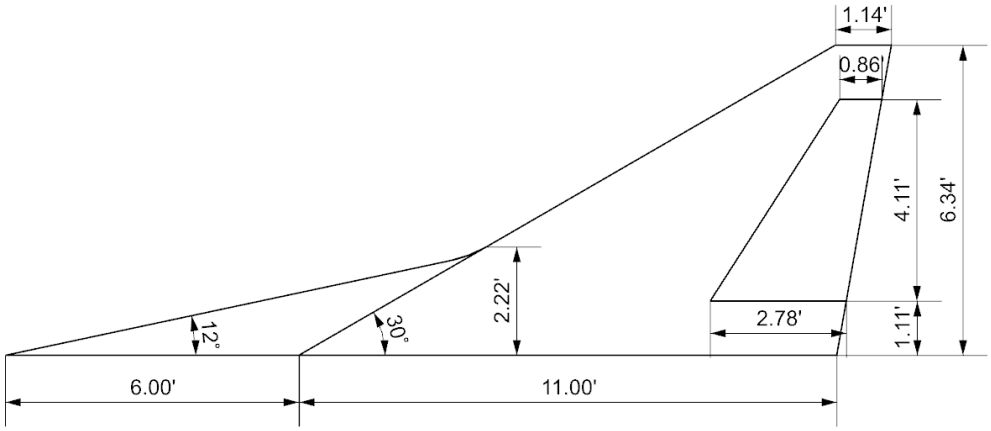

Fig. 54 Vertical tail, dorsal fin, and rudder dimensional drawing.

B. Control Surface Sizing

The three main control surfaces on the Homelander are the ailerons and flaps on the wing and the rudder on the vertical stabilizer. Since the horizontal tail is all-moving, it does not employ separate elevator surfaces. For the preliminary design of the ailerons, historical guidelines presented in Raymer Fig. 6.3 were used [6]. To ensure the size of the

ailerons met MIL-STD-1797 requirements for Class IVA aircraft (90 deg roll in 1.3 s), the roll rate was computed and compared to the required 1.21 rad/s. Initially, the ailerons were oversized, and the roll rate exceeded the requirement by a significant amount. A trade study was conducted to gauge the effects of reducing the chord or span ratios in order to minimize aileron surface area while still meeting the roll rate requirement. This study took the form of a 2^2 factorial design experiment, and it showed that for a given change in chord/span ratio the roll rate was impacted about 25% less by a change in chord ratio. Thus, to minimize the decrease in roll rate the chord ratio should be reduced to a greater extent than the span ratio.

The flaps were designed to occupy the remaining exposed wing area, maximizing lift coefficient enhancement during deployment. To streamline structural integration, the flaps and ailerons have identical hinge angles, which allows two significant advantages to the aircraft's design. First, this configuration enables a continuous wing spar to extend across the entire half-wingspan ahead of the control surfaces without structural complications. Second, the uniform hinge angle allows electro-hydraulic actuation systems to be installed along straight pathways parallel to the control surfaces, eliminating the need for complex bends or turns in the system lines. The aerodynamic benefits of this flap configuration are discussed in greater detail in the Aerodynamics Section VI.

Table 33. Control Surface Dimensions

	Aileron	**Flap**	**Rudder**
Root Chord Ratio	0.18	0.14	0.30
Tip Chord Ratio	0.14	0.18	0.30
Root Chord [ft]	1.30	1.99	2.78
Tip Chord [ft]	0.78	1.30	0.86
Span Ratio	0.30	0.40	0.65
Span [ft]	4.16	5.51	4.43
Area [ft^2]	4.31	9.05	7.48
Hinge Angle [deg]	21	21	40
Max Deflection [deg]	±30	40	±30

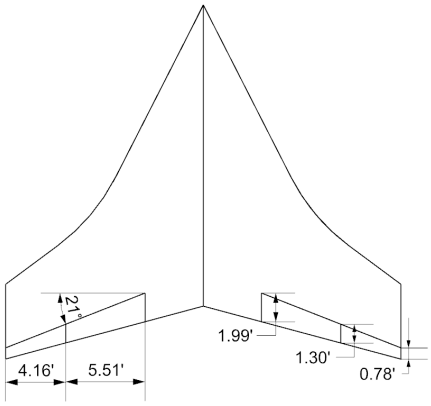

Fig. 55 Wing control surface dimensional drawing.

Similarly to the ailerons, the rudder size was initially made using suggestions from Raymer and finalized using requirements from MIL-STD-1797 [28]. Specifically, the rudder is to be effective in take-off and landing conditions of 90-deg crosswinds. This corresponds to rudder power that will allow the aircraft to hold a sideslip of 11.5 deg during take-off and landing conditions with a rudder deflection of ±20 deg as explained in Nicolai [9]. The rudder employs a constant chord ratio from root to tip chord and the span ratio is 65% which meets MIL-STD-1797 requirements with some margin. From these design decisions, the resulting control surface dimensions are tabulated in Table 33 and are visualized in Fig. 55.

C. Longitudinal Static Stability

The longitudinal static stability of the aircraft was characterized by its ability to achieve a negative C_{M_α}, positive C_{L_α}, and a ±10% subsonic static margin range required by the RFP [1]. The static margin analysis was performed using the aerodynamic center and stability derivative equations from Raymer [6], and the neutral point equation from McCormick [7]. Transonic and supersonic effects were taken into account for all calculations and smooth transitions were estimated using sigmoid-curve blending. Figure 56 plots the shift in neutral point as a function of Mach number, and the longitudinal stability derivatives evaluated at cruise, loiter, and dash are tabulated in Table 34 (units of rad^{-1}).

Table 34. Longitudinal Static Stability Coefficients

	C_{L_α}	C_{M_α}
Loiter	2.16	-0.27
Cruise	4.18	-0.35
Dash	3.47	-0.55

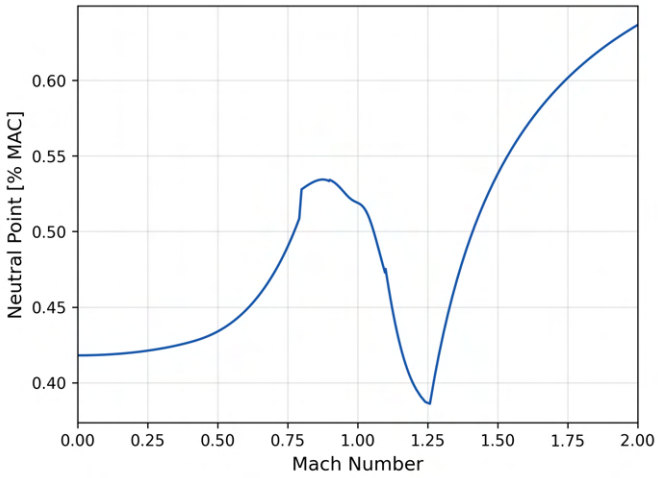

Fig. 56 Neutral point shift as a function of Mach number.

With the neutral point variation found, the static margin could be calculated throughout each mission. Table 30 in the Mass Properties Section IX includes these values for the aircraft during the DCA patrol mission, PDI, and I/E missions. As shown, the total static margin range accounts for supersonic mission segments, during which the neutral point shifts significantly aft and stability margins are reduced. This effect is more pronounced in the PDI mission, where the use of a Mach 2 dash segment results in a larger aft shift of the neutral point and, consequently, the widest total static margin range even though the CG shift itself is not the largest among the missions. This highlights the greater influence of high Mach number flight on static stability compared to CG movement alone. While the total static margin range exceeds the ±10% threshold in some cases, the subsonic static margin range remains within RFP requirements for all missions [1]. Although negative static margins occur at several points during flight, these instances of instability are managed by the digital flight control system described in the Systems Section XIV.

D. Aircraft Trim

Trim analysis was conducted for the Homelander at cruise, take-off, and landing conditions. To balance stability and structural feasibility, a trade study evaluated wing twist magnitude and distribution to achieve manageable horizontal tail deflections during cruise. The selected design incorporates linear wing washout, varying from 0 deg at the root to 3 deg at the tip. This configuration delays tip stall by reducing the wingtip's effective angle of attack relative to the root ensuring root stall precedes tip stall for retained aileron authority, while also increasing the zero-lift pitching moment coefficient (C_{M_0}).

At cruise, the horizontal stabilizer's downwash angle was calculated using Sadraey's methodology [29], combining zero-angle-of-attack downwash and downwash slope. The resulting downwash angle of 1.98 deg required a -1.47 deg horizontal tail deflection (leading-edge down) to achieve trim. AVL-based trim analysis for take-off and landing conditions revealed a -11.13 deg deflection requirement during take-off to generate the C_{Lmax} needed for rotation. Landing conditions, operating at lower airspeeds, required a -19.50 deg deflection at 20 deg angle of attack to maintain adequate C_{Lmax}. Figure 57 plots these critical points and the full range of horizontal tail deflections needed to maintain $C_{M,\text{cg}} = 0$ across operational angles of attack.

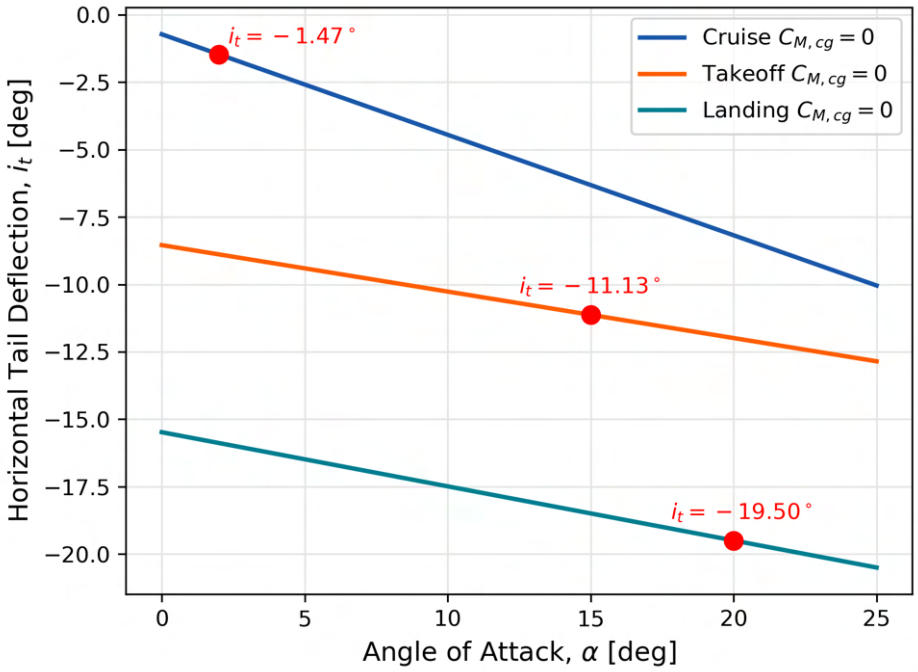

Fig. 57 Trim diagram for cruise, take-off, and landing conditions.

E. Lateral Static Stability

The lateral static stability coefficients evaluated at loiter, cruise, and dash are seen in Table 35 (units of rad^{-1}). These values were calculated using equations from Nelson [30] and validated with AVL. Each derivative displays the appropriate sign required for static stability.

From the magnitude variations across flight regimes, a pattern where stability derivatives reach their peak values at cruise conditions is seen. The observed reduction in derivative magnitudes from cruise to dash is consistent with compressibility effects at higher Mach numbers. The lower derivative values at loiter speeds reflect reduced dynamic pressure, although the aircraft maintains sufficient stability margin throughout this slower flight regime.

Table 35. Lateral Static Stability Coefficients

	C_{y_β}	C_{l_β}	C_{n_β}	C_{y_r}	C_{l_r}	C_{n_r}	C_{y_p}	C_{l_p}	C_{n_p}
Loiter	-0.32	-0.14	0.08	0.27	0.07	-0.16	0.06	-0.24	-0.01
Cruise	-0.70	-0.24	0.30	0.59	0.15	-0.34	0.10	-0.49	-0.02
Dash	-0.57	-0.18	0.22	0.47	0.11	-0.27	0.06	-0.39	-0.01

F. Dynamic Stability

The dynamic stability analysis conducted for the Homelander examined the aircraft's response to disturbances over time, characterizing the oscillatory behavior and convergence rates of the various motion modes. For the Homelander, longitudinal dynamic stability was evaluated at the cruise condition against Level 1 flight qualities criteria as defined by the Cooper-Harper scale outlined in MIL-STD-1797. Although not a requirement, the Cooper-Harper scale provides advisory insight into the required workload on a pilot. Since the Homelander operates at supersonic cruise speeds, it is categorized as a Category A flight phase, and as an interceptor, it is classified as a Class IV aircraft according to military specifications. Thus, the Level 1 flight quality criteria for Class IV Category A was used as the baseline requirements for this analysis.

1. Longitudinal Dynamic Stability

The longitudinal dynamic stability assessment focused on calculating the natural frequency and damping ratios for both the short period and phugoid modes to ensure compliance with handling qualities standards. The longitudinal dynamic stability results in Table 36 show that the short period mode meets Level 1 requirements, with a natural frequency of 0.57 rad/s and a damping ratio of 0.90. The phugoid mode damping ratio is 0.04, which is exactly at the Level 1 threshold and therefore meets Level 2 criteria. This indicates the aircraft will exhibit lightly damped long-period oscillations, but the short period response remains well within acceptable limits for handling qualities.

Table 36. Longitudinal Dynamic Stability Flight Qualities

	ω_{n_p} [rad/s]	ζ_p	$\omega_{n_{sp}}$ [rad/s]	ζ_{sp}
Level 1 Requirement	-	>0.04	-	$0.35 \leq \zeta_{sp} \leq 1.30$
Actual Value	0.08	0.04	0.57	0.90

2. Lateral Dynamic Stability

The lateral dynamic stability analysis evaluated the aircraft's Dutch roll characteristics, roll mode time constant, and spiral mode doubling time to verify compliance with handling qualities criteria. As shown in Table 37, the Homelander meets Level 1 handling quality criteria for three of four critical criteria. The Dutch roll natural frequency ($\omega_{n_{DR}}$), roll mode time constant (τ_r), and spiral mode doubling time ($T_{2,s}$) exceed requirements, ensuring responsive roll control and manageable spiral divergence. However, the Dutch roll damping ratio falls below the Level 1 threshold, but remains within Level 2 acceptability.

Table 37. Lateral Dynamic Stability Flight Qualities

	$\omega_{n_{DR}}$ [rad/s]	ζ_{DR}	τ_r [s]	$T_{2,s}$ [s]
Level 1 Requirement	>1.00	>0.19	<1.00	>12
Actual Value	2.86	0.03	0.57	12.81

XI. Loads & Dynamics

The structural integrity of every engineering design must be tested. This can be achieved through load analysis by evaluating various loads such as aerodynamic, gravitational, and operational loads that will impact the Homelander's flight. Evaluating these forces help engineers to support a design's safety and durability and make integral structural decisions. This analysis helps design strong, lightweight structures while maximizing performance and minimizing failures.

A. V-n Diagram

The V-n diagram, or flight envelope, defines the structural and aerodynamic operational limits of the aircraft. It presents the relationship between velocity and load factor, accounting for both maneuver-induced and gust-induced loads. This helps the team ensure the structural resilience of the Homelander under various flight conditions, in compliance with MIL-A-8861. The maneuver envelope was generated using Raymer's methodology [6] and the criteria in MIL-A-8861C (Section 3.5.2). The gust envelope was constructed using Nicolai's gust load equations [9] in conjunction with MIL-A-8861C (Section 3.5.1) guidelines, which define atmospheric disturbance velocities of 25,

50, and 66 ft/s. To meet the RFP's performance requirement of a maximum instantaneous turn rate of 18 deg/s [1], the upper limit load factor was increased from the specified +7g to +8g. This adjustment allows the aircraft to remain structurally viable during aggressive high-rate maneuvers. The lower limit remained at -3g. A 1.5 safety factor was applied to both bounds to define ultimate loading conditions used in structural analysis, consistent with MIL-A-8861C. The critical airspeeds and parameters used to construct the envelope are summarized in Table 38.

Table 38. V-n Diagram Speeds

Cruise Speed	Pos. Stall Speed	Neg. Stall Speed	Dive Speed
445.40	136.80	193.50	742.30

These include positive and negative stall speeds, cruise and dive velocities, and corresponding load factors. The design cruise Mach number was set at 1.1 and the dive Mach number at 1.6, resulting in an equivalent dive speed of 742.3 knots. The maneuver envelope reflects the aircraft's controlled operational limits, while the gust envelope ensures the structure can withstand sudden aerodynamic disturbances across different flight conditions. Using this information, the V-n diagram is plotted in Fig. 58.

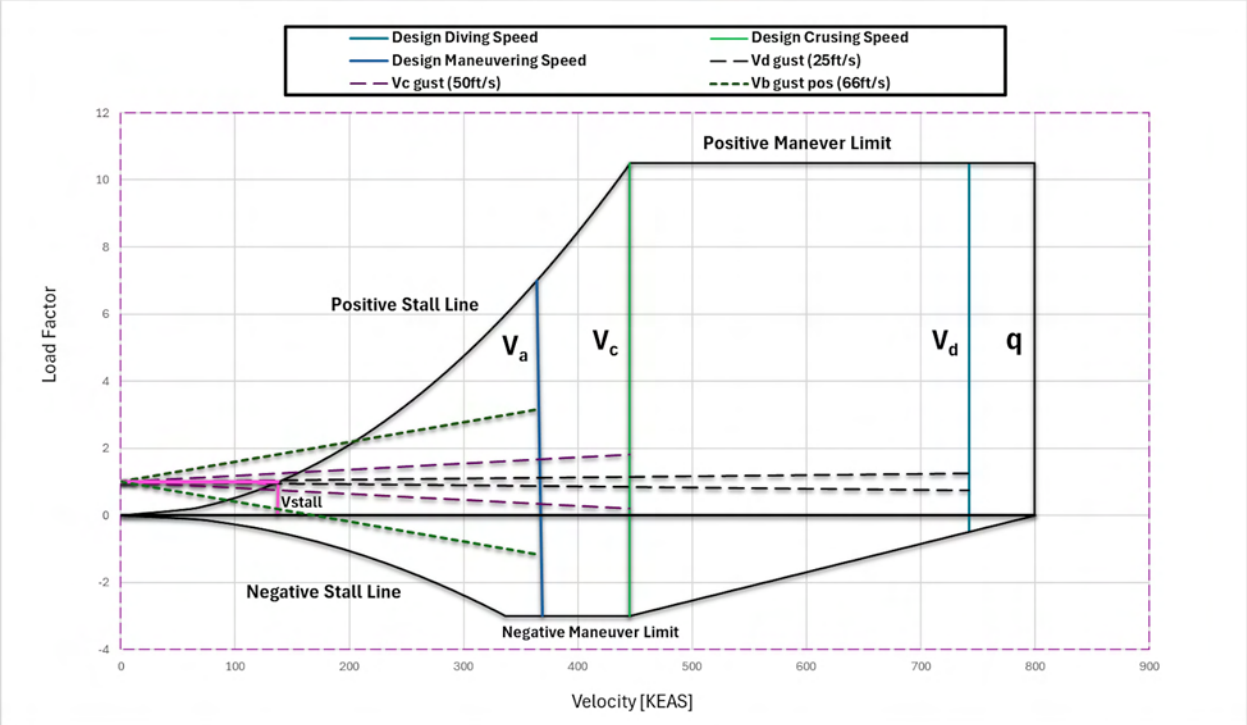

Fig. 58 V-n Diagram.

B. Lift Distribution

An analysis of the aircraft's load distribution over the wing was conducted, focusing on the half-span measured from the wing-fuselage intersection to the wingtip. The initial load considered was the lift distribution, determined using AVL at an angle of attack near stall to capture the largest loads the aircraft may encounter. The weight of the wing was then included, approximated using the aircraft's CAD model as described in the Mass Properties Section IX. Additionally, 600 lb fuel tanks were added at the wingtips to represent the heaviest possible tip loading, making this the most constraining scenario.

Taking these three loads into account, the total load distribution was calculated. Figure 59 illustrates the resulting half-span lift distributions under +8g and -3g loading conditions. The inclusion of the 600 lb fuel tanks introduces a modest increase in loading near the tank attachment locations, slightly altering the overall distribution and increasing the structural demand near the wing root.

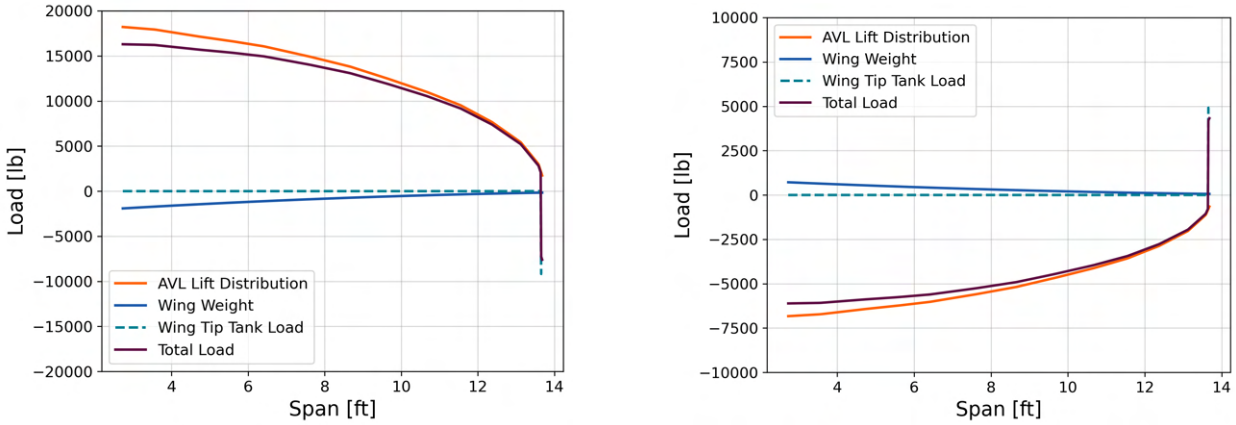

(a) Positive 8g lift distribution.

(b) Negative 3g lift distribution.

Fig. 59 Positive and negative lift distribution across the half-span.

C. Shear and Bending Moments

The half-span load distributions were used to generate the shear force and bending moment diagrams for three key load cases: +8g maneuver, -3g maneuver, and 2.5g landing with a safety factor of 1.5 applied. These are shown in the two subplots of Fig. 60. For each case, the plots illustrate how the loads vary along the wing span, with the most critical values consistently occurring at the wing root. In the +8g maneuver case, the shear force reaches a maximum negative value of approximately $-150{,}000$ lb at the root, while the corresponding bending moment peaks at over 600,000 lb $\cdot$ ft. These values highlight the large structural demands imposed during high-g maneuvers, which requires reinforcement in the root region. The -3g case, while less severe, still results in a substantial positive shear force of about 50,000 lb at the root and a negative bending moment approaching $-200{,}000$ lb $\cdot$ ft. The 2.5g landing scenario produces intermediate values, with a negative shear force and a bending moment that show it is not a constraining load case for the wing.

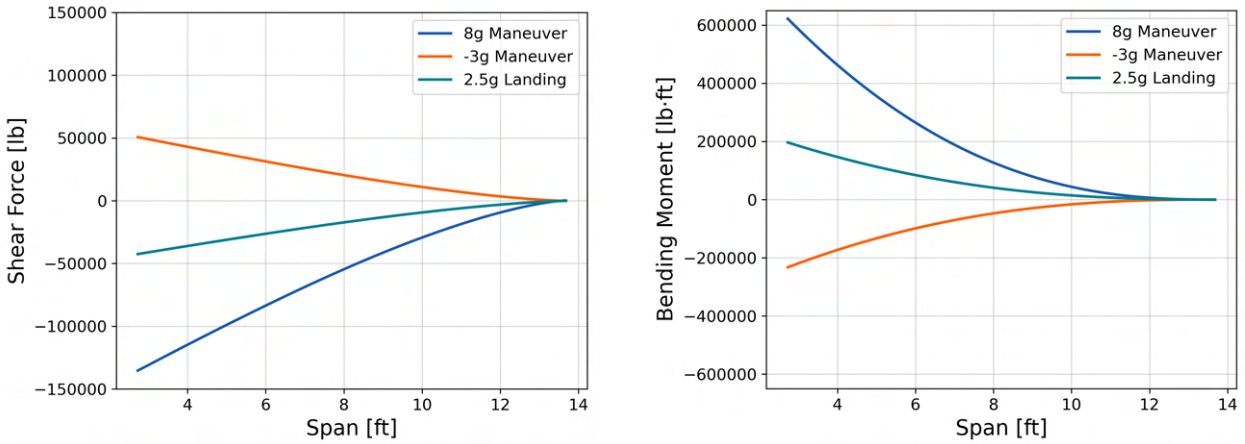

(a) Shear force distribution across the half-span.

(b) Bending moment distribution across the half-span.

Fig. 60 Bending and shear force for three different load cases.

D. Load Paths

Load path diagrams for the Homelander in steady level flight and on the ground are seen in Figs. 61a and 61b. The arrows seen within the figures represent the direction of travel for each corresponding force the aircraft must withstand. As illustrated in Fig. 61a, the lift generated by the wings is transmitted to the fuselage primarily through the main spars and ribs, forming the primary load path. These structural elements carry the bending and shear forces induced by lift and the weight of the wing and fuel tanks. A robust spar system is essential to distribute these loads efficiently across the wing root and fuselage.

The majority of the aircraft's static weight is supported by the main landing gear as seen in Fig. 61b, which transfers forces vertically through the fuselage structure and shock-absorbing elements. The nose gear helps stabilize the aircraft and prevents forward pitching. The downward force of the wingtip tanks induces bending, which is counteracted by the spars and reinforced wing root, maintaining structural balance and preventing excessive stress at rest.

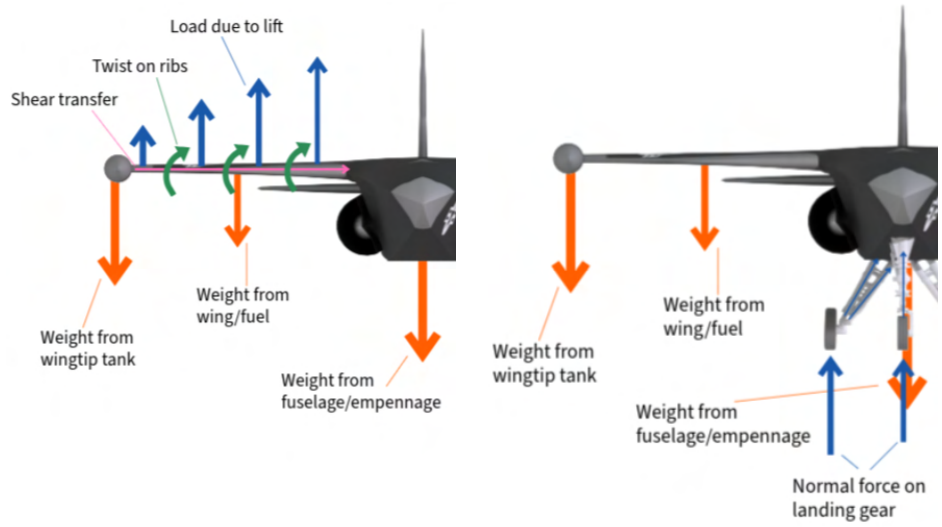

(a) Steady Level Flight **(b) Landing Gear Extended**

Fig. 61 Comparison of load paths during steady level flight and ground roll with landing gear extended.

XII. Structures

Structures are a crucial component of the Homelander's abilities to meet the requirements laid out in the RFP [1]. An optimal structural design would meet the loading requirements as outlined in the previous sections in addition to minimizing the overall weight and cost of the aircraft. Structural sizing considerations were guided by MIL-HDBK-516C Section 5. The following sections outline the team's design process for the major-load bearing components of the aircraft with the full structural configuration shown below in Fig. 62.

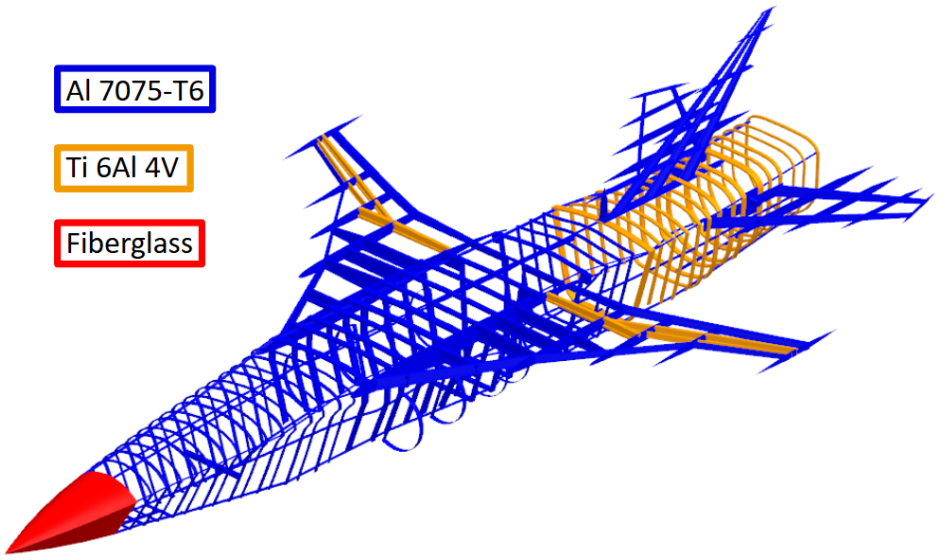

Fig. 62 Full internal structural configuration with materials labeled.

A. Materials

The team explored various common aircraft materials used in the aerospace industry to meet the demanding loading forces during flight. This resulted in a trade study of the various aircraft materials, as shown in Table 39. This table highlights important properties such as: material strength, density, and raw material cost. These are key parameters when evaluating which materials will be assigned to different components, while achieving the aerodynamic goals of the aircraft. This requires a strong but lightweight aircraft. A lighter aircraft boasts several benefits for the required missions, including fuel savings and cost savings. This would indicate that a composite material would be ideal from a structural perspective, however, they tend to have a large raw material cost. From the material trade study, it was found that aluminum alloys proved to be superior in balancing the high material strength needs, low cost requirement, and the desire for a lighter aircraft. This was further supported through the analysis of similar aircraft such as the F-16, whose airframe is nearly made up of 80% aluminum [31]. The materials and their qualities used for this trade study are detailed in Table 39.

Table 39. Table of Aircraft Material Properties [32, 33]

Material	E [KSI]	ν	σ_{ult} [KSI]	σ_{yield} [KSI]	ρ [lb/in^3]	Cost [$/lb]
Aluminum 2024-T3	10.47×10^3	0.33	65.05	47.01	0.1005	3.97
Aluminum 7075-T6	10.36×10^3	0.33	78.03	71.03	0.1005	3.97
Aluminum Lithium	11.15×10^3	0.33	104.45	98.81	0.0921	4.45
Titanium 6Al-4V	15.95×10^3	0.31	134.13	126.14	0.1617	35.84
Steel AISI4340	29.01×10^3	0.32	259.56	215.43	0.2826	0.55
E Type Fiberglass	10.47×10^3	–	50.07	–	0.0903	3.97
T800 carbon fiber	42.86×10^3	–	85.42	–	0.0651	254.43

The team then compared different Aluminum Alloys, 2024-T3, 7075-T6, and Aluminum Lithium to determine their best application on the aircraft. Aluminum Lithium is lighter and stronger compared to the other alloys the team explored, but has one major downfall, the alloy has less ductility, making it difficult to shape and overall more brittle. Due to Homelander's unique configuration such as the the varying sweep of the wing, many structural components include complex geometries that would not be ideal for this material. The 2024-T3 alloy has excellent fracture toughness, a slow crack growth rate, and good fatigue life [32]. The 7075 alloy has a higher strength than 2024 but lower fracture toughness [32]. Therefore, the 2024-T3 alloy is best used for aircraft skins, which will be prone to fatigue due to the tensile stress experienced during their design life. The 7075-T6 alloy will be used in the internal structure of the wing and fuselage due to higher yield and ultimate stress [32]. For Homelander's radome, the team will use fiberglass as it is not a major load-bearing component and will house the avionics, requiring a material with radio frequency (RF) transparency. The empennage of the aircraft will be constructed with AL 7075 materials in addition to Titanium 6AL-4V for engine integration components. Titanium is ideal for this application because of its high overall melting point.

B. Wing

The unique aerodynamic capabilities of the Homelander are reflected in its intricate wing geometry design. This increases the complexity in analyzing the structural components of the wings. A combination of empirical methods described by Howe [34] and trade studies was used to size the components of the wing, spars, and ribs, as shown in Fig. 63. The wing design is an 8-spar and 5-rib configuration based on a qualitative trade study that included fighters of a similar size or wing geometry such as the F-16, F-16XL, and Saab 35 Draken [35]. The front and rear spar are parallel to the leading and trailing edge of the aircraft, while the interior spars follow the taper of the wing [35, 36].

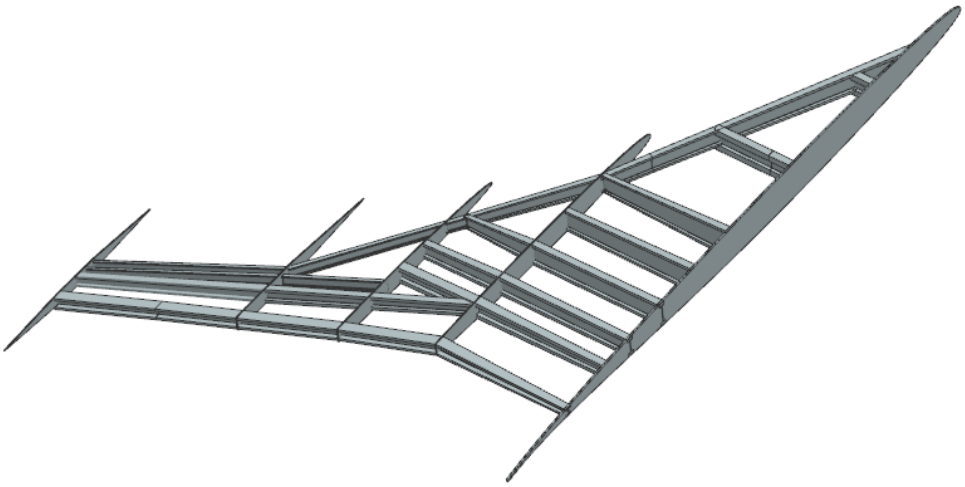

Fig. 63 CAD of internal wing structure.

The ribs were studied similarly and set to a thickness of 0.3” with two cutouts to reduce weight and allow for the connection between the wing cells. The ribs are evenly spaced to minimize the wing-skin thickness in order to prevent buckling [35]. The dimensions of the spars are shown in Table 40. The spars were designed as I-Beams as this structure is able to resist bending which is critical for the wing [34]. The moment on the spars is derived from the loads outlined earlier in the report. From the mid chord, the spars linearly taper in dimension up to the root.

Table 40. Spar Dimensions

Wing Location	Spar Location	Flange	Web Thickness
Root Chord	Forward	1.50” x 1.00”	0.25”
	Middle	1.00” x 1.00”	0.25”
	Aft	1.50” x 1.00”	0.25”
Mid Chord	Forward	1.50” x 1.00”	0.25”
	Middle	1.00” x 0.75”	0.25”
	Aft	1.00” x 1.00”	0.25”

The wing skin is a non-homogeneous skin thickness that was iterated upon in Abaqus FEA software with a full wing structure buildup to determine an ideal skin thickness. The wing skin tapers linearly from the root to the tip from 0.40”-.05”. This aligned with values traditionally observed in the design of fighter aircraft of 0.02”-0.08” at the tip [37]. The results of the FEA for the highest loading conditions are shown in Figs. 64a and 64b. These conditions include the dynamic pressure requirement of 2,133 psf and the 18 deg instantaneous turn. The FEA analysis validated the design of the wing and the previous empirical sizing methods while meeting the loading requirements with a minimum safety factor of 1.5 on the ultimate loads.

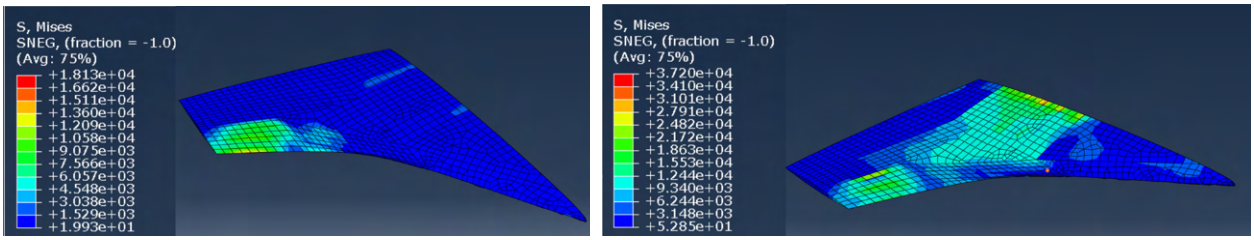

(a) FEA results of 2,133 psf dynamic pressure loading. **(b) FEA results of an instantaneous 18 deg turn loading.**

Fig. 64 FEA results for the highest loading conditions defined by the RFP.

C. Fuselage

During sizing of the internal dimensions of the fuselage, a fighter similarity analysis identified common practices regarding the spacing of frames, stringers, and longerons. This revealed the common practice of a semi-monocoque with frames of many aircraft that are evenly spaced on average about 10 inches apart [38]. The length of these frames near major loads such as the wing are at 4% of the fuselage length, sized according to methods described by Howe [34]. Since the fuselage is not pressurized, the depth varies from 1 to 1.5 inches based on its location.

The team explored various longeron cross sections such as circular, rectangular, T-channel, and C-channel. Circular and Rectangular longeron improve the torsional rigidity, which is critical for the fighter that will be completing high-g maneuvers. The C-channel or T-channel tubing have a lower structural weight, but a lower torsional rigidity compared to closed cross-sections [39]. However, due to the large operating altitudes of this fighter, it is likely that it will be exposed to conditions that may create moisture within the structure. This would indicate that for repair and maintenance, the C-Channel is ideal to prevent corrosion, which would be detrimental to the structural strength of the aircraft. This decision aligns with MIL-HDBK-516C Section 7.6.1, which requires corrosion protection for primary structure in prolonged service environments. This same methodology was applied to the section of the stringers. The longerons are placed at each corner in addition to the top and bottom of the aircraft. Between the side-mounted longerons, stringers bisect the longerons. The dimensions of these materials are listed in Table 41. Additionally, any material cutout because of bays, landing gear, and maintenance are reinforced with stiffeners.

Table 41. Dimensions of C-channel Stringers and Longerons

Component	Width x Height	Thickness
Stringer	1.00” x 1.00”	0.25”
Longeron	2.00” x 1.00”	0.25”

A defining characteristic of the Homelander is its high-wing configuration, which significantly influences the design of the fuselage-to-wing joint. This structural interface is critical to the fighters design, as it must accommodate load transfer between the wing and fuselage, while maintaining aerodynamic efficiency and structural integrity. In the final design of the Homelander, the wing ribs and spars intersect directly with the fuselage frame, creating a joint that connects to the fuselage. The final fuselage structure is shown in Fig. 65 below.

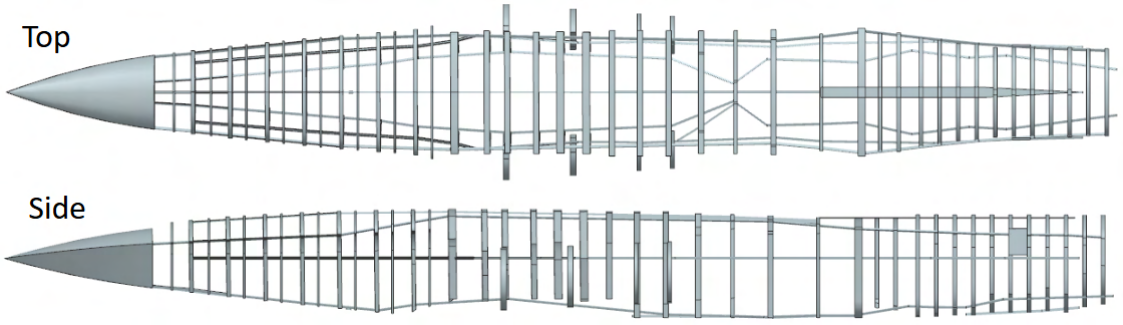

Fig. 65 Top and side view of CAD fuselage structure.

The front of the fuselage includes a radome made of fiberglass to allow for avionics that require RF capable materials. The Radome is not a load-bearing component that only requires the ability to maintain its shape during flight. This resulted in a radome with 0.27” thickness [35]. Similarly, the aircraft skin thickness for the fuselage is approximately 0.125” thick [40].

D. Empennage

The empennage of the aircraft is a multispar design for the vertical and horizontal tails. The vertical and horizontal tails are securely connected to the aircraft’s aft fuselage frames. Specifically, the horizontal tail is mounted between two fuselage frames, which serve as the primary structural supports for the tail assembly. These frames are positioned such that a pivot mechanism allows the stabilator to rotate. Structural design of empennage components follows the fatigue and fail-safe criteria defined in MIL-HDBK-516C Section 7.4.2.

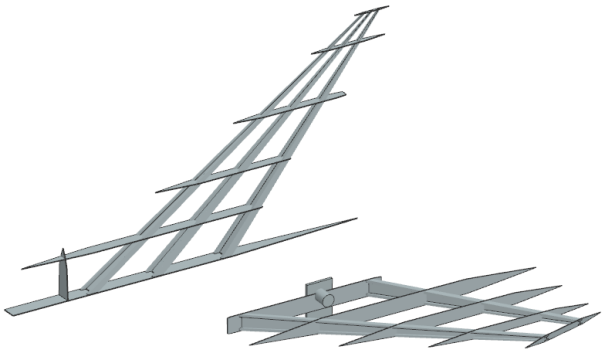

Fig. 66 CAD of internal empennage structure.

The multispar configuration in both tails not only improves torsional rigidity and strength but also allows for a more efficient transfer of aerodynamic and inertial loads back into the airframe. This structural strategy is particularly important in high-performance or dynamically unstable aircraft, where the tail surfaces endure significant forces during maneuvering. Figure 66 visualizes the empennage structure.

XIII. Landing Gear

The landing gear system is a vital element of the Homelander aircraft, ensuring safe ground, take-off, and landing operations, while also maintaining minimal storage space in the fuselage. Drawing on proven UAV designs and industry standards, the landing gear system was optimized for reliability, maintainability, and minimal weight. The following section outlines the key design choices, sizing methods, and placement considerations that define the final landing gear arrangement.

A. Landing Gear Configuration and Sizing

A tricycle landing gear configuration was selected for the Homelander, as it offers the most space-efficient solution for interceptor-class aircraft. Both the main and nose gear are designed to deploy aft to forward, following the precedent set by the MQ-9A Reaper, an autonomous UAV with a similar deployment scheme [41]. This approach is cost-effective for unmanned platforms, whereas forward-to-aft deployment is typically used on crewed aircraft to enhance safety during hydraulic failures.

The nose gear placement is constrained to a narrow region between the weapons bay and radar, while the main gear is positioned near the engine, where more space is available. Both gear legs are sized to provide a minimum ground clearance of 46.5 inches from the fuselage, ensuring sufficient space for PW-229 engine maintenance and removal. Gear loads were determined through moment balancing within the aircraft's CG limits, and initial sizing of oleos

and tires followed Raymer's methodology [6]. This is in compliance with the landing gear functionality standards in MIL-HDBK-516C Section 5.4.1. With this sizing method, trial and error of placing the gear in different spots within the constraints discussed was done to minimize expected gear loads, so that gear overall weight could be minimized. For expected braking loads, Raymer was again used to calculate the expected kinetic energy of the aircraft landing at MTOW [6], which is the worst case emergency landing situation. Tire selection from the Goodyear catalog prioritized minimal volume to optimize storage within the airframe [42]. With tires selected, maximum expected braking load was determined by guessing and checking minimum landing field lengths required to come to a full stop. These braking loads where then compared to the selected tires rated braking loads to ensure the aircraft could come to a full stop in a given landing field length, which in the end resulted in a minimum landing field length of 3,100 ft to be underneath the rated tire braking loads. A hydraulic actuation system, as common in industry with the Reaper being a notable example [41], was chosen for gear deployment and retraction. For gear locations, datum was still defined at the nose tip, where X-axis points towards the aft of the plane along the aircraft centerline, Y-axis points towards the right wing, and Z-axis points up directly opposite to where gravity would be acting on the aircraft. Table 42 summarizes the final loads, dimensions, and locations for both the main and nose landing gear.

Table 42. Landing Gear Specifications

Parameter	**Main Gear (1x)**	**Nose Gear**
X Location [in]	450	120.5
Y Location [in]	±16	0
Z Location [in]	−25	−12.9
Tire Diameter [in]	22	18
Tire Width [in]	6.6	5.5
Expected Max Load [lb]	11,650	5,990
Rated Load [lb]	12,000	6,200
Expected Max Braking Load [lb]	N/A	8,880
Rated Braking Load [lb]	18,000	9,300
Rated Tire Speed [MPH]	190	239
Stroke [in]	8.8	8.8
Oleo Diameter [in]	2.82	3.90
Oleo Pressure [psi]	1,800	1,800

B. Landing Gear Tipback and Overturn Angles

The landing gear placement requirements are to not exceed maximum tip back or overturn angles. The tip back angle is the angle measured from the vertical centerline of the main gear's contact point with the ground to the aft-most point on the aircraft. This measures 17.5 deg for the Homelander's configuration. This angle must not exceed the angle measured from the vertical centerline of the main gear's contact point to the CG of the aircraft, as stated by Raymer [6]. Shown in Fig. 67, the angle between the vertical and CG location is 34.9 deg, thus satisfying the tip back requirement. The overturn angle is measured from the ground to the angle made with the line connecting the center of gravity to main gear's contact point with the ground, and this angle need not exceed 63 deg, also as stated by Raymer [6]. This angle is 61.2 deg as shown in Fig. 68, which satisfies the overturn angle requirement.

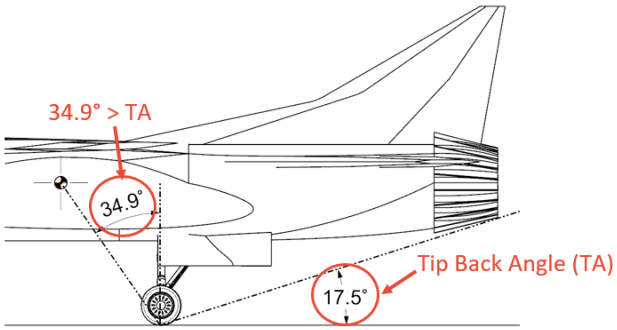

Fig. 67 Main gear tipback angle.

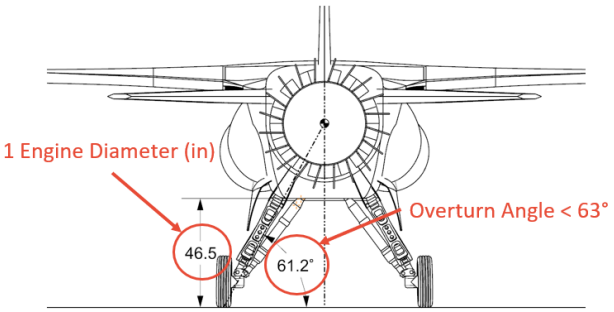

Fig. 68 Main gear overturn angle.

C. CAD Renderings

With gear specifications and locations determined, final landing gear models for the nose and main gear were created using Siemens NX CAD software. Table 42 dimensions were utilized in the models. The tricycle style landing gear placement are shown in the Figs. 69 - 72 in the stowed and deployed configuration for both the main and nose gear.

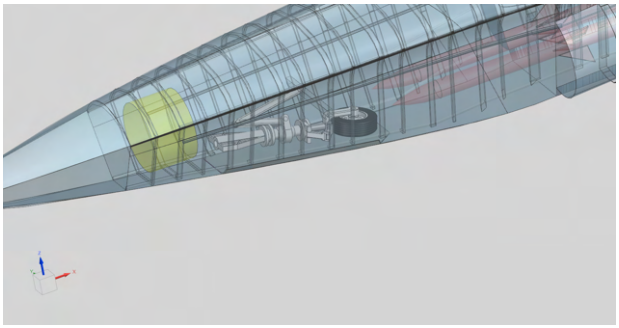

Fig. 69 Nose gear stowed.

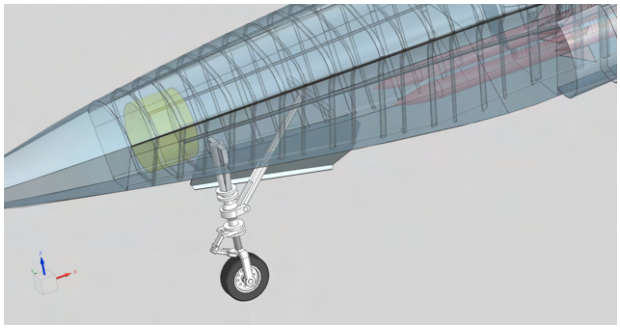

Fig. 70 Nose gear deployed.

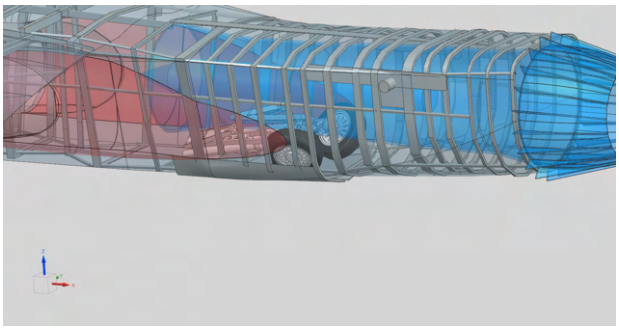

Fig. 71 Main gear stowed.

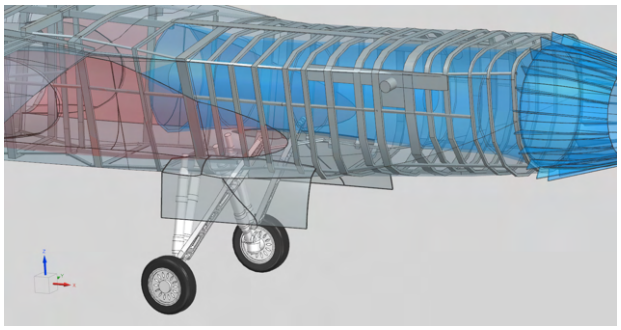

Fig. 72 Main gear deployed.

D. Turn Diagram

The RFP never states anything explicit about turn requirements for the aircraft during taxi phases, although it does specify that the aircraft must be capable of operating on NATO runways [1]. With this in mind, NATO does publish standardized runway dimensions [43]. Using these dimensions, it was assumed that the aircraft needs to maintain its position along the runway centerline. It was found that the aircraft must have a nose gear angle (with respect the aircraft's centerline) of 25 deg with a pivot point 786 in. away from the nose gear. Figure 73 shows a turning diagram of the team's aircraft with these specifications in mind to allow for operation on NATO runways.

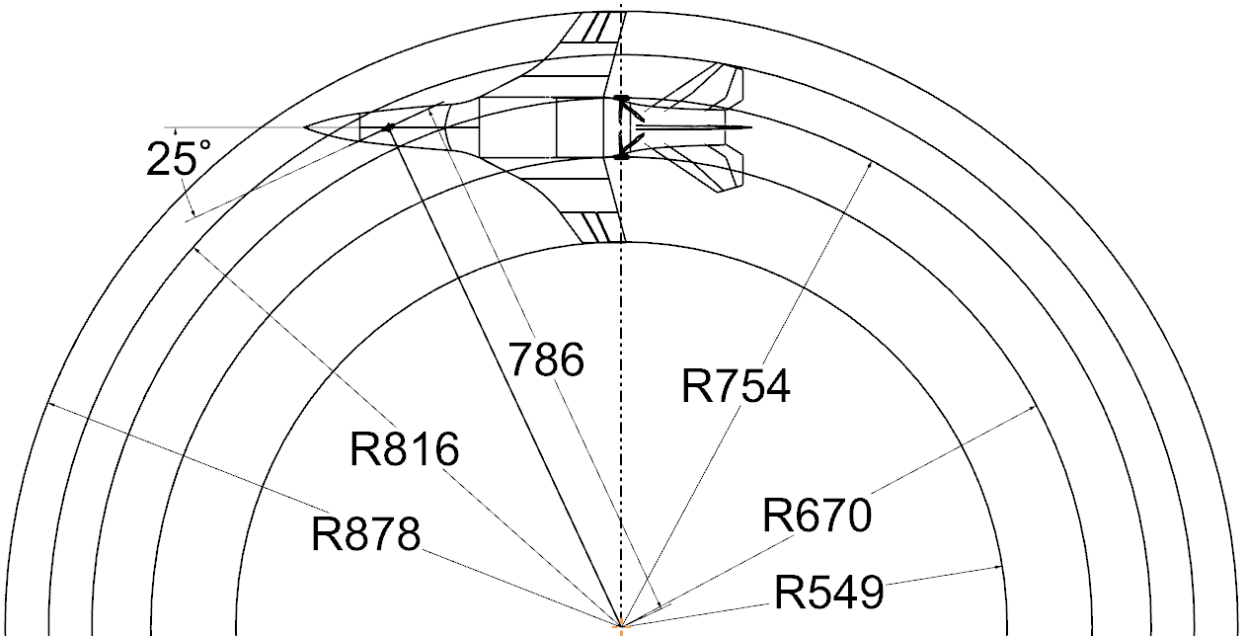

Fig. 73 Turn diagram of Draco aircraft (inches).

XIV. Systems

The Homelander's systems architecture is designed to support high-performance, unmanned missions with a focus on survivability. The suite of subsystems, flight control, engine management, fuel delivery, and electrical power are designed for redundancy and minimal dependence on external support, inspired by proven systems on fighters like the F-16 [40].

A. Flight Control and Navigation System

The Homelander utilizes a fully digital fly-by-wire (FBW) flight control system. It includes quadruple redundant flight control computers (FCC) fed by redundant air data sensors, rate sensors, and accelerometers. The FCCs continuously process inputs from pilot commands, accelerometers, rate sensors (yaw, pitch, roll), air data sensors, and airflow sensors. The system is powered through the Essential DC Bus, with redundancy built in through the emergency power system adhering to MIL-HDBK-516C Section 9.1.1 for flight control systems, ensuring redundancy and operational integrity under failure conditions. Each FCC calculates control surface commands, compares and cross-checks them with the other FCCs, and then sends signals to the actuators that move the control surface. A diagram of the Flight Control System can be seen in Fig. 74. The quad-redundant FCCs with cross-monitoring, sensor redundancy, and emergency power systems increase the survivability of the aircraft in the cases of subsystem failure or battle damage.

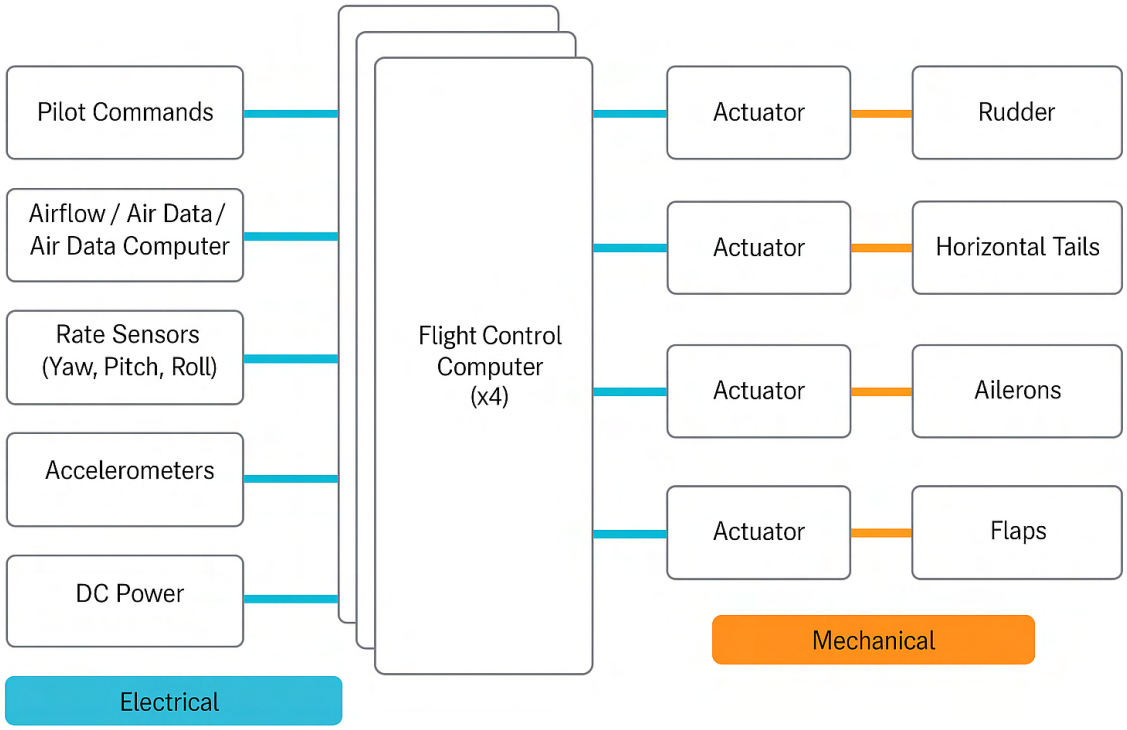

Fig. 74 Diagram of flight control system.

Collins Aerospace supplies the Athena Redundant Flight Control and Navigation System for unmanned aerial systems and is the choice product family employed on the Homelander [44]. The product offers the modes and functions listed in Table 43.

Table 43. Autopilot Modes and Navigation Functions

Autopilot Modes	Navigation Functions
Pitch Rate Command	3-D Waypoint Tracker
Attitude Hold	Auto-Take-off
Airspeed Hold	Auto-Approach and Landing
Vertical Speed Command	Emergency Mission Management System
Altitude Hold	Lost Link
Glide-Slope Tracker	
Roll Rate Command	
Turn Rate Command	

B. Engine Control System

Engine control on the Homelander will be handled by a full authority digital engine controller (FADEC), which is a digital system for precise and autonomous engine controls. The FADEC is integrated into the Vehicle Management System available in the RFP under GFE [1]. The unit continuously monitors inputs, from either the ground control station operator or the autopilot computer, to send signals to the actuators which adjust fuel injection rates and airflow to the engine. Various sensors are integrated into the system to monitor temperature, pressure, and airflow, providing data back to the Vehicle Management System in a similar manner to the FBW system for flight control. Additionally, the system will handle engine start-up commands. A diagram of this system can be seen in Fig. 75.

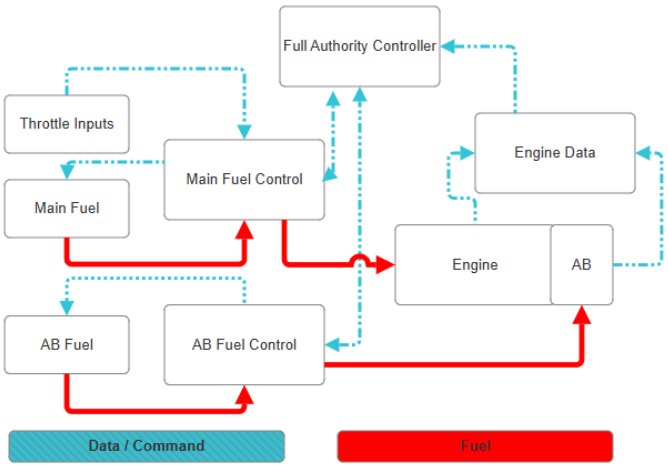

Fig. 75 Diagram of engine control system.

The redundancy of the system is similar to that of the FBW system for flight control, as there are multiple computers, actuators, and fire detection units. This system's computers will be placed in the aircraft's dedicated avionics space, while the actuators and hydraulic system will be spread across the fuselage connecting the fuel system to the engine.

A jet fuel starter (JFS) will be used for engine start-up. The JFS utilizes the aircraft's onboard fuel supply to drive a small turbine, which generates the necessary mechanical energy to start the F100-PW-229. The model selected for this aircraft is the same model utilized on the F-16, which also uses the F100-PW-229: the Turbomach T-62T-40-8 Titan Jet Fuel Starter [22]. A JFS was selected due to its smaller volume requirement and lower weight compared to the GFE Auxiliary Power Unit [1, 22]. The JFS presents more advantages than just weight and space savings. The F-16 scramble time is one of the fastest. Capable of startup without ground support, the Homelander has a scramble time of 5 minutes with the help of the JFS startup. This is faster than the F-22 and F-35 which utilize highly complex and expensive integrated power plant systems. Seconds and minutes matter in an intercept mission, and the Homelander is saving every second possible using this method.

C. Fuel System

The fuel system is designed to ensure uninterrupted fuel delivery to the engine and manage the aircraft's center of gravity under all operating conditions. The system includes both internal and external fuel storage with tank transfer. The design includes self-sealing tanks. The primary design fuel will be Jet-A (6.7 lb/gal) as required by the RFP [1].

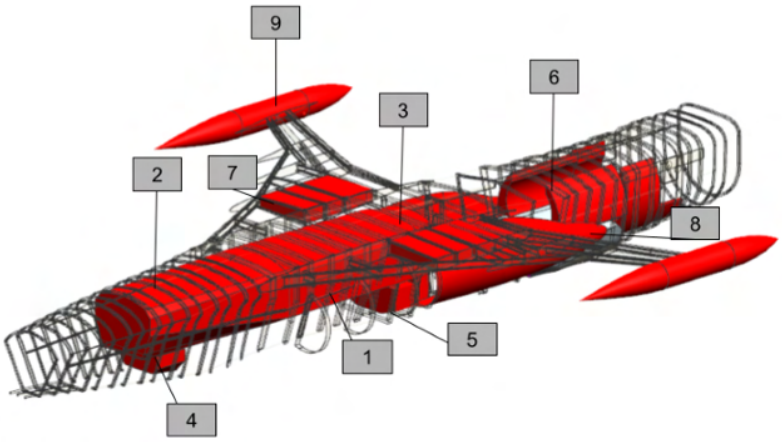

Fig. 76 Full fuel tank capacity and locations.

The majority of the aircraft's fuel is carried in the main internal Fuselage Tanks A and B, with additional capacity provided by smaller internal tanks (Fuselage Tanks C through E), as well as the Left and Right Wing Tanks. Externally, two Wingtip Tanks and two Conformal Tanks add volume with minimal drag impact. Two Reservoir Tanks are incorporated to maintain consistent fuel pressure and supply to the engine during transfer, and also help manage the

aircraft's center of gravity. All fuel, whether from internal or external tanks, is routed through the Reservoir Tanks and a Fuel Flow Proportioner, which balances fuel draw to optimize CG and overall stability. The fuel tank locations can be seen in Fig. 76 with the fuel tank capacities and locations listed in Table 44.

Table 44. Fuel-Tank Capacities and CG Locations

No.	Tank	Capacity [lbs]	Location [in]
1	Fuselage Tank A	5,079	333.21
2	Fuselage Tank B	4,282	237.20
3	Fuselage Tank C	719	392.15
4	Fuselage Tank D	252	207.70
5	Fuselage Tank E	179	377.50
6	Engine Section Tank	184	505.00
7	Wing Tank	628	379.30
8	Conformal Tanks	2,008	419.32
9	Wingtip Tanks Total	1,147	425.67
	Total	**14,478**	

The system utilizes fully electric fuel pumps for both transfer and engine feed. Electric pumps were selected over hydraulic alternatives to reduce system complexity and enable more precise electronic control through the fuel management system. The pumps will be routed through the DC Essential Bus, which remains powered by the emergency generator or battery in the event of electrical failure or engine failure.

All internal tanks on the Homelander are self-sealing as required by the RFP [1], increasing survivability in the case of battle damage. The volume of the self-sealing tank was considered in the tank capacity calculations, and the overall fuel system design complies with MIL-HDBK-516C Section 10.2.1 requirements for combat survivability, redundancy, and safe operation under failure conditions. A diagram of the entire fuel system can be seen in Fig. 77 with tanks, refuel/transfer lines, and pressurization lines shown.

Additionally, the Homelander is equipped for aerial refueling, enhancing its operational range and endurance. It features a refueling port linked to the fuel line located near Fuselage Tank A, allowing for compatibility with standard boom-equipped aerial refueling tankers such as the KC-135 and KC-46. This system enables mid-air refueling without the need for landing, supporting extended missions and increasing flexibility in deployment. The refueling port is designed to meet current NATO standards, ensuring seamless integration with existing tanker fleets.

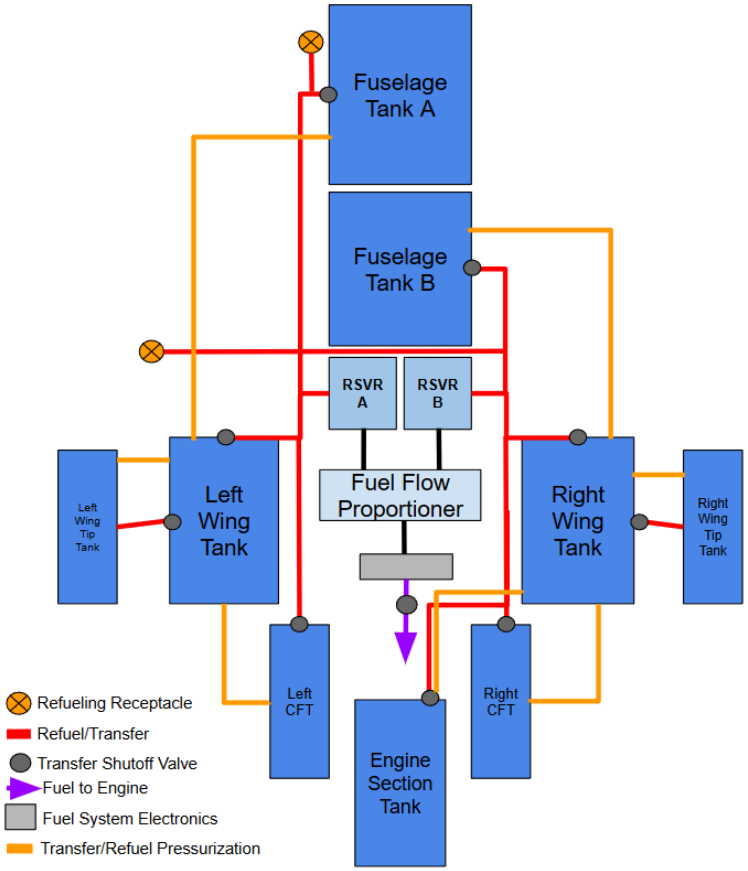

Fig. 77 Diagram of the fuel system.

D. Electric System

The Homelander's electrical power system is a multi-bus AC/DC architecture designed to ensure continuous power delivery to all onboard systems under both normal and emergency conditions. The system is based on the F-16's electrical design, with adaptations for unmanned operation [40]. Primary power is supplied by an engine-driven integrated drive generator (IDG), which is supported by a constant-speed drive (CSD) to maintain a steady output. The IDG, mechanically coupled to the engine via the accessory gearbox, is regulated by a generator control unit (GCU). This generator supplies the Primary AC Bus, which powers high-demand AC systems such as radar and the electronic warfare suite, as well as all non-critical AC systems, including ordnance deployment. Critical systems are fed by the AC Essential Bus, while the Emergency AC Bus, powered by a ram-air-turbine-driven generator, supports flight-essential systems during emergencies.

For DC power, the DC Main Bus supplies non-critical loads such as formation lighting and data recorders, while the DC Essential Bus supports critical flight systems. In the event of a total AC loss, the Emergency DC Bus, powered by the onboard battery, ensures continued operation of flight-essential systems, thereby enhancing survivability.

The Homelander is equipped with a ram air turbine (RAT) to provide emergency electrical power in the event of engine or main generator failure. The RAT is a compact wind-driven turbine that extends from within wing when needed. Upon deployment, it supplies power to the Emergency AC Bus to maintain critical systems, as illustrated in Fig. 78. Although the RAT provides less power than the main engine-driven generator, it delivers sufficient energy to sustain flight controls and enable aircraft recovery.

Redundant power sources include the ram-air-turbine-driven emergency generator and an onboard lithium-ion battery, both providing backup to essential loads. If the engine or main generator fails, the in-wing RAT deploys to drive the emergency generator, supplying power to the Emergency AC Bus and emergency electric hydraulic pumps. A static inverter is also available to convert DC battery power into AC, sustaining essential AC loads. Additional redundancy is provided by dual transformer rectifier units (TRUs), automatic bus switching, a backup battery, an emergency generator, and load shedding algorithms that prioritize key loads during failures. This configuration meets MIL-HDBK-516C Section 9.2.1 requirements for a fail-safe, redundant power architecture supporting flight-critical systems. An overview of the electrical system is shown in Fig. 78, with electric loads detailed in Table 45.

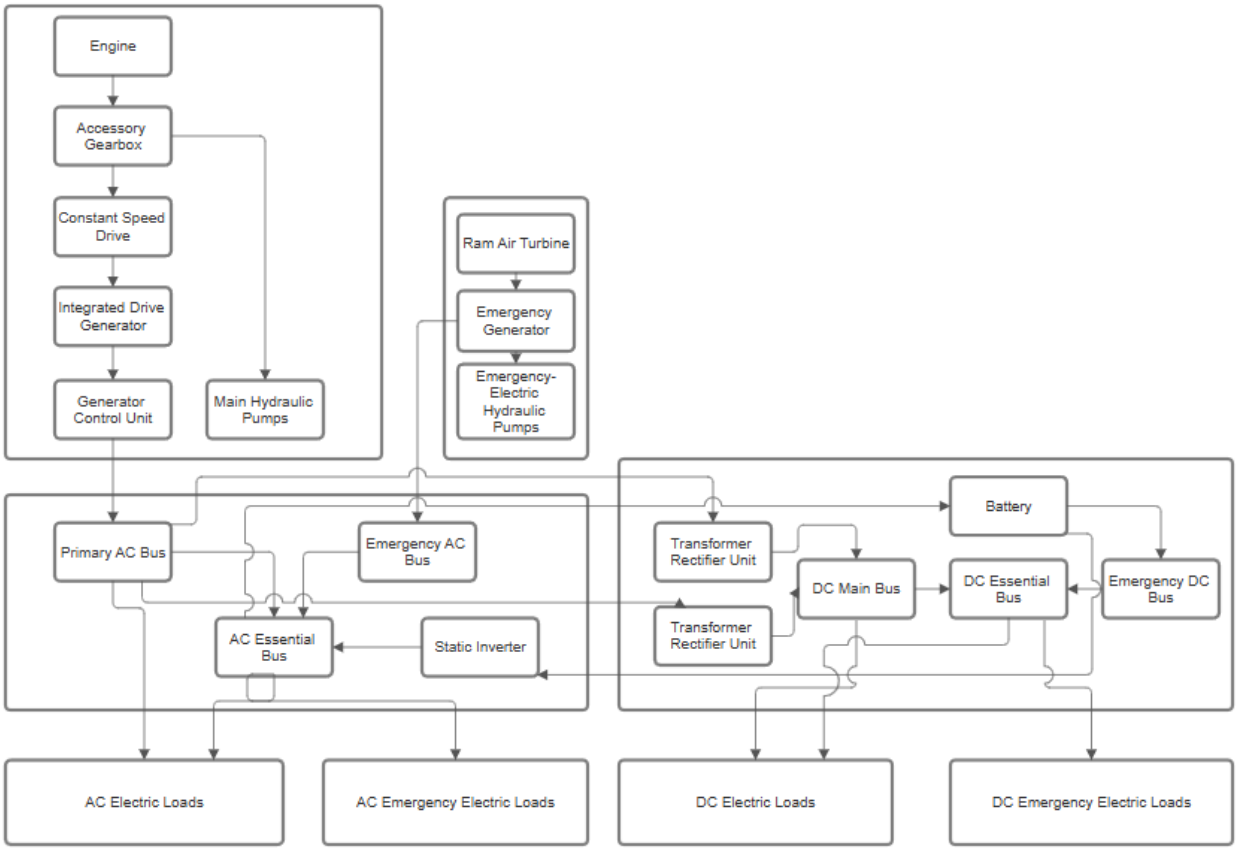

Fig. 78 Diagram of electric system.

Table 45. Electrical Load Classifications

AC Electric Loads	AC Emergency Electric Loads	DC Electric Loads	DC Emergency Electric Loads
Radar	Air Data System	Formation Lighting	Engine Control System
Avionics Cooling	Avionics Cooling	Payload Controllers	Trim and Servo Actuators
EW Systems	Emergency Hydraulic Pump	Battery Charger Power	Air Data Computer
	Essential Actuators	Data Recorders	Inertial Navigation System
	Anti-Icing Systems	Secondary Comms System	GPS
	Landing Gear	Bay Door Actuators	Data Link
			Power Management System
			Emergency Jettison
			Anticollision Light
			Ice/Fire Detectors
			Oil Pressure Indicators
			Fuel System Indicators
			Data Transfer Unit
			Health Monitoring

E. Hydraulic System

The hydraulic system onboard the Homelander is largely based on the system found in the F-16 [40]. The hydraulic system will provide flow to: control surface actuators, the landing gear system, weapon bay doors, the jet fuel starter system, brakes, and the steering system.

The hydraulic system is divided into two subsystems: System A and System B. Both systems will have an engine-driven hydraulic pump, as well as an emergency electric hydraulic pump. The emergency electric hydraulic pumps can be supplied with power independently by the onboard ram air turbine. This design redundancy in the event of engine failure.

For increased survivability and redundancy, both System A and System B will provide flow flight controls, landing gear, and brakes. Additionally, System A will provide flow to the jet fuel starter, and System B will provide flow to the bay doors. In the case of engine failure, only one system will need to be operable to maintain flight control of the Homelander for recovery and landing operations.

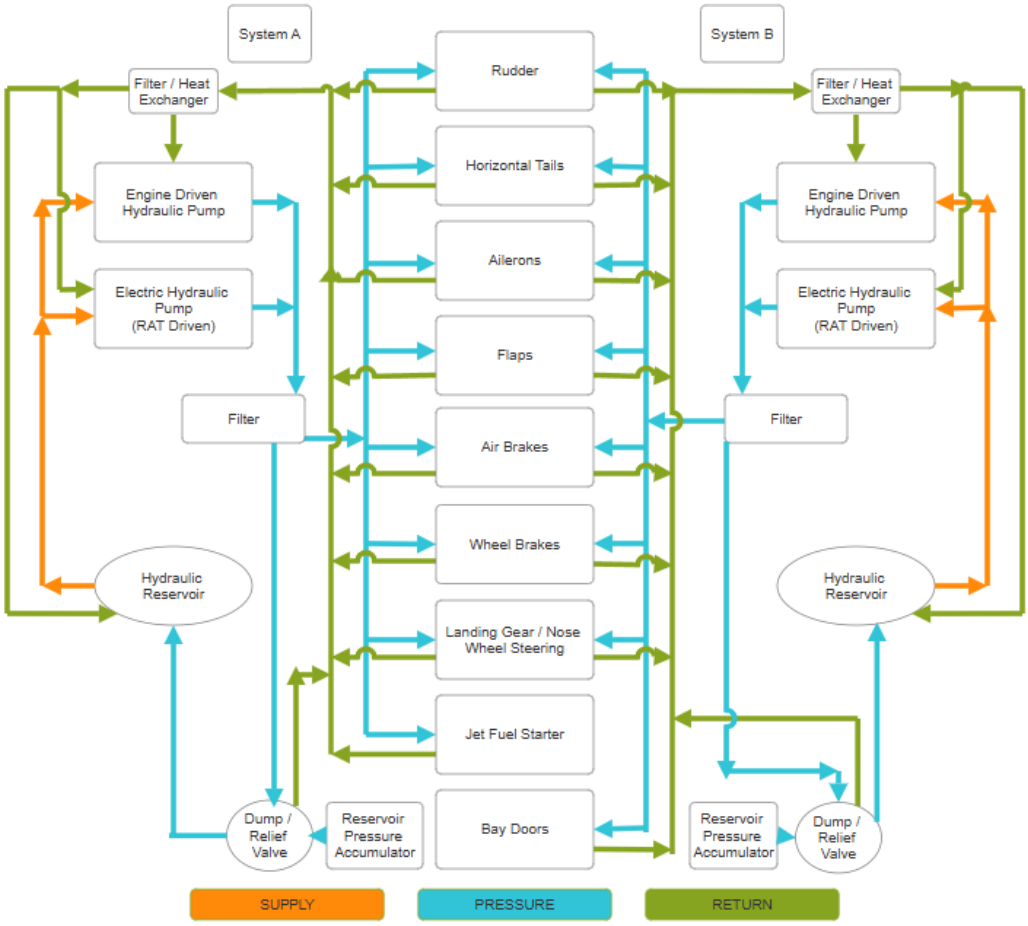

Fig. 79 The hydraulic system diagram.

F. Environmental Control/Pneumatic System

Since the Homelander is an unmanned platform, the environmental control system (ECS) does not require traditional cockpit temperature regulation, cabin pressurization, or onboard oxygen generation. Instead, its primary roles are focused on avionics thermal management, ordnance bay temperature control, and providing necessary pressurization and venting for sensitive components. The ECS is composed of elements such as the avionics cooling loop, airframe cooling ducts, heat exchangers, ram air intake and outlet, liquid cooling systems, temperature sensors, and cooling fans.

The chosen configuration is an air cycle cooling system, as detailed in [45]. Engine bleed air is tapped from a stage of the high-pressure compressor and supplemented by ram air. Initial heat exchange occurs in the pre-cooler, after which the air passes through a compressor and into an inter-cooler. Moisture is removed from the air stream before it enters the turbine, where both temperature and pressure are regulated to meet system cooling requirements. The conditioned air is then distributed to critical subsystems for effective thermal management. This process is illustrated in Fig. 80. While a vapor cycle cooling system was also evaluated, the air cycle system was ultimately selected due to its lower overall weight and improved suitability for the Homelander's mission profile [45].

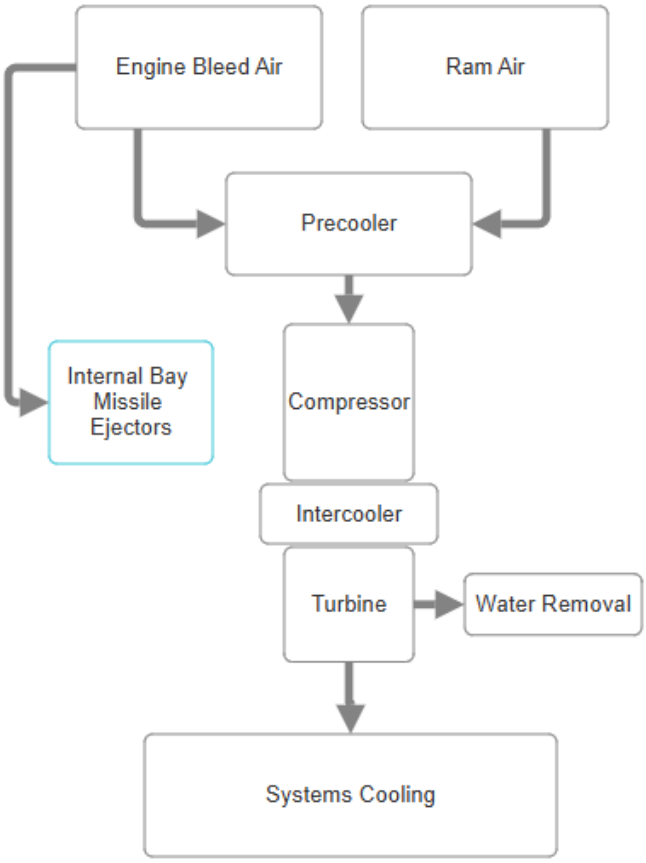

Fig. 80 Diagram of pneumatic and environmental control system.

Rather than employing a full-aircraft pneumatic system, the Homelander's pneumatic system will only support two mission-critical functions: missile ejection from the internal weapons bay and bleed-air-powered environmental control. By limiting the scope in this way, the system remains minimal and self-contained, providing high-pressure air where it's needed most without adding unnecessary cost, weight, or maintenance complexity.

For internal bay missile ejection, the Homelander utilizes the LAU-142/A AMRAAM Vertical Eject Launcher, which deploys AIM-120 AMRAAMs using a pneumatic ejector mechanism [23]. This approach eliminates the need for pyrotechnic devices within the fuselage—a key consideration given the proximity of fuel tanks surrounding the internal weapons bay. The use of pneumatic ejection not only enhances safety but also ensures compliance with MIL-HDBK-516C Section 5.3.1 requirements for safe separation, structural compatibility, and certified release systems.

In addition, the environmental control system depends on engine bleed air, extracted from the compressor stages, to provide effective cooling for avionics and the internal weapons bay. This integration of pneumatic and environmental control functions further streamlines the overall system, supporting mission reliability while maintaining simplicity.

XV. Avionics

The aircraft's remotely piloted design requires substantial avionics considerations. Without a pilot on board, there is a reduction in environmental and situational awareness. To combat this, an extensive avionics suite will provide multiple layers of redundancy to increase the aircraft's survivability and combat abilities. Table 46 details the onboard avionics architecture that enables all mission operations for the Homelander which was chosen as all GFE as specified in the RFP [1].

Table 46. Onboard Avionics Suite

Component	Volume [ft^3]	Weight [lb]
ICNIA	3.0	100
Active Array Radar	6.0	450
EO/IR Camera Suite	2.5	200
Data Bus	0.5	10
INEWS	3.0	100
Vehicle Management System	1.0	50
IRSTS	2.0	50

A. Communication

The aircraft includes a government furnished Integrated Communication, Navigation, and Identification Avionics (ICNIA) system. The ICNIA will be the core processing unit connecting the remote pilot to the aircraft, providing navigation capabilities, and supplying an identification friend or foe (IFF) system. The capabilities are similar to existing ICNIA systems that provide line-of-sight (LOS) and beyond-line-of-sight (BLOS) operations [46]. The ICNIA architecture enables redundant, simultaneous communication links across both Ka and Ku frequency bands, maintaining connectivity between the aircraft, satellites, and the remote pilot's ground control station (GCS). If connection is lost between the aircraft and remote pilot, the ICNIA will allow the aircraft to autonomously continue flight operations. This meets MIL-HDBK-516C Section 9.2.1, which requires fail-safe, redundant architecture for flight-critical systems under single- and multi-point failure conditions. The pre-programmed action in response to lost connection will be a circular loiter for five minutes at its current altitude. If connection is not reestablished in five minutes, the aircraft will automatically return to a predefined destination—defaulting to the take-off location or nearest NATO airbase unless specified otherwise. Although not implemented currently due to budget constraints, future innovation includes the ability to add more autonomous capabilities using Artificial Intelligence (AI), inspired by the MQ-20 Avenger's existing abilities. The MQ-20 uses reinforcement learning algorithms to perform air combat maneuvers by enabling collaborative operations between human and AI pilots. Real-time learning and adaptation can be executed, allowing AI pilots to be

rapidly retrained and redeployed mid-flight based on new mission data [47]. To apply this technology to the Homelander, more advanced onboard hardware with constant software and firmware updates will be required. To aid in the transition to fully autonomous flight, data collection for AI training will commence with the Homelander's first flight.

The remote pilot will be controlling the aircraft using the Lockheed Martin Unmanned Carrier Aviation Mission Control Station (UMCS). The UMCS is a modular platform that can be shaped to meet a specific aircraft's requirements [48]. The system includes various displays consistent with a standard on-board cockpit as well as displays of the aircraft's surroundings from the on-board EO/IR system as seen in Fig. 81. The UMCS incorporates both conventional throttle and stick controls for manual pilot operation and the capability for fully autonomous flight. To further enhance operational flexibility, the Homelander can also be equipped with a dedicated sensor operator, each utilizing their own UMCS to facilitate seamless information exchange with the primary operator controlling the aircraft.

Fig. 81 The Lockheed Martin UMCS GCS [48].

B. Visuals and Awareness

To provide the remote pilot with comprehensive visual and situational awareness, the Homelander is equipped with an advanced Electro-Optical/Infrared (EO/IR) camera suite. This system delivers capabilities comparable with the WESCAM MX-20 EO/IR imaging system fielded on the MQ-9 [49]. The suite supports up to seven simultaneous sensors mounted on a five-axis stabilized gimbal, enabling real-time image enhancement for both high-resolution daytime EO operations and low-visibility nighttime scenarios. The IR channel supplies thermographic video to support target detection and identification under poor visual conditions. The EO/IR assembly is installed beneath the aircraft's nose section to maximize unobstructed forward and downward fields of view. In addition to the EO/IR suite, the

Homelander is furnished with a GFE Active Array Radar. This radar provides all-weather, multi-mode detection and tracking capability. The integration of the Active Array Radar enhances the aircraft's ability to operate in complex and contested environments, allowing for automatic target recognition to the remote pilot.

The camera suite locations on the Homelander were determined through similarity analysis with the unmanned MQ-28 Ghost Bat. One camera suite is positioned on the top side of the aircraft near the nose, closely resembling the cockpit location on piloted aircraft and allowing for seamless integration above the internal avionics. To enhance coverage, an additional camera suite is installed under the nose, ahead of the landing gear, providing improved underside and rearward visuals. Figure 82 illustrates the locations of both camera suites as well as the combined field of view available to the remote pilot. While some limitations in rearward awareness remain, the Homelander is designed as an interceptor, so most targets are expected to be detected by the forward-located cameras.

Fig. 82 Camera suite locations and provided field of view.

C. Targeting and Fire Control

The onboard GFE Infrared Search and Track system (IRSTS) has the capability to perform both autonomous and operator designated target track, as well as large area search for targets. Integration of this component with the ICNIA and EO/IR cameras, allows for passive target detection, identification, and tracking. For infrared guided kinetics, should weapons deployment be necessary, the IRSTS will provide target acquisition data to the fire control system. The specific types of infrared guided ordnance that can be employed on the Homelander are explained in the Ordnance Section XVI.

XVI. Ordnance

The Homelander's armament configuration enables first-shot beyond-visual-range strike, along with defensive close-range combat capabilities through use of AIM-120 AMRAAM, AIM-9 Sidewinder missiles, or LAU-131 seven-round rocket launcher depending on configuration.

All armament configurations include two AIM-120 AMRAAMs housed within an internal weapons bay. The decision to carry the air-to-air missiles internally was driven by design priorities of drag minimization for super-cruise operations, as described in the Aerodynamics Section VI. For missions with reduced fuel requirements, the aircraft can carry

additional AIM-9 Sidewinder missiles on wingtip-mounted launch rails or the LAU-131 rocket launcher in place of external tanks. These additional ordnance options were selected to give the Homelander more flexible and cost-effective means of countering smaller threats, such as the recent global increase in drone attacks. By offering a versatile mix of internal and external armament, the Homelander is well-equipped to address both traditional aerial threats and emerging challenges in modern air combat.

Not employing the M61A1 20 mm Cannon was justified due to the aircraft's mission set, concept of operations, and remote pilot operations, where latency and input lag limit the effectiveness. Additionally, eliminating the gun reduces weight, both through the weight of the gun and ammunition, as well as through reduced structural complexity in the fuselage to support it. Eliminating the gun also simplifies the flight control system as gun compensation is not required.

A. Internal Weapons Bay

The internal weapons bay is positioned within the fuselage as shown in Fig. 83. The weapons bay actuation system opens and closes the bay doors using hydraulically driven actuators. The missile ejector system is pneumatic using hydraulic power. The LAU-142/A AMRAAM Vertical Eject Launcher was selected due to its design being solely for internal carriage and ejection of AIM-120 AMRAAMs. [23].

Fig. 83 AIM-120 AMRAAMs within internal weapons bay.

B. Wingtip Weapons

For missions not requiring external wing fuel tanks, the Homelander can be equipped with AIM-9 Sidewinder missiles on removable wingtip rails. The rail launcher of choice for the Homelander is the F-16 Wingtip Launcher (16S210) due to its combat proven capabilities, easy of maintenance, and self contained power supply [24]. When not in use, wingtip rails will be removed and replaced with fairings to maintain aerodynamic efficiency. The aerodynamic effects of AIM-9 carriage are discussed in the Aerodynamics Section VI.

Furthermore, for smaller targets, primarily drone swarms, the Homelander can be equipped with wingtip-mounted LAU-131/A Launchers [50]. This is a 7-round rocket launcher system providing additional firepower in a compact, light package. When not required, the wingtip launchers can be removed and replaced with fairings to restore the clean wing configuration.

C. Capabilities

By integrating both AIM-120 AMRAAMs and AIM-9 Sidewinders, the Homelander can engage a wider spectrum of threats. With both weapons onboard, the Homelander will have both infrared and active radar targeting capabilities in both short range and beyond-visual-range situations [51, 52].

XVII. Survivability

While the Homelander may be unmanned, posing no danger to the pilot, it does not make this multimillion dollar aircraft expendable. The chances of the vehicle returning should be maximized while staying within the limits of the aircraft's performance and cost constraints. The aircraft is unlikely to encounter significant resistance while defending the US mainland, as the region has not faced a large-scale military conflict in recent history. According to the Department of Homeland Security, current threats are primarily focused on critical infrastructure and isolated incidents rather than organized military action [53]. However, if the Homelander were deployed to allied nations, such as in Europe or Asia, the risks would increase substantially. As such countermeasures and low observability are considered, even if they are only implemented in later export variants of the Homelander.

A. Countermeasures

The countermeasure system onboard the aircraft will receive threat data from the GFE Integrated Electronic Warfare System (INEWS), interpret those data within the Vehicle Management System, and automatically deploy the determined countermeasure. Countermeasures onboard include a RF jammer, chaff, flares, and a towed decoy. Chaff and flares will be deployed from the aircraft to provide decoy targets for infrared homing missiles. A towed decoy, such as the AN/ALE-50 system by Raytheon, can provide protection against missiles guided by radio frequency and is towed by a fiber-optic cable [54]. These integrated countermeasures meet the survivability design requirements outlined in MIL-HDBK-516C Section 5.5.1, which ensures mission-critical systems are protected against guided threats.

B. Low Observability

By lowering an aircraft's chance of detection its odds of return are increased. Low observability takes a number of forms to evade an observant enemy. This ranges from visual and acoustic detection to more modern radar and infrared seeking sensors. Radar will be focused on as it most commonly used to detect and lock onto an aircraft at range.

The radar cross section (RCS) is a measure of the energy returned to a transmitter after reflecting of a specified target [9]. By reducing its RCS an aircraft reduces the effective detection range of ground or air based radar. This reduction can be achieved in a number of ways. For example sharp edges along the trailing edge of the wing or tail tend to reflect radar,

by applying coatings or serrating these edges the radar can either be absorbed or scattered [55]. Total low observability from every angle is difficult to achieve and may involve many undesirable tradeoffs. A better approach is to select a few strategic angles and reduce radar visibility from those angles. Low observability from straight on is one desirable angle, making the aircraft difficult to detect whatever it is flying towards, ideal for an interceptor.

Radar absorbing coatings are one way to achieve low observability without significantly altering the airframe. They can work by different mechanisms such as transforming electro-magnetic energy into heat energy or reflecting the radar wave with a phase shift that causes destructive interference. These coatings must be carefully applied to certain locations at calculated thicknesses to achieve the desired effect. The weight and skin friction added by these coatings must be considered during implementation [9].

Using Python code and the RadarSimPy library [56] the RCS of the Homelander was calculated and plotted, shown in Fig. 84. This provides a general demonstration of the angles at which the Homelander is most detectable, primarily from the sides as they present the most flat area. Note that these data do not take into account any specific surface material or properties. This plot serves as a baseline for when radar absorbent coatings are applied.

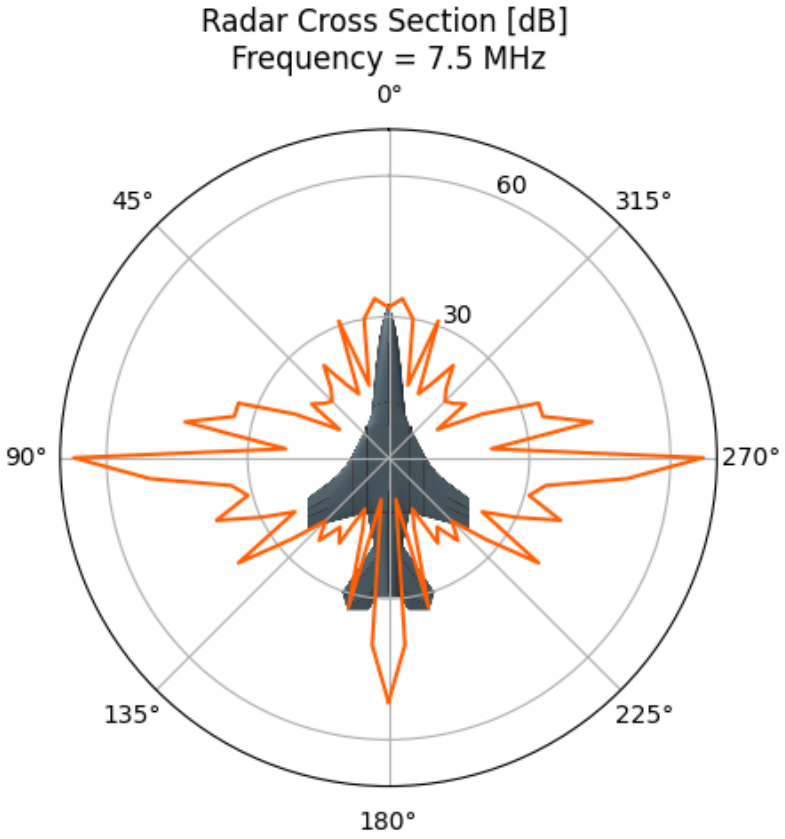

Fig. 84 RCS of the Homlander about the vertical axis.

XVIII. Repair & Maintenance

A critical aspect of the Homelander's design is meeting the 2,000 flight hour service life specified in the RFP [1]. Achieving this goal requires a robust and well-structured maintenance program. Drawing on the experience of legacy fighter aircraft with proven longevity, the team modeled Homelander's maintenance checks after the F-16, which was originally designed for 8,000 flight hours and has since been extended to 12,000 hours [57–59]. Table 47 summarizes the maintenance operations and associated man-hours adopted for the Homelander.

Table 47. Maintenance Checks

Maintenance Check	Description	Frequency (flight hours)	Man Hours
Line Check	Pre/Post Flight Checks	Before and after every flight	2
A	Light routine maintenance, lubrication, fluid refills, avionics checks	100-150	10-20
B	More in-depth, requiring minor disassembly, system diagnostics, and structural checks	200-400	100-250
C	Comprehensive inspection of critical systems, landing gear, hydraulics, and structural components	1200-2000	10,000-30,000
D	Major maintenance, component overhauls, extensive structural inspections	4000-6000	2 months

The maintenance operations currently reflect conservative maintenance timelines and are subject to decrease in frequency throughout the fighters lifetime. By referencing the maintenance operations and historical data from comparable fighters like the F-16 and F-15, the team estimates that the maintenance man-hours per flight hour (MMH/FH) for the Homelander will align closely, but lower than the values in Table 48 [9]. The reason for this is because of the lack of complex systems, such as the environmental control system.

Table 48. Historical MMH/FH of Fighter Aircraft

Aircraft	MMH/FH
F-15C	22
F-16C	19

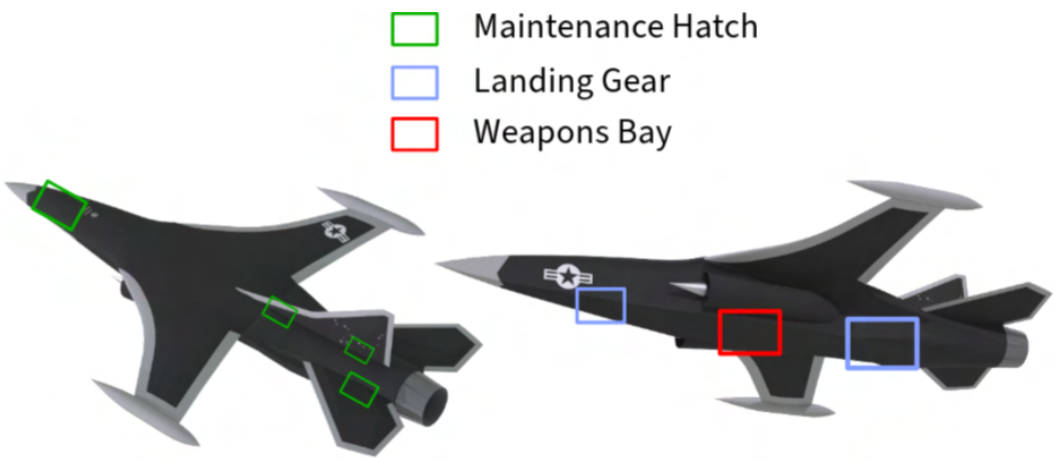

Fig. 85 Hatch locations for repair and maintenance.

A. Additional Maintenance Considerations

The Homelanders' high-wing configuration increases the complexity of maintaining the wing, mounting armament, etc.. To solve this issue, the aircraft will require an MJ-40 Bomb Lift Loader to maintain and mount the wingtip tanks and weapons. This equipment is already used by NATO, requiring minimal modification. The final Repair and Maintenance consideration includes the locations of maintenance hatches to allow for easy access to major structural components and systems. These can be seen in Fig. 85.

XIX. Cost

A. Cost Analysis using Modified DAPCA IV Model

This section outlines a structured cost estimation approach for the proposed aircraft design using a modified DAPCA IV model, as originally developed in Raymer [6]. The methodology integrates an empirically derived cost-estimating relationship tailored to major subsystems including airframe manufacturing, propulsion, avionics, and flight testing.

All base cost figures are referenced in 2012 U.S. dollars and subsequently adjusted to 2024 values using a compound inflation factor to reflect contemporary economic conditions. A full breakdown of development, production, and operational cost components is presented in Table 49, providing stakeholders with a transparent and scalable cost structure. All costs are rounded up to the nearest hundred to reflect some uncertainty.

Table 49. Modified DAPCA IV Cost Model Parameters and Results (2024 USD)

Input Parameters	
Aircraft empty weight, W	15,890 lb
Maximum velocity, V	940 kts
Production quantity, Q	1,000
Number of flight-test aircraft, FTA	4
Wrap rate, R_E	\$115/hr
Wrap rate, R_T	\$118/hr
Wrap rate, R_M	\$98/hr
Wrap rate, R_Q	\$108/hr
Total avionics cost	\$2,300,000
Engine cost	\$5,479,300
Max Mach Number, M_{max}	2.0
Thrust at Sea-Level, T_{SLS}	17,100 lbf
Turbine inlet temperature, T_R	2,916 Rankine
Computed Hours	
Engineering hours	~ 11,540,224.8 hr
Tooling hours	~ 7,316,872.8 hr
Manufacturing hours	~ 43,324,872.3 hr
QC hours	~ 5,762,208.0 hr
Corresponding Costs	
Engineering cost	\$1,327,125,800
Tooling cost	\$863,391,000
Manufacturing cost	\$4,245,837,500
QC cost	\$622,318,500
Additional Cost Components	
Development Support	\$277,537,800
Flight Test	\$83,260,900
Manufacturing Materials	\$2,598,108,400
Engine cost	\$5,479,300,000
Avionics cost	\$2,864,547,500
Total Estimated Flyaway Cost (2012 USD)	\$18,566,760,500
Inflation Factor	1.3221
Total Estimated Flyaway Cost (2024 USD)	\$24,547,114,100
Estimated Flyaway Cost per unit (2024 USD)	\$24.547 Million

B. Roskam's Cost Analysis

To complement the Modified DAPCA IV framework and enhance the fidelity of flyaway cost projections, Roskam's cost estimation model was employed as a secondary validation tool. The Roskam-based analysis in this study leverages the same primary input parameters as shown in Table 49. Adjustment multipliers were applied to account for factors such as advanced material usage, stealth features, CAD-centric workflows, and design complexity beyond historical norms. Applying the above methodology yields a unit-level flyaway cost estimate that includes airframe fabrication, propulsion and avionics integration, final assembly, and production flight testing:

Flyaway Cost per Aircraft (2024 USD): $24.7 million

This figure represents a strong and similar preliminary estimate for a modern, single-engine tactical platform employing select advanced technologies. With higher performance numbers, and material selections, and a relatively difficult manufacturing and engineering process for this aircraft, trends of a higher cost of production were observed. The cost breakdown share is shown in Fig. 86.

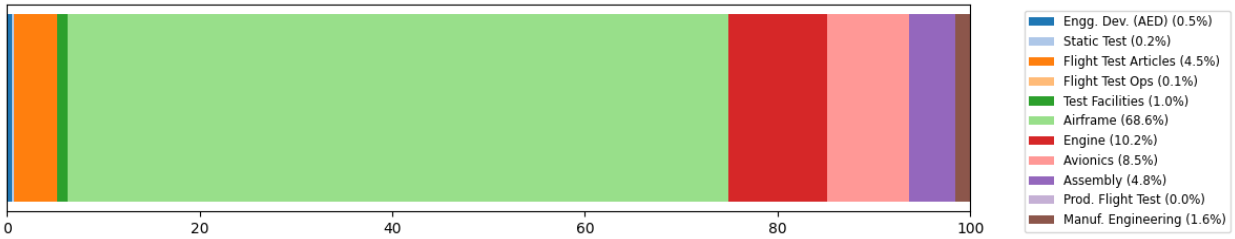

Fig. 86 Roskam's flyaway cost model breakdown.

A comparative analysis of both the Modified DAPCA IV and Roskam cost models confirms that the projected flyaway cost per unit remains within the RFP threshold of $25 million [1]. This compliance is made feasible primarily through the assumed production quantity of 1,000 aircraft, which enables favorable economies of scale. The impact of production volume on cost behavior is illustrated in Fig. 87, highlighting the significance of scaling effects in meeting budgetary constraints.

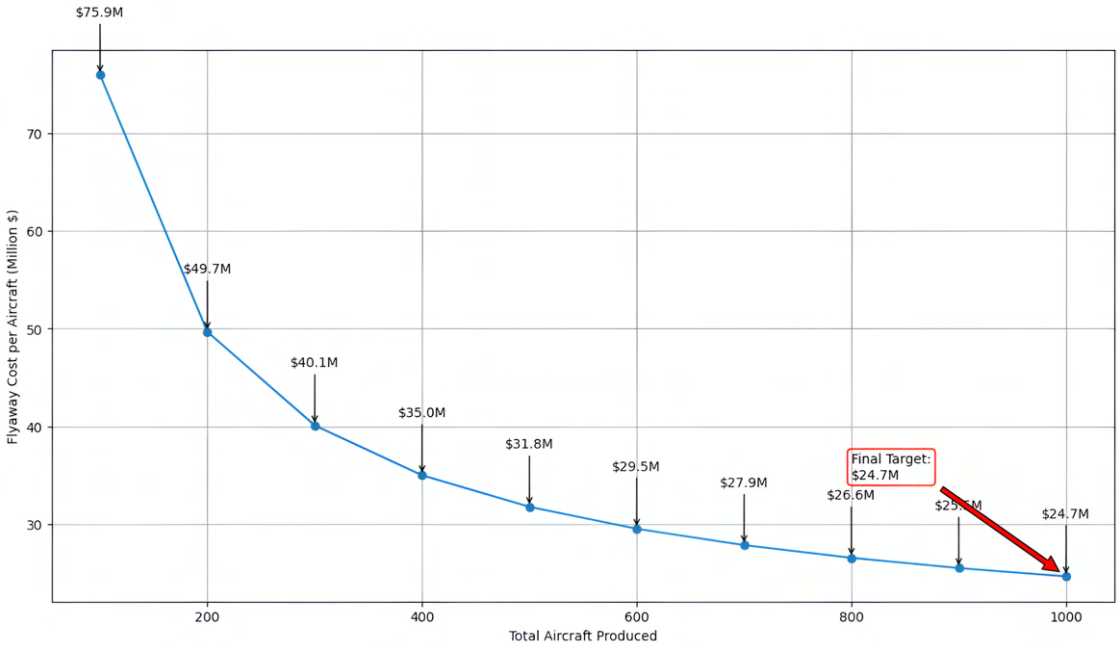

Fig. 87 Cost vs production quantity analysis.

Being under budget right now, gives the team a better headstart towards preparing the next variant for this design proposal. With profit margins of about 1-1.2%, the Homelander can be sold at the limit RFP price of $25 Million, and reinvest the projected $300 Million dollars profit back into the Research and development of MkII variant. The reinvestment can help the team research and explore past current Mach 2.0, and 60,000 ft altitude limits, and find measures to reduce current projected lifecycle costs, which will be discussed in the following section.

C. Lifecycle Cost Analysis Overview

Lifecycle Cost (LCC) analysis is a comprehensive methodology used to evaluate the total cost of ownership of an aircraft system across its entire service life. The LCC encompasses all expenditures from initial research and development (R&D) through production, operation, sustainment, modernization, and eventual disposal, providing a holistic view into critical insights into long-term affordability and program viability.

A key takeaway from this analysis is that Operating and Support (O&S) costs—covering maintenance, fuel, spares, training, and infrastructure—make up the largest portion of total expenditures for high-performance military aircraft.

For this study, the lifecycle cost estimate is broken down into the components summarized in Table 50. Notably, O&S costs were calculated over 2,000 flight hours per aircraft, using an updated per-hour cost in 2024 USD. Support and disposal costs are estimated as percentages of the total acquisition cost, following standard industry practices.

Table 50. Lifecycle Cost Breakdown

Cost Component	Calculation	Value [Millions, 2024 USD]
Operating & Support	2,000 hr/aircraft × $58,000/hr	$116,000
Support Cost	15% of acquisition cost	$528
Disposal Cost	1.5% of acquisition cost	$52.8
Total LCC (Fleet)		**$117,000**
LCC per Aircraft		**$117**

While the flyaway cost meets RFP constraints through efficient production scaling, the LCC underscores the significant long-term financial commitment required to sustain operations over the aircraft's service life.

XX. Conclusion

Draco Aerospace proudly presents the Homelander. Designed from the ground up to protect American airspace, the Homelander delivers Mach 2.0 top speed, enabling rapid response for imminent incursions. Although it achieves these high speeds, it does not compromise combat capabilities or performance during combat. The reason is its compound delta wing design, which has been rigorously validated through aerodynamic modeling and performance calculations. The Homelander is also light and small compared to modern US and non US fighters and interceptors, just as the RFP requested [1]. Boasting an empty weight of 15,890 lb, length of 50 ft, and wingspan of 27.4 ft, the Homelander is among the smallest of them all.

With a flyaway cost of just $24.7 million, the Homelander is significantly more affordable than current fifth-gen fighters, making it viable for wide deployment across the continental U.S. and potentially overseas bases. Its high-mounted wing and sleek, stealth-inspired airframe reflect a modern design tailored for performance and low observability. Armed with two internally housed AIM-120 AMRAAMs and versatile wingtip hardpoints for additional air-to-air payloads, the Homelander is fully equipped to engage enemy aircraft across the threat spectrum. Fast, affordable, and lethal, the Homelander is engineered to be the future of American air defense, and revolutionize how we protect our homeland.

XXI. References

[1] "Homeland Defense Interceptor Request for Proposal," AIAA, 2025. URL: https://www.aiaa.org/docs/default-source/uploadedfiles/membership-and-communities/university-students/design-competitions/2024-2025_team_homeland_defense_interceptor-updated-9-december-2024.pdf, [Accessed May 16, 2025].

[2] "F-106 Specifications and Performance Data," F-106 Delta Dart Association, 1998. URL: https://www.f-106deltadart.com/specs.htm.

[3] "Tejas: The Indian Light Combat Aircraft," Aeronautical Development Agency, 2015. URL: https://web.archive.org/web/20171116055959/http://www.tejas.gov.in/ADA-Tejas%20Brochure-2015.pdf.

[4] "Gripen JAS 39," Global Defense News, 2025. URL: https://armyrecognition.com/military-products/air/fighter/gripen-jas-39.

[5] "F-16 Fighting Falcon," Air Force, 2021. URL: https://www.af.mil/About-Us/Fact-Sheets/Display/Article/104505/f-16-fighting-falcon/.

[6] Raymer, D. P., *Aircraft Design: A Conceptual Approach 6th Edition*, AIAA Education Series, Playa Del Rey, California, 2018.

[7] McCormick, B. W., *Aerodynamics, Aeronautics, and Flight Mechanics 1st Edition*, John Wiley & Sons, 1979.

[8] Harris, C. D., "NASA supercritical airfoils: A matrix of family-related airfoils," NASA, NASA Langley Research Center, USA, March 1990.

[9] Nicolai, L. M., and Carichner, G. E., *Fundamentals of Aircraft and Airship Design: Volume I–Aircraft Design*, AIAA Education Series, Blacksburg, Virginia, 2010.

[10] Polhamus, E. C., "A Concept of the Vortex Lift of Sharp-Edge Delta Wings Based on a Leading-Edge-Suction Analogy," NASA, NASA Langley Research Center, USA, December 1966.

[11] Bertin, J. J., *Aerodynamics for Engineers*, JPrentice Hall, Upper Saddle River, NJ, 1998.

[12] Fegin, C. R., and Morrison, W. D., "Delta Method, An Empirical Drag Buildup Technique," NASA CR-15197, 1978.

[13] "F-16 Fighting Falcon," 169th Fighter Wing, 2015. URL: https://www.169fw.ang.af.mil/About-Us/Fact-Sheets/Article/454065/f-16-fighting-falcon/, [Accessed Feb. 12, 2025].

[14] "Probe Positioning for the Exhaust Emissions Measurements," ResearchGate, 2017. URL: https://www.researchgate.net/publication/317826392_Probe_Positioning_for_the_Exhaust_Emissions_Measurements, [Accessed May 3, 2025].

[15] Meier, N., Parsch, A., and Afnt, T., "Jet Engine Specification Database," jet-engine.net, 2021. URL: https://jet-engine.net/, [Accessed Feb. 9, 2025].

[16] Roux, E., *Turbofan and Turbojet Engines: database handbook*, Editions Elodie Roux, Great Britian, 2007.

[17] "F110-GE-132 Turbofan Engine," GE Aerospace, 2020. URL: https://www.geaerospace.com/sites/default/files/datasheet-F110-GE-132.pdf, [Accessed Feb. 9, 2025].

[18] "Deeply Upgraded Mirage 2000DRMV Strike Jet Enters French Service," TWZ, 2025. URL: https://www.twz.com/air/deeply-upgraded-mirage-2000drmv-attack-jet-is-back-in-french-service, [Accessed May 3, 2025].

[19] Ibrahim, I., "Fluid Flow Studies of the F-5E and F-16 Inlet Ducts," Nanyang Technological University, 2008.

[20] Roskam, J., *Airplane Design: Preliminary Configuration Design and Integration of the Propulsion System*, Roskam Aviation and Engineering Corporation, Ottawa, Kansas, 1985.

[21] "F100-PW-229 Product Card," Pratt & Whitney An RTX Business, 2024. URL: https://prd-sc102-cdn.rtx.com/-/media/pw/newsroom/collateral/documents/military-engines/f100-pw-229-product-card.pdf?rev=0eeacad7f5f84719973a61331df7e27f&hash=750235C595BF263A085686E70F41562A, [Accessed Feb. 9, 2025].

[22] "Advisory Group for Aerospace Research and Development: Auxilary Power Systems," NATO, Agard Conference Proceedings, France, Nov 1983.

[23] "Release Systems Product Catalog," L3Harris Technologies, 2020. URL: https://www.l3harris.com/sites/default/files/2020-08/l3harris-release-systems-product-catalog-sas.pdf, [Accessed May. 05, 2025].

[24] Marvin Engineering Company, "Wingtip Launcher 16S210," Marvin Engineering, 2025. URL: https://marvineng.com/product/wingtip-launcher-16s210/, [Accessed May. 05, 2025].

[25] Drella, M., and Youngren, H., "Athena Vortex Lattice," Ver. 3.37, 2017. URL: https://web.mit.edu/drela/Public/web/avl/, [Accessed Mar. 10, 2025].

[26] Torenbeek, E., *Synthesis of Subsonic Airplane Design*, Kluwer Academic Publishers, The Netherlands, 1999.

[27] Barua, P., Sousa, T., and Scholz, D., "Empennage Statistics and Sizing Methods for Dorsal Fins," Hamburg University of Applied Sciences, Aircraft Design and Systems Group, Hamburg, Germany, April 2013.

[28] "MIL-STD-1797: Flying Qualities of Piloted Aircraft," *United States Department of Defense*, 2004.

[29] Sadraey, M. H., *Aircraft Design: A Systems Engineering Approach*, John Wiley & Sons, New Hampshire, USA, 2013.

[30] Nelson, R. C., *Flight Stability and Automatic Control 2nd Edition*, McGraw-Hill, 1998.

[31] Roskowicz, M., Smal, T., and Szrama, S., "New Challenges and Technologies Related to Aircrafts' Battle Damages," *Scientific Journal of the Military University of Land Forces*, Vol. 50, Military University of Land Forces, Poland, 2018, pp. 208–223. https://doi.org/10.5604/01.3001.0012.2509.

[32] Sun, C. T., and Adnan, A., *Mechanics of Aircraft Structures*, John Wiley & Sons, New Jersey, 2021.

[33] "Material Properties Module," MIT, 1999. URL: https://web.mit.edu/course/3/3.11/www/modules/props.pdf, [Accessed Mar. 10, 2025].

[34] Howe, D., *Aircraft Loading and Structural Layout*, The Aerospace Series, Professional Engineering Publishing Limited, 2004.

[35] Eden, P., and Moeng, S., *Aircraft Anatomy: A Technical Guide to Military Aircraft from World War II to the Modern Day*, Amber Books Ltd, London, 2023.

[36] "Elegance in Flight," NASA, 2015. URL: https://www.nasa.gov/wp-content/uploads/2015/06/elegance_in_flight.pdf, [Accessed Mar. 10, 2025].

[37] Monette, D., "10 - Coating removal techniques in the aerospace industry," *Corrosion Control in the Aerospace Industry*, edited by S. Benavides, Woodhead Publishing Series in Metals and Surface Engineering, Woodhead Publishing, 2009, pp. 225–247. https://doi.org/https://doi.org/10.1533/9781845695538.3.225, URL: https://www.sciencedirect.com/science/article/pii/B9781845693459500104.

[38] Sensmeier, M., and Samareh, J., "A Study of Vehicle Structural Layouts in Post-WWII Aircraft," *AIAA Conference Proceedings*, 2004. https://doi.org/10.2514/6.2004-1624.

[39] Seaburg, P. A., and Carter, C. J., *Torsional Analysis of Structural Steel Members*, American Institute of Steel Construction, USA, 1997.

[40] "F-16C/D Flight Manual (T.O. 1F-16C-1)," United States Air Force, 2001. URL: https://info.publicintelligence.net/HAF-F16.pdf, [Accessed May 5, 2025].

[41] "MQ-9A Reaper," General Atomics Aeronautical, 2025. URL: https://www.ga-asi.com/remotely-piloted-aircraft/mq-9a, [Accessed May 3, 2025].

[42] "The Aircraft Tire DataBook," GoodYear Aviation Tires, 2025. URL: https://www.goodyearaviation.com/resources/pdf/Data-Section-2022.pdf, [Accessed May 3, 2025].

[43] "CRITERIA STANDARDS FOR TACTICAL AIRFIELDS," NATO, 1955.

[44] "Athena Redundant Flight Control and Navigation System," Collins Aerospace, 2010. URL: https://www.rockwellcollins.com/~/media/Files/Unsecure/Products/Product%20Brochures/Controls/Flight%20Controls/Athena-Redundant-Flight-Control-and-Navigation-System-Data-Sheet-0810.aspx, [Accessed Mar. 09, 2025].

[45] Panzieri, C. M., et al., "Unmanned Aerial Vehicle: Integrated Systems for Surveillance and Emergency," Politecnico di Torino, 2018. URL: https://iris.polito.it/retrieve/handle/11583/2785178/e384c431-964e-d4b2-e053-9f05fe0a1d67/UAV_ISSE_REV-2.pdf, [Accessed May. 05, 2025].

[46] "Cubic Halo Data Sheet," Cubic, 2024. URL: https://www.cubic.com/sites/default/files/2024-10/SCOM_Halo%20AAG_R7_DIGITAL.pdf, [Accessed May 1, 2025].

[47] "GA-ASI Flies MQ-20 Avenger Autonmously Using LEO SATCOM Datalink," General Atomics, 2023. URL: https://www.ga.com/ga-asi-flies-mq-20-avenger-autonomously-using-leo-satcom-datalink, [Accessed Mar. 6, 2025].

[48] "Skunk Works AI and Autonomy," Lockheed Martin, 2025. URL: https://www.lockheedmartin.com/en-us/who-we-are/business-areas/aeronautics/skunkworks/skunkworks-ai-autonomy.html, [Accessed Mar. 6, 2025].

[49] "WESCAM MX-20, Air Surveillance and Reconnaissance," L3Harris, 2025. URL: https://www.l3harris.com/all-capabilities/wescam-mx-20-air-surveillance-and-reconnaissance, [Accessed Apr. 27, 2025].

[50] "LAU-131/A-2 Rocket Launcher," Arnold Defense, 2025. URL: https://arnolddefense.com/product/lau-131-a-2/, [Accessed May 01, 2025].

[51] U.S. Air Force, "AIM-120 AMRAAM," U.S. Air Force Fact Sheets, 2023. URL: https://www.af.mil/About-Us/Fact-Sheets/Display/Article/104576/aim-120-amraam/, [Accessed May 6., 2025].

[52] U.S. Air Force, "AIM-9 Sidewinder," U.S. Air Force Fact Sheets, 2023. URL: https://www.af.mil/About-Us/Fact-Sheets/Display/Article/104557/aim-9-sidewinder/, [Accessed May 6., 2025].

[53] "Homeland Threat Assessment 2025," Department of Homeland Security, 2024. URL: https://www.dhs.gov/sites/default/files/2024-10/24_0930_ia_24-320-ia-publication-2025-hta-final-30sep24-508.pdf, [Accessed May 13, 2025].

[54] Moir, I., and Seabridge, A. G., *Military Avionics Systems*, John Wiley & Sons, West Sussex, England, 2006.

[55] Jenn, D. C., *Radar and Laser Cross Section Engineering*, AIAA Education Series, Monterey, California, 2005.

[56] "RadarSimPy: A Python Library for Radar Signal Processing and Simulation," RadarSimPy, 2023. URL: https://github.com/RadarSimPy/radarsimpy, accessed May 8, 2025.

[57] "F-16 Fighting Falcon Block 70/72," Lockheed Martin, 2022. URL: https://www.lockheedmartin.com/en-us/products/f-16.html#:~:text=The%20Block%2070/72%20has,with%20an%20improved%20performance%20engine, [Accessed Mar. 10, 2025].

[58] "Aviano Maintainers Exceed Standards on Downrange F-16 Inspections," U.S. Air Force, 2018. URL: https://www.af.mil/News/Article-Display/Article/624884/aviano-maintainers-exceed-standards-on-downrange-f-16-inspections/, [Accessed Mar. 10, 2025].

[59] "U.S. Air Force Further Extends Phase Maintenance Interval on Lockheed Martin F-16s," Lockheed Martin, 2003. URL: https://news.lockheedmartin.com/2003-12-04-U-S-Air-Force-Further-Extends-Phase-Maintenance-Interval-on-Lockheed-Martin-F-16s, [Accessed Mar. 10, 2025].